



VRIJE
UNIVERSITEIT
BRUSSEL

Vrije Universiteit Brussel
Faculteit Wetenschappen en
Bio-ingenieurswetenschappen
Departement Natuurkunde

1

2

3

4

5

6

7

Search for Dark Matter in the Monojet and Trackless Jets Final States with the CMS Detector at the LHC

Isabelle De Bruyn

8

Promotor

9

Prof. Dr. Steven Lowette

10

11

Proefschrift ingediend met het oog op het behalen van de
academische graad van Doctor in de Wetenschappen

12

December 2017

Samenvatting

13

14 Alle materie die we rondom ons zien, is opgebouwd uit atomen, bestaande uit negatief gela-
15 den elektronen die rond een positief geladen kern cirkelen. Hoewel de elektronen voor zover
16 onze huidige kennis strekt elementaire deeltjes zijn, bevat de kern van een atoom protonen en
17 neutronen, die op hun beurt bestaan uit up en down quarks. Al deze deeltjes en hun onder-
18 linge wisselwerking worden beschreven in een theorie die gekend staat als het Standaard Model
19 van de Deeltjesfysica. Desondanks kan deze uiterst succesvolle theorie niet alle waargenomen
20 fenomenen verklaren. Verschillende kosmologische waarnemingen tonen namelijk aan dat de
21 gekende materie die door het Standaard Model beschreven wordt maar 15% van de totale ma-
22 terie in het universum beslaat. De overige materie kan waargenomen worden door middel van
23 zwaartekrachteffecten, maar is niet zichtbaar via waarnemingen gebaseerd op licht van eender
24 welke golflengte. Dit wijst erop dat deze zogenaamde donkere materie ongeladen is. Verder is
25 er over deze materie bitter weinig geweten, maar bestaan er talloze theoretische modellen die de
26 oorsprong ervan proberen te verklaren.

27 Afhankelijk van de aard van de donkere materie deeltjes, kunnen deze geproduceerd worden
28 in hoogenergetische botsingen die plaatsvinden in deeltjesversnellers. Vele modellen nemen
29 aan dat de donkere materie deeltjes zwak met de gewone materie interageren, via een nieuwe,
30 onbekende kracht. Dit maakt het mogelijk om deze deeltjes te produceren door deeltjes van de
31 gekende materie aan een hoge snelheid tegen elkaar te laten botsen.

32 Deze thesis behandelt twee zoektochten naar donkere materie, die uitgevoerd werden aan
33 het Compact Muon Solenoid (CMS) experiment dat zich aan de Large Hadron Collider (LHC)
34 in het CERN bevindt. De LHC is momenteel de werelds grootste en krachtigste deeltjesversneller
35 en laat protonen aan een hoge frequentie tegen elkaar botsen, met een massamiddelpuntsenergie
36 van 13 TeV. De CMS detector is veelzijdig en wordt zowel voor precieze testen van het Standaard
37 Model als voor onderzoek naar nieuwe fysica gebruikt.

38 In de eerste analyse worden de donkere materie deeltjes verondersteld de CMS detector
39 ongezien te verlaten, aangezien ze neutraal zijn en zwak interageren. Wanneer ze samen met
40 andere deeltjes geproduceerd worden, kunnen deze evenwel waargenomen worden door een
41 onevenwicht in de gemeten energien, wat leidt tot ontbrekende energie in de detector. Deze
42 methode wordt in de zogenaamde monojet analyse gebruikt door te zoeken naar een combinatie
43 van ontbrekende energie en gecollimeerde bundels van deeltjes, zogenaamde jets. Het werk
44 in deze thesis heeft tot een nauwkeurigere voorspelling van de achtergrond geleid en heeft het
45 bekomen resultaat aanzienlijk verbeterd. Er werd geen nieuwe fysica waargenomen boven op
46 de voorspelde achtergrond, en nieuwe, strengere beperkingen werden op deze manier aan de
47 beschouwde modellen opgelegd.

48 In het tweede deel van deze thesis wordt een enigszins ongewoon model bestudeerd. In dit
49 geval wordt er gezocht naar sterk interagerende donkere materie deeltjes, in tegenstelling tot
50 zwak interagerende deeltjes. Deze donkere materie deeltjes zouden in paren geproduceerd wor-
51 den via een nieuw krachtdragend deeltje, dat in gelijke mate met de gekende materie interageert
52 als protonen en neutronen. Het signaal dat deze deeltjes in de detector achterlaten lijkt bijge-
53 volg sterk op dat van neutronen, aangezien deze ook ongeladen zijn. Er wordt dus gezocht naar
54 een paar neutrale jets, zogenaamde *trackless jets*, die gemakkelijk onderscheiden kunnen wor-
55 den van de achtergrond bestaande uit geladen jets. Het resultaat van dit onderzoek is volledig

56 compatibel met de voorspelde achtergrond, waardoor het beschouwde model uitgesloten wordt.

57 De twee onderzochte scenario's vullen elkaar aan, daar de ontbrekende energie die in de
58 monojet analyse gebruikt wordt in neutrale jets omgevormd kan worden wanneer de interactie-
59 waarschijnlijkheid van de deeltjes groot genoeg wordt. Hoewel er geen teken van nieuwe fysica
60 waargenomen werd, leiden deze zoektochten tot het uitsluiten van een aantal donkere materie
61 modellen.

Summary

62

63 All matter we know and see around us is made up of atoms, which consist of negatively charged
64 electrons revolving around a positively charged nucleus. While the electrons are - as far as we
65 currently know - fundamental particles, the nucleus contains protons and neutrons, which are in
66 turn composed of up and down quarks. The theoretical framework that describes all these funda-
67 mental particles and their interactions is called the Standard Model of Particle Physics. While
68 it is an extremely successful theory, multiple unresolved questions and observations cannot be
69 explained by the Standard Model. Cosmological observations, for example, indicate that the
70 known matter described by the Standard Model only contributes 15% of all the matter in the
71 universe. The remaining matter is observed through gravitational interactions, but is not visible
72 in observations of light at any wavelength, implying it is electrically neutral. Only very little is
73 known about this so-called dark matter, and many theoretical models exist to explain its origin.

74 Depending on their exact nature, dark matter particles might be produced in high-energy col-
75 lisions at particle colliders. Many models assume that the dark matter particles interact weakly
76 with ordinary matter, through a new force, making it possible to produce them in the collision
77 of two Standard Model particles.

78 This thesis covers two searches for dark matter performed at the Compact Muon Solenoid
79 (CMS) experiment at the CERN Large Hadron Collider. This particle accelerator is currently the
80 largest in the world, and provides proton-proton collisions with a record centre-of-mass energy
81 of 13 TeV at a high collision rate. The CMS detector is a multi-purpose particle detector, used
82 for various precision measurements of the Standard Model and many searches for new physics.

83 In the first analysis, the dark matter particles are expected to leave the CMS detector unde-
84 tected as they are neutral and weakly interacting. When they are produced in association with
85 other particles, they can however be observed due to an imbalance of energies measured in the
86 detector, called missing energy. This technique is used in the first dark matter search described
87 in this thesis, called the monojet analysis, where the missing energy is balanced with one or
88 more collimated sprays of particles emerging from the collision, so-called jets. The work in this
89 thesis refined the background prediction and thus increased the sensitivity of the search. No
90 significant excess above the predicted background was observed, setting new, stronger limits on
91 several dark matter models, and excluding a larger part of the available parameter space.

92 As no observation was made in this first analysis, a more unusual model is studied as well.
93 Instead of looking for weakly interacting massive particles, strongly interacting candidates were
94 considered. These dark matter candidates would be produced in pairs through a new mediating
95 particle, which has a probability to interact with matter that is similar to protons or neutrons. As
96 a result, these particles will leave a signal in the detector that is similar to neutrons, which are
97 electrically neutral as well. The investigated signature is therefore a pair of neutral or so-called
98 trackless jets, which can efficiently be differentiated from the background consisting of charged
99 jets. The result of this search is compatible with the predicted background, and again a part of
100 parameter space was excluded.

101 To conclude, the two searches covered in this thesis are very complementary, as the missing
102 transverse energy signature used in the monojet search can transform into a trackless jets signa-
103 ture when the interaction probability becomes large enough. Although no sign of new physics
104 was observed, these searches have led to the exclusion of more dark matter scenarios.

Table of Contents

106	1 Introduction	1
107	2 Dark Matter Scenarios Beyond the Standard Model	5
108	2.1 The Standard Model of Particle Physics	5
109	2.1.1 Elementary particles and their interactions	5
110	2.1.2 The theoretical framework of the Standard Model	6
111	2.1.3 Unanswered questions of the Standard Model	9
112	2.2 Dark matter	10
113	2.2.1 Observational evidence	10
114	2.2.2 Dark matter models	13
115	2.2.3 Detection of dark matter	16
116	2.2.3.1 Direct detection experiments	17
117	2.2.3.2 Indirect detection experiments	19
118	2.2.3.3 Collider experiments	19
119	2.2.4 From EFTs to simplified models	20
120	2.3 Strongly Interacting Massive Particles	22
121	2.3.1 The SIMP simplified model	23
122	2.3.2 Experimental constraints	23
123	3 The LHC and the CMS Detector	27
124	3.1 The Large Hadron Collider at CERN	27
125	3.1.1 The LHC injector chain	27
126	3.1.2 The Large Hadron Collider	28
127	3.1.3 The experiments at the LHC	30
128	3.2 The CMS detector	30
129	3.2.1 The tracker	31
130	3.2.1.1 The pixel tracker	31
131	3.2.1.2 The strip tracker	32
132	3.2.2 The electromagnetic calorimeter	33
133	3.2.3 The hadronic calorimeter	35
134	3.2.4 The muon system	35
135	3.2.5 Trigger and data acquisition	36
136	3.2.6 CMS performance in Run 2	38
137	3.2.6.1 Pre-amplifier saturation in the APV25 chip	38
138	4 Event Simulation and Reconstruction	43
139	4.1 Event generation	43
140	4.1.1 Generation of the monojet signals	46
141	4.1.2 Generation of the SIMP signal	46
142	4.2 Detector simulation	47
143	4.3 Event reconstruction	47
144	4.3.1 Track and vertex reconstruction	47

145	4.3.2	Electron and isolated photon reconstruction	49
146	4.3.3	Electron and photon identification	50
147	4.3.4	Muon reconstruction	50
148	4.3.5	Muon identification	51
149	4.3.6	Particle flow	52
150	4.3.7	Jet reconstruction	52
151	4.3.8	Identification of b-jets	54
152	4.3.9	Reconstruction of tau leptons	54
153	4.3.10	Missing transverse momentum reconstruction	55
154	4.4	Simulation and reconstruction of the SIMP signal	55
155	5	The Monojet Analysis	59
156	5.1	Physics object reconstruction	59
157	5.1.1	Jets	59
158	5.1.2	Missing transverse momentum and hadronic recoil	60
159	5.1.3	Leptons	60
160	5.1.4	Photons	60
161	5.2	Trigger selection	60
162	5.3	Event selection	61
163	5.4	Background estimation	62
164	5.4.1	The Z and W background estimation	62
165	5.4.2	The QCD background estimation	68
166	5.4.3	Simulation-based background estimation	68
167	5.5	Systematic uncertainties	69
168	5.6	Results	70
169	5.7	Improvements going from the 2015 to 2016 analysis	74
170	5.8	Limit setting	78
171	5.9	Interpretation	78
172	6	Search for SIMPs using Trackless Jets	81
173	6.1	Physics object reconstruction	81
174	6.1.1	Jets	81
175	6.1.2	Photons	82
176	6.1.3	Primary vertex	82
177	6.2	Trigger selection	83
178	6.3	Event selection	85
179	6.4	Background estimation	86
180	6.4.1	Photon + jets	86
181	6.4.2	QCD multijets	88
182	6.5	Systematic uncertainties	92
183	6.6	Results	93
184	6.7	SIMP model interpretation	95
185	7	Conclusions & Outlook	97
186	References		110
187	List of Acronyms		114

1

Introduction

188

189

190 *There is a theory which states that if ever anyone discovers exactly what the Universe is for and
191 why it is here, it will instantly disappear and be replaced by something even more bizarre and
192 inexplicable. There is another theory which states that this has already happened.*

193

– Douglas Adams, *The Hitchhiker’s Guide to the Galaxy*

194 Nevertheless, humankind is still trying to understand the most fundamental aspects of our
195 universe, by studying the fundamental particles matter is made of and the interactions between
196 them. The story so far has been summarised in a theory called the Standard Model of Particle
197 Physics. This theory has been extensively tested and has already predicted many experimental
198 observations. However, it cannot explain the full story, and some pieces remain missing. Gravity,
199 for example, is not incorporated in the Standard Model. Similarly, it cannot explain the observed
200 neutrino masses or the matter-antimatter asymmetry.

201 Another mystery stems from a series of cosmological observations made during the last
202 century. These observations are based on gravitational effects, such as measurements of the
203 rotation curves of galaxies [1] and gravitational lensing [2], and on the analysis of the Cosmic
204 Microwave Background (CMB) [3–5]. The collected evidence shows that there is matter in
205 the universe, which is not visible from measurements at any wavelength of the electromagnetic
206 spectrum. This so-called dark matter was found to constitute about 85% of the matter in the
207 universe, which means that the ordinary matter described by the Standard Model only accounts
208 for 15% of all matter. So far, only very little is known about the dark matter, as it does not
209 interact through any of the forces included in the Standard Model, and has only been observed
210 through gravitational interaction at large scales. Many theoretical models therefore exist, that
211 try to model this unknown type of matter. These theories generally assume that this form of
212 matter is composed of particles, just as the known matter, and describe a new type of interaction
213 through which these dark matter particles interact with the Standard Model particles.

214 If the dark matter indeed interacts with ordinary matter through a new force, mediated by
215 a new particle, it can be searched for, and many existing theories can be tested. A myriad
216 of experiments are currently looking for dark matter, and can be divided into three categories.
217 Firstly, direct detection experiments take advantage of the dark matter particles that should be
218 present in a halo permeating our galaxy and try to measure the recoil of nuclei generated by dark
219 matter particles passing through the Earth and scattering off the ordinary matter. The detectors
220 used for this type of experiment are mostly located underground and are well shielded from
221 radiation, though a few are airborne or space experiments. Indirect detection experiments on the
222 other hand look for particles or radiation coming from the annihilation of dark matter particles

in dense regions such as the galactic centre. These searches are studying gamma rays, neutrinos, electrons and positrons, or radio emissions. Finally, dark matter particles could potentially also be produced and detected at particle colliders. One of the direct detection experiments observed evidence pointing to the existence dark matter particles, but so far no conclusive observations have been made.

At collider experiments, such as ATLAS and CMS, dark matter candidates are often looked for by focusing on missing energy. Indeed, if the dark dark matter is assumed to interact weakly with the ordinary matter, it will be able to leave the detector unnoticed. However, these so-called weakly interacting massive particles (WIMPs), can be detected when they recoil against another object. Some examples of such collider searches are the monophoton, monojet, monolepton, and mono-Higgs analyses, categorised based on the signature in the detector. Additionally, different signatures are obtained when the dark matter is for example produced in a cascade of decays. Also resonances in e.g. the dijet mass spectrum are looked for, as this could indicate the existence of a new dark matter mediator. In general, more and more analyses are adding dark matter interpretations to their results. This thesis describes two searches for dark matter performed using data from high-energy proton-proton collisions produced at a centre-of-mass energy of 13 TeV and recorded with the CMS detector. The first analysis is the so-called the monojet analysis, which investigates the existence of WIMPs as dark matter candidates. Conversely, the second search looks for dark matter in the form of strongly interacting massive particles (SIMPs).

In Chapter 2, an overview of the Standard Model is given, as well as a short description of a few of its shortcomings. Furthermore, a summary of the existing evidence for dark matter, together with a concise review of popular dark models and a brief description of the operational or developing dark matter experiments are given. As this thesis covers dark matter searches that are performed using the CMS detector, located at one of the collision points of the LHC at CERN, more details concerning this accelerator and particle detector are summarised in Chapter 3. In Chapter 4, the procedure to reconstruct the collisions occurring inside the detector is detailed, as well as the necessary simulations of the predicted signal, which are needed in order to design a search for a particular dark matter candidate and to tune the analysis to the expected signature in the detector. The required techniques for this are described, with more details on the specific simulations needed for the searches covered in this thesis. The two complementary dark matter searches are described in Chapters 5 and 6.

The monojet analysis, covered in Chapter 5, is one of the flagship analyses which were designed to quickly detect potential dark matter candidates, for a broad range of models. I contributed to this analysis by improving the prediction of the main background, coming from the invisible decay of Z bosons into neutrinos, produced in association with one or more jets. The used strategy for the background estimation is detailed in Section 5.4 and the resulting impact on the sensitivity of the analysis is shown in Section 5.7. In the strongly interacting massive particle (SIMP) analysis, described in Chapter 6, the dark matter candidates and the Standard Model particles interact strongly through a new force, carried by a new, light mediator. The signature therefore does not consist of missing energy, but instead trackless jets are created due to the interaction of these neutral SIMPs in the dense material of the calorimeters in the detector. First, a phenomenological study of the dark matter model was performed and published [6], and subsequently the search was carried out using data collected by CMS in 2016. This work, together with my contribution to the monojet analysis are the main topics of my PhD research. The monojet search provides new, stronger limits on WIMP dark matter candidates, while the trackless jets search rules out a new dark matter model which had not been tested at colliders yet.

Besides my work on the dark matter searches described in this thesis, I also contributed in several ways to the data taking itself, more specifically related to the CMS tracker. During the shutdown preceding Run 2, I participated in the preparations to operate the tracker at a colder coolant temperature and to the subsequent re-commissioning. Afterwards, during data taking, I continued to be involved by taking on shifts in the control room and I additionally contributed

276 to the development and maintenance of the tracker Data Quality Monitoring (DQM) framework,
277 which is used to spot problems in data taking and to certify the recorded data, as mentioned in
278 Section 3.2.6.

2

279

280

Dark Matter Scenarios Beyond the Standard Model

281

282 In modern particle physics, the fundamental structure of matter at subatomic scales is described
283 by the Standard Model [7, 8], which has already predicted many experimental results and is
284 today considered among the most thoroughly tested scientific theories. The Higgs boson, the
285 last missing piece which was predicted more than 50 years ago, was recently discovered at the
286 Large Hadron Collider (LHC) in 2012 [9, 10], thus completing this elegant theory. Although it
287 has survived many precision tests so far, the Standard Model only describes 5% of the matter
288 and energy in the known universe and is unable to explain many unresolved questions and ob-
289 servations, such as the baryon asymmetry, dark matter and dark energy, the neutrino masses, the
290 incorporation of gravity, and the hierarchy problem.

291 In this chapter, a brief description of the Standard Model is first given in Section 2.1, in-
292 cluding its shortcomings. In Section 2.2, one of the missing pieces in the Standard Model, dark
293 matter, is discussed. The observational evidence for dark matter, as well as possible models
294 and detection mechanisms are detailed. Finally, in Section 2.3 one of the dark matter models
295 considered in this thesis is described in detail.

296 2.1 The Standard Model of Particle Physics

297 The Standard Model of elementary particle physics has been developed during the second half
298 of the 20th century, and reached its current formulation in the 1970's with the combination
299 of the electromagnetic and weak interactions into the electroweak interaction [11–13], incor-
300 porating the Brout-Englert-Higgs (BEH) mechanism [14–16], and the addition of asymptotic
301 freedom [17, 18] into the theory of the strong interaction. It is a quantum field theory which
302 describes the fundamental particles and their interactions, incorporating three of the four fun-
303 damental forces. While this consistent framework describes the electromagnetic force and the
304 weak and strong nuclear interactions, the fourth interaction, gravity, has not yet been included
305 successfully.

306 2.1.1 Elementary particles and their interactions

307 All ordinary matter we see around us is built up from atoms, which consist of negatively charged
308 electrons circulating around the positively charged atomic nucleus, formed by protons and neu-
309 trons, which in turn consist of up and down quarks. The electrons and up and down quarks

are fundamental particles called fermions. Although all ordinary matter can be built from this so-called first generation of fermions, there are twelve fermions with different flavours in total, six quarks and six leptons, grouped in three generations with increasing mass, as shown in Figure 2.1. The electrically neutral neutrinos interact only via the weak nuclear interaction, which complicates their observation, but they can be detected in dedicated experiments.

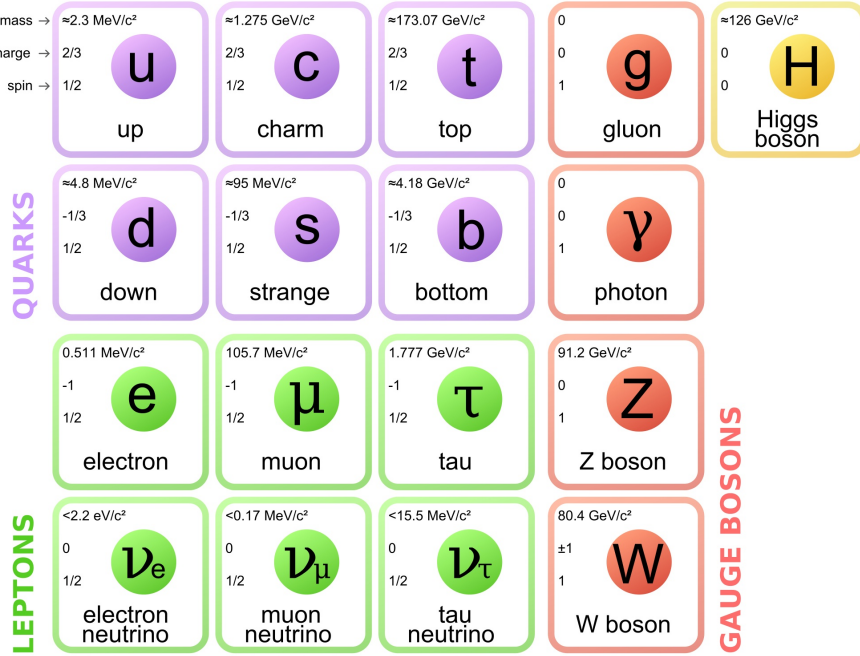


Figure 2.1: The particle content of the Standard Model, showing the fermions divided into 3 generations (columns) on the left and the bosons on the right. The electrical charges are expressed as multiples of the absolute value of the electron charge. Figure taken from [19].

A common characteristic of the fermions is their half-integer spin, in contrast to the integer spin of the force mediators, called bosons. Within the Standard Model, the mediation of the different fundamental interactions is represented by the exchange of these spin-1 gauge bosons, which are summarised in Figure 2.1. The massless photon mediates the most familiar force, the electromagnetic interaction, which is responsible for light, electromagnetic fields, and chemical reactions. The weak nuclear interaction is among other things used to describe the radioactive β decay, and is propagated by the neutral massive Z boson and two charged massive W bosons. Lastly, the strong nuclear interaction is carried by massless gluons, keeping the protons and neutrons in the atomic nuclei and holding the quark constituents together. A resulting property of the quarks is that they hadronise, i.e. they cannot exist isolated, but form bound states via the strong interaction. These bound states are referred to as hadrons, and can be made up from three quarks or a quark and an antiquark, respectively called baryons and mesons.

Finally, it is also important to note that for every fermion (f) there exists an antifermion (\bar{f}), which differs only in electric charge and handedness of spin. When matter and antimatter come into contact they annihilate, generating energy which can be transformed into other particles.

2.1.2 The theoretical framework of the Standard Model

The Standard Model goes further than merely giving an exhaustive list of elementary particles, it has a supporting theoretical framework formulated as a relativistic quantum field theory. In a quantum field theory, every particle is represented by discrete excitations of a field $\psi(x)$, where x is the space-time coordinate. The interactions and kinematics of this particle are fully determined by the action S , which is defined as the integral of the Lagrangian $\mathcal{L}(\psi(x), \partial^\mu \psi(x))$

336 over the space-time coordinates:

$$S = \int \mathcal{L}(\psi(x), \partial^\mu \psi(x)) d^4x. \quad (2.1)$$

337 The Lagrangian is a function of the field $\psi(x)$ and its first derivative $\partial^\mu \psi(x)$, where μ represents
 338 the index of the space-time coordinate. The physical behaviour of the particles is obtained by
 339 following the principle of least action $\delta S = 0$, minimizing the action.

340 In this framework based on the gauge invariance of the Lagrangian under the fundamental
 341 symmetries, the interactions between the fermions and bosons follow automatically. This can be
 342 illustrated with the following example for invariance under a general local gauge transformation.

343 As mentioned before, a fermion has a half integer spin and can thus be represented as a
 344 complex relativistic spin-1/2 field, called a Dirac spinor:

$$\mathcal{L}_{Dirac} = i\bar{\psi}\gamma^\mu \partial_\mu \psi - m\bar{\psi}\psi, \quad (2.2)$$

345 where γ^μ are the Dirac matrices, and the adjoint field $\bar{\psi} = \psi^\dagger \gamma^0$ is the field associated to the
 346 antifermion. The imposed local gauge invariance then requires the fermion fields, and the overall
 347 Lagrangian, to be invariant under so-called local phase transformations

$$\psi \rightarrow \psi' = U(x)\psi = e^{i\vec{\alpha}(x) \cdot \vec{\tau}} \psi \quad (2.3)$$

348 where $\vec{\alpha}(x)$ are the space-time dependent rotation parameters in the symmetry group represented
 349 by the Lie group generators $\vec{\tau}$. Since the derivative ∂_μ in (2.2) spoils the invariance of the
 350 Lagrangian under a local phase transformation, it is replaced with a covariant derivative

$$D_\mu = \partial_\mu - ig\frac{\vec{\tau}}{2} \vec{A}_\mu, \quad (2.4)$$

351 restoring the invariance. This however introduces new vector gauge fields A_μ , which interact
 352 with the fermion fields with a coupling strength g . As a result, the Dirac Lagrangian contains
 353 an additional term, which describes the interaction between the fermion fields mediated by the
 354 gauge fields A_μ , and (2.2) becomes

$$\mathcal{L}_{Dirac} = i\bar{\psi}\gamma^\mu \partial_\mu \psi - m\bar{\psi}\psi + g\bar{\psi}\gamma^\mu \frac{\vec{\tau}}{2} \psi \vec{A}_\mu \quad (2.5)$$

355 The matrix $U(x)$ which was introduced above, was defined as a general rotation matrix of the
 356 symmetry group $SU(N)$. In order to obtain the three fundamental interactions of the Standard
 357 Model, the described procedure can be simplified using the corresponding symmetry groups as
 358 mentioned below.

359 Electroweak theory

360 The electroweak interaction describes the electromagnetic and weak interactions, which
 361 appear very different at low energies but can be merged into a single electroweak force
 362 above the electroweak energy scale. This theory is described by requiring gauge invari-
 363 ance under the $SU(2)_L \otimes U(1)_Y$ symmetry group. This leads to 3 gauge fields W_μ^α
 364 introduced by the $SU(2)_L$ group, and one gauge field B_μ from the $U(1)_Y$ group. Two
 365 coupling constants are introduced, g_1 and g_2 , for $U(1)_Y$ and $SU(2)_L$, respectively. The
 366 corresponding observable gauge bosons are then obtained as linear combinations of these
 367 fields:

$$A_\mu = \sin \theta_W W_\mu^3 + \cos \theta_W B_\mu, \quad (2.6)$$

368

$$Z_\mu = \cos \theta_W W_\mu^3 - \sin \theta_W B_\mu, \quad (2.7)$$

369

$$W_\mu^\pm = \sqrt{\frac{1}{2}} (W_\mu^1 \mp i W_\mu^2), \quad (2.8)$$

370 where A_μ , Z_μ , and W_μ^\pm are the photon, Z^0 , and W^\pm fields, respectively, and θ_W is the
 371 weak mixing angle defined as $\tan \theta_W = \frac{g_1}{g_2}$.

372 **Quantum Chromodynamics (QCD)**

373 The strong interaction is described by the theory of Quantum Chromodynamics and is rep-
 374 resented by the symmetry group $SU(3)$. It describes the interaction between particles that
 375 carry a colour charge, which can be red, green, blue, or one of the three corresponding anti-
 376 colours. There are eight gauge boson fields associated to this group, which are massless
 377 and known as gluons. An important aspect which is unique for this interaction is asymptotic
 378 freedom, which states that the strong coupling constant, denoted by α_s , goes to zero
 379 at high energies. Consequently, the strong force becomes stronger as the distance between
 380 the strongly interacting quarks and gluons increases. As a result, the quarks and gluons
 381 cannot exist independently and are not observed individually, but are instead confined in
 382 colour-neutral hadrons. This effect is called confinement.

At this point the resulting Lagrangian including the three fundamental forces does not contain any mass terms, and so it cannot explain the observed particle masses. Additional mass terms cannot simply be added explicitly because they would break gauge invariance. Instead, a solution to this problem is found by introducing a complex scalar doublet ϕ with a non-zero vacuum expectation value (vev) v . This breaks the electroweak symmetry and is known as the Brout-Englert-Higgs (BEH) mechanism, postulated in 1964 [14–16]. The Lagrangian of the Higgs field is

$$\begin{aligned} \mathcal{L}_H &= (D^\mu \phi)^\dagger (D_\mu \phi) - V(\phi) \\ &= (D^\mu \phi)^\dagger (D_\mu \phi) - \frac{1}{2} \mu^2 \phi^\dagger \phi + \frac{1}{4} \lambda (\phi^\dagger \phi)^2, \end{aligned} \quad (2.9)$$

383 where μ is a real constant representing a mass parameter and λ is a dimensionless parameter
 384 standing for the self-interaction strength. The potential V of the scalar doublet has an infinite
 385 set of minima or ground states, and by choosing a ground state and expanding the field around
 386 it, the electroweak symmetry is broken. As a result, three of the four original fields of the scalar
 387 doublet are absorbed by the massless vector fields of the weak interaction, giving mass to the W
 388 and Z bosons:

$$M_W = \frac{1}{2} v g_2 \quad M_Z = \frac{1}{2} v \sqrt{g_1^2 + g_2^2}. \quad (2.10)$$

389 From the remaining field, the H boson arises, acquiring a mass $m_H = \sqrt{2\lambda v}$.

390 The introduction of mass terms for the fermions also follows from the BEH mechanism,
 391 which allows to insert the following gauge-invariant term in the Lagrangian:

$$\mathcal{L}_{Yukawa} = -Y_{ij} \bar{\psi}_{L,i} \phi \psi_{R,j} + h.c. \quad (2.11)$$

392 with the Y_{ij} Yukawa matrices. The L and R here denote left-handed and right-handed fermions.
 393 This handedness or chirality is defined as $\psi_L = \frac{1}{2}(1 - \gamma_5)\psi$ for left-handed and $\psi_R = \frac{1}{2}(1 +$
 394 $\gamma_5)\psi$ for right-handed fermions. The fermion masses then arise from the Yukawa interactions
 395 describing the couplings of the fermions with the Higgs field. For massive particles, a reference
 396 frame which overtakes the spinning particle can always be found, in which case the particle
 397 will seem to move backwards, flipping its helicity¹. This is however not the case for massless
 398 particles, which travel at the speed of light. As only left-handed neutrinos and right-handed
 399 antineutrinos have been observed so far, the neutrinos are massless in the Standard Model.

¹The helicity is defined as the sign of the projection of the spin vector onto the momentum vector of a particle, left is negative and right is positive.

400 2.1.3 Unanswered questions of the Standard Model

401 Although the Standard Model is an extremely successful theory, there are still many questions
 402 that remain unanswered, indicating that the Standard Model cannot be a complete theory of
 403 nature. A brief description of some of the main unsolved problems follows here.

404 **Grand Unified Theory**

405 As the weak and electromagnetic interactions were successfully unified into the elec-
 406 troweak one, the idea of representing the three forces of the Standard Model by a single
 407 one is envisaged and studied. While this Grand Unified Theory (GUT) could be a first step
 408 towards the incorporation of gravity in the Standard Model, it cannot be achieved with the
 409 current Standard Model and requires new physics at a very high energy scale.

410 **Baryon asymmetry**

411 This problem refers to the imbalance of matter and antimatter in the universe. While the
 412 Big Bang should have produced an equal amount of baryonic and antibaryonic matter,
 413 this is not measured in our observable universe. It is assumed that most of the primordial
 414 matter and antimatter annihilated, but an imbalance allowed a fraction of the matter to
 415 survive. Within the Standard Model, some asymmetry in the production of matter and
 416 antimatter could be explained by the CP-violation² of the weak interaction. However, the
 417 amount of CP-violation needed to explain the baryon asymmetry is ten times higher than
 418 is observed from Standard Model measurements.

419 **Hierarchy problem**

420 This problem is related to the mystery as to why the Higgs boson mass is so much smaller
 421 than the Planck scale. The real physical Higgs boson mass, expressed as $m_H^2 = m_{H,\text{bare}}^2 +$
 422 $\mathcal{O}(\Lambda^2)$, is composed of its bare mass and quantum loop corrections. As the Higgs boson
 423 is a scalar particle, the corrections depend strongly on the cut-off scale Λ , instead of
 424 logarithmically as is the case for renormalisable interactions. At the electroweak scale,
 425 which is of the order of 100 GeV, the corrections are of the same order of magnitude
 426 as the bare mass. When going to high energy scales such as the Planck scale however,
 427 a divergence occurs. A significant fine-tuning would be needed for the bare mass and
 428 the huge quadratic radiative corrections to cancel, in order to obtain the experimentally
 429 determined mass of 125 GeV. This unnatural amount of fine-tuning is not desirable for
 430 any theory. This so-called naturalness problem can be solved by introducing new particles
 431 which interact with the Higgs boson in such a way that the correction terms coming from
 432 Standard Model particles are partially cancelled.

433 **Neutrino masses**

434 The Standard Model predicts that the neutrinos are massless weakly interacting particles,
 435 but observations by the Sudbury Neutrino Observatory [20] and Super-Kamiokande [21]
 436 collaborations showed the first clear evidence that the neutrinos oscillate from one flavour
 437 into another. This can only be explained if the neutrinos differ in mass, implying that at
 438 least 2 of the 3 neutrinos are not massless. As mentioned above, the Standard Model does
 439 not provide masses for the neutrinos and it should therefore be extended to explain this
 440 observation.

441 **Dark matter and energy**

442 This mystery arises from cosmological observations which indicate that all known mat-
 443 ter described by the Standard Model makes up only 5% of the matter and energy in the
 444 universe. The remaining matter, called dark matter, contributes another 27%, and will be

²According to Charge Parity (CP) symmetry, the laws of physics should remain identical when converting a particle into its antiparticle and mirroring the space coordinates. However, measurements of e.g. kaon-antikaon mixing show that this symmetry is violated.

445 discussed in more detail in Section 2.2. In the Standard Model, neutrinos contribute to the
 446 dark matter, but their relic density is by far not enough to account for all the dark matter.
 447 The last 68% has been labelled dark energy and is believed to be responsible for the ac-
 448 celeration of the observed expansion of the universe, but remains even more enigmatic as
 449 no explanation can be provided by the Standard Model.

450 2.2 Dark matter

451 One of the current open questions in particle physics that is not answered by the Standard Model
 452 is the existence of dark matter. Many astrophysical observations from gravitational effects (see
 453 for instance [22]) show there must be some additional matter in the universe, the so-called dark
 454 matter, next to the known matter. Despite this, its precise nature remains as of yet unknown.
 455 Countless theoretical models are being constructed in order to explain its origin, and on the
 456 experimental side dark matter is being looked for in many different ways, but no observation has
 457 been made so far.

458 2.2.1 Observational evidence

459 The first hints of dark matter were observed by F. Zwicky [23] in 1933 by studying the velocity
 460 dispersion of galaxies in the Coma cluster. The effect is not only observed for entire galaxies,
 461 but also for various luminous objects, such as stars or gas clouds, inside a galaxy. The rotation
 462 curves of galaxies have been well studied, and show clear evidence for the existence of dark
 463 matter. An example of a rotation curve is shown in Figure 2.2, exhibiting a flat behaviour of
 464 the rotational velocity at large distances, going even far beyond the edge of the visible disk.
 465 However, in Newtonian dynamics the circular velocity is expected to be

$$v(r) = \sqrt{\frac{GM(r)}{r}}, \quad (2.12)$$

466 where $M(r) = 4\pi \int \rho(r)r^2 dr$ with $\rho(r)$ the mass density profile. Assuming $M(r)$ to be con-
 467 stant, the circular velocity is expected to fall like $1/\sqrt{r}$ beyond the disk. Since the measurements
 468 show an approximately constant velocity but a dropping visible mass density, this implies the
 469 existence of a halo with $M(r) \propto r$ and $\rho(r) \propto 1/r^2$. A universal density profile seems to be
 470 suggested by the rotation curves of both low and high surface luminosity galaxies, consisting of
 471 an exponential thin stellar disk and a spherical dark matter halo with a flat core of radius r_0 and
 472 density $\rho_0 = 4.5 \times 10^{-2}(r_0/\text{kpc})^{-2/3} M_\odot \text{pc}^{-3}$ [24]³.

473 Another evidence for dark matter comes from the effect of gravitational lensing, allowing to
 474 determine the mass of an object regardless of the light it emits. When a distant star or quasar is
 475 aligned with a massive compact object, the bending of its light due to the gravitational field of the
 476 massive object can lead to multiple distorted, magnified, and brightened images, as illustrated in
 477 Figure 2.3. The distortion of the image can then be used to determine the potential well and thus
 478 the mass of the heavy object. Yet another way to determine the mass of a cluster of galaxies,
 479 next to gravitational lensing and the distribution of radial velocities, is by studying the profile
 480 of X-ray emission, tracing the distribution of the hot emitting gas in clusters. In general, these
 481 three methods are in reasonable agreement with each other.

482 Additionally, at a cosmological level, the analysis of the Cosmic Microwave Background
 483 (CMB) allows to determine the total amount of dark matter in the universe. The existence of this
 484 isotropic background radiation was already predicted in 1948, and unintentionally discovered
 485 by A. Penzias and R. Wilson in 1965 [25]. This relic radiation comes from the propagation of
 486 photons in the early universe, once they decoupled from matter. Before this, the photons were
 487 energetic enough to ionise hydrogen, creating a plasma of electrons and protons which were

³ M_\odot denotes a solar mass, $2 \times 10^{30} \text{ kg}$.

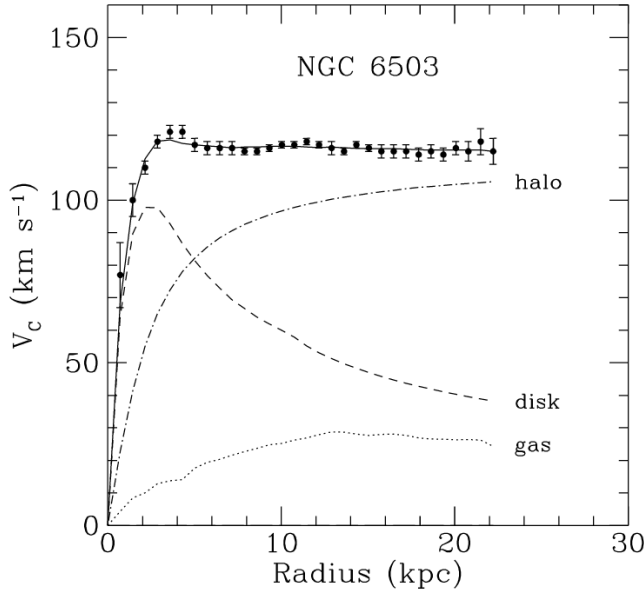


Figure 2.2: Rotation curve of NGC 6503. The dotted, dashed, and dash-dotted lines show the contributions of gas, disk, and dark matter, respectively. Figure taken from [1].

unable to combine into hydrogen. As the universe expanded and cooled down, the photons also cooled down enough to let the hydrogen atoms recombine, and the universe became transparent. The photons can then travel freely without scattering off the protons and electrons of the plasma, still carrying information from this surface of last scattering. The CMB is now known to be isotropic at the level of 10^{-5} and to follow the spectrum of a black body corresponding to a temperature of 2.726 K. However, small anisotropies in the CMB have first been observed by the COBE satellite [3] and more recently by WMAP [4] and Planck [5], as can be seen in Figure 2.4. These anisotropies correspond to small thermal variations, and are usually expanded as

$$\frac{\delta T}{T}(\theta, \phi) = \sum_{l=2}^{+\infty} \sum_{m=-l}^{+l} a_{lm} Y_{lm}(\theta, \phi), \quad (2.13)$$

where $Y_{lm}(\theta, \phi)$ are spherical harmonics. The variance of a_{lm} is given by

$$C_l = \langle |a_{lm}|^2 \rangle = \frac{1}{2l+1} \sum_{m=-l}^{+l} |a_{lm}|. \quad (2.14)$$

As the temperature fluctuations appear to be Gaussian, the information contained in the CMB anisotropy maps can be condensed into the power spectrum given by the behaviour of C_l as a function of l . This is generally represented using $D_l = l(l+1)C_l/2\pi$, as illustrated in Figure 2.5.

The CMB anisotropies are caused by acoustic oscillations arising from the conflict between the gravitational pull from baryons and dark matter and the repulsive force due to the radiation pressure from the photons. One popular model to describe and interpret these observations is the Λ CDM model. CDM stands for cold dark matter, indicating that in this model the dark matter particles are moving slowly compared to the speed of light, while the Λ represents the cosmological constant, which is associated with the vacuum energy or dark energy that is used to explain the accelerating expansion of space. The Λ CDM model is compatible with a number of observations beyond the CMB fluctuations, such as the large scale structure in the distribution of galaxies, the relative abundance of light nuclei, and the accelerating expansion of the universe which is observed from the red shift of well-known spectral absorption or emission lines in

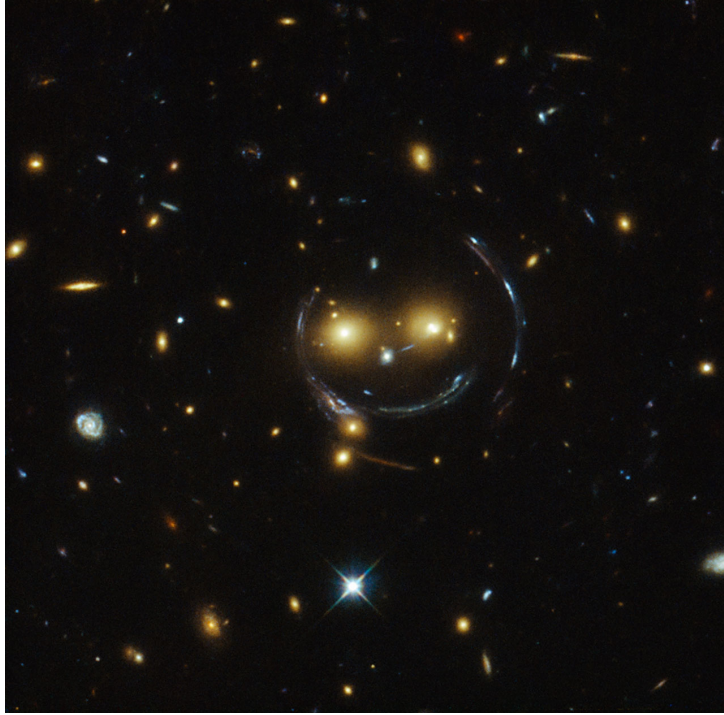


Figure 2.3: An example of gravitational lensing showing the “Cheshire Cat” image of galaxy cluster SDSS J1038+4849, taken by the Hubble Space Telescope. Figure taken from [2].

511 the light of distant galaxies. Using the Λ CDM model to fit the power spectrum of the CMB
 512 anisotropies, the multiple peaks in the spectrum can be interpreted. The angular scale of the first
 513 peak can be used to determine the curvature of the universe. The second peak determines the
 514 reduced baryon density and the third peak can be used to retrieve information about the dark
 515 matter density. From the analysis of the Planck data the abundance of baryons and matter in the
 516 universe is determined to be

$$\Omega_b h^2 = 0.02205 \pm 0.00028 \quad \Omega_M h^2 = 0.1423 \pm 0.0029 \quad (2.15)$$

517 This result shows that only about 15% of the matter in the universe is made up from the ordinary
 518 known matter, and the remaining 85% is called dark matter.

519 Hot dark matter (HDM), in contrast to CDM, is disfavoured as it is not compatible with the
 520 observed small scale structure formation in the universe. Due to the high velocity of the HDM
 521 particles, they cannot form clumps as small as galaxies, but would correspond to the formation
 522 of larger structures that surround an entire cluster of galaxies. However, models with either a mix
 523 of hot and cold dark matter, which could explain both small and large scale structure formation,
 524 or models assuming warm dark matter are still being considered.

525 More evidence for dark matter was found from a great variety of data, both on subgalac-
 526 tic and inter-galactic scales. Without discussing them here in detail, a few examples are the
 527 velocity dispersions of spiral galaxy satellites, suggesting the existence of dark halos around
 528 spiral galaxies extending well beyond the visible disk [28], the velocity dispersion of dwarf
 529 spheroidal galaxies, implying larger mass-to-light ratios than those observed in our local neigh-
 530 bourhood [29], and the so-called Oort discrepancy in the disk of the Milky Way, inferring the
 531 existence of dark matter from the inconsistency between the amount of stars in the solar neigh-
 532 bourhood and the gravitational potential indicated by their distribution [30].

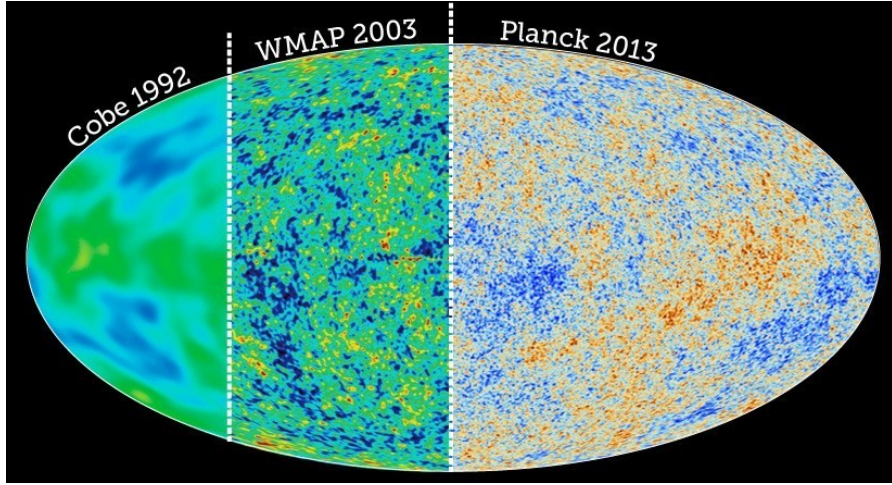


Figure 2.4: The CMB temperature fluctuations obtained from the COBE, WMAP, and Planck data. Figure taken from [26].

533 2.2.2 Dark matter models

534 There are two main categories of models that can explain the astrophysical observations detailed
 535 in the previous section. The models either predict candidates for a new type of matter, or propose
 536 modifications to the laws of gravity which could explain the observations at large scales. An
 537 example of theories in the latter category is Modified Newtonian Dynamics (MOND) [31–33].
 538 While Newton's laws of gravity have been widely tested for large accelerations, they have never
 539 been validated for objects that have an extremely low acceleration, such as stars in the outer
 540 parts of galaxies. The included modifications result in a rotation velocity which is independent
 541 of the distance to the centre of the galaxy, corresponding to a flat rotation curve. These non-
 542 relativistic models have also been extended by inserting them in relativistic theories, resulting
 543 for example in a model called TeVeS [34]. As a result, this model can also explain observations
 544 from gravitational lensing and structure formation. However, it still faces problems to explain
 545 the observed CMB anisotropies. A more recent alternative theory is based on entropic gravity
 546 and describes emergent gravity [35].

547 As these theories are often not complete or are unable to explain all the astrophysical ob-
 548 servations, the models focussing on a new type of matter to explain the observed phenomena
 549 are usually preferred. Since very little is known so far concerning the nature of dark matter, a
 550 multitude of dark matter candidates are discussed in the literature. Without attempting to be
 551 complete, a list is given and a few of the more popular candidates are briefly covered here.

552 Standard Model neutrinos

553 As mentioned before, the Standard Model could explain the existence of dark matter with
 554 the already observed neutrinos. However, it can be shown [36] that their total relic density
 555 is predicted to be

$$\Omega_\nu h^2 = \sum_{i=1}^3 \frac{m_i}{93 \text{ eV}}, \quad (2.16)$$

556 taking the sum over the 3 neutrino flavours. Currently, the most stringent upper bound on
 557 neutrino masses is

$$m_\nu < 2.05 \text{ eV} \quad \text{at 95% CL} \quad (2.17)$$

558 obtained in tritium β -decay experiments at Troitsk [37,38] and Mainz [39]. Since the mass
 559 difference between the 3 neutrinos must be very small to explain solar and atmospheric
 560 neutrino anomalies [40], this mass limit applies to the three mass eigenvalues, implying

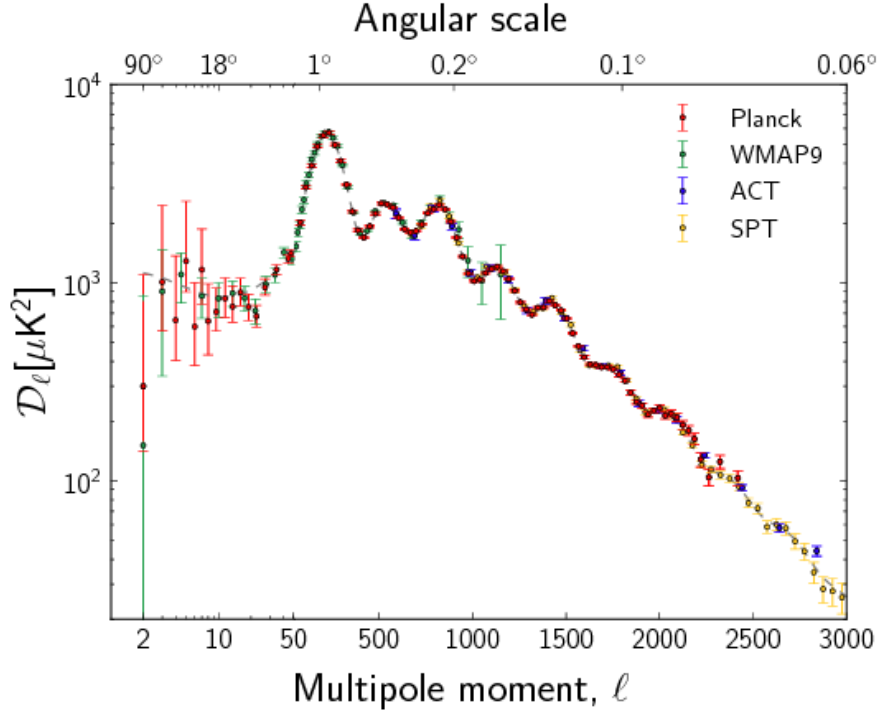


Figure 2.5: The observed power spectrum of the CMB anisotropies. The horizontal axis is logarithmic up to $l = 50$ and linear beyond. Figure taken from [27].

561 an upper bound on the total neutrino relic density of

$$\Omega_\nu h^2 \lesssim 0.07. \quad (2.18)$$

562 This shows that Standard Model neutrinos are not abundant enough to be the dominant
563 component of dark matter.

564 **Sterile neutrinos**

565 Proposed in 1993 by Dodelson and Widrow [41], these hypothetical particles are similar
566 to the Standard Model neutrinos, but without Standard Model weak interactions, except
567 for mixing. The analysis of their cosmological abundance and the study of their decay
568 products places stringent constraints on the sterile neutrinos. Light neutrinos with masses
569 below a few keV would for example be ruled out [42].

570 **Axions**

571 These particles were originally introduced to solve the problem of the apparent absence of
572 CP-violation by the strong interaction, and have often been discussed as dark matter can-
573 didates. They are expected to interact extremely weakly with Standard Model particles.
574 Furthermore, observations from laboratory searches, stellar cooling, and the dynamics of
575 supernova 1987A constrain the axion mass to be very small, of the order of or below
576 0.01 eV [43]. More recently, axions also appear as dark matter candidates in so-called
577 fuzzy dark matter scenarios as an intriguing alternative to cold dark matter, which is not
578 very successful at scales of about 10 kpc or less, due to the difficulty of modelling pro-
579 cesses such as star formation. This alternative is for example in better agreement with
580 some of the observations that are inconsistent with simple predictions from the Λ CDM
581 model, such as the absence of dark matter cusps at the centre of dark matter dominated
582 galaxies or the “missing satellite” problem [44, 45]. In this type of model, the axion mass
583 is expected to be of the order of 10^{-22} to 10^{-21} eV. More details on the motivation and
584 the astrophysical signatures can be found in [46].

585 **Massive primordial black holes**

586 Primordial black holes are a hypothetical type of black holes, formed during an inhomogeneous phase of the Big Bang. First proposed by Stephen Hawking in 1971 [47], they
 587 are good dark matter candidates belonging to the class of massive compact halo objects
 588 (MACHOs). While they are stable, have non-relativistic velocities, form very early in the
 589 universe, and are nearly collision-less, tight limits on their abundance exist from various
 590 observations, excluding them as dominant dark matter candidates for most of the preferred
 591 mass range. Nevertheless, the recent detection of gravitational waves from merging black
 592 holes by the LIGO and VIRGO experiments [48] could point to the existence of primordial
 593 black holes [49], and even to a scenario where dark matter is primarily made of primordial
 594 black holes [50, 51].
 595

596 **SUSY candidates**

597 Several particles in supersymmetry (SUSY) models can serve as dark matter candidate,
 598 such as gravitinos and neutralinos. Gravitinos are the superpartners of the graviton. In
 599 some SUSY models, they can be the lightest supersymmetry particle and can be stable.
 600 While they are very strongly motivated theoretically, they are very difficult to observe,
 601 as they only interact gravitationally. The neutralinos are the superpartners of the photon,
 602 Z boson, and neutral Higgs bosons. The lightest of the four can be stable and is an
 603 excellent dark matter candidate. These dark matter candidates are often called weakly
 604 interacting massive particles (WIMPs), since they are massive and interact through the
 605 weak interaction. As many SUSY models predict a new particle with the correct properties
 606 and self-annihilation cross section to obtain the correct abundance of dark matter today, a
 607 stable supersymmetric partner has long been a very plausible dark matter candidate and a
 608 lot of experimental effort has been made to detect it.

609 **WIMPs**

610 A prevalent assumption is that dark matter particles are a relic from the early universe,
 611 when all particles were in thermal equilibrium. At those high energies the dark matter
 612 particles and antiparticles could be formed by sufficiently energetic lighter particles, and
 613 they would annihilate back into these lighter particles as well. However, as the universe
 614 expanded and cooled down, the thermal energy of the lighter particles became insufficient
 615 to form dark matter particle-antiparticle pairs. The annihilation of the dark matter particles
 616 and antiparticles continued however, until the dark matter density decreased considerably
 617 and the interaction between the dark matter particles stopped. The number of dark matter
 618 particles would remain constant from that moment on, which is referred to as “freeze-out”.
 619 This process is illustrated in Figure 2.6.

620 When the temperature in the universe is lowered below the dark matter mass, the dark
 621 matter abundance freezes out to a value which is suppressed by $e^{-\frac{m_\chi}{T}}$, and the number
 622 density of the dark matter is given by:

$$n = \left(\frac{m_\chi T}{2\pi} \right)^{\frac{3}{2}} e^{-\frac{m_\chi c^2}{kT}}, \quad (2.19)$$

623 with m_χ the dark matter mass and T the temperature of the universe. However, as the
 624 universe is expanding at a rate given by the Hubble parameter H , the freeze-out will occur
 625 when the annihilation rate becomes smaller than the expansion rate of the universe.
 626 The annihilation rate of the dark matter particles is given by $n\sigma v$, with σ the annihilation
 627 cross section which depends on the dark matter model parameters, and v the relative velocity
 628 of the two colliding dark matter particles. The resulting relation is quantified by the
 629 Boltzmann equation:

$$\dot{n} + 3Hn = \langle \sigma v \rangle (n_{EQ}^2 - n^2), \quad (2.20)$$

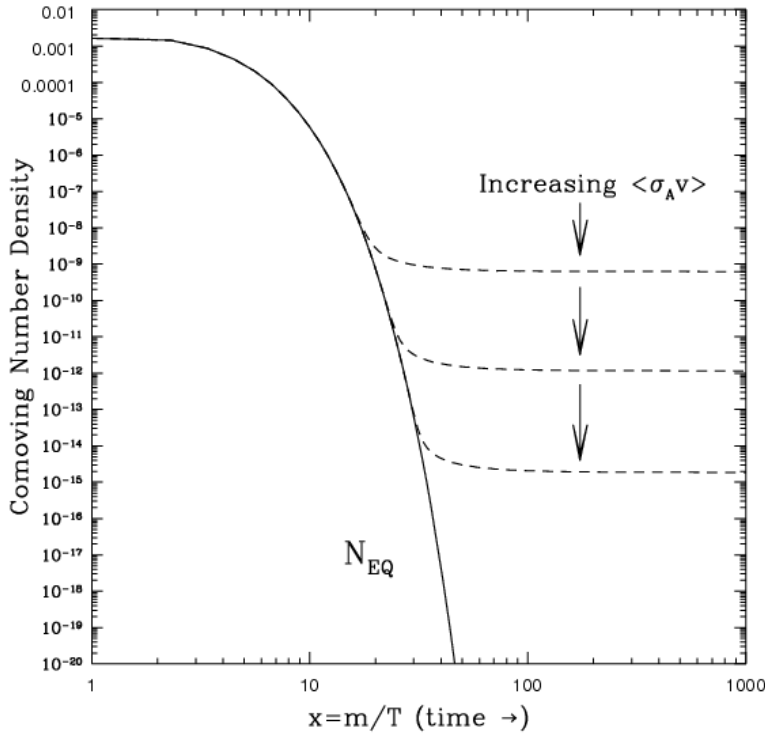


Figure 2.6: The evolution of the number density of a thermal relic in time, showing the dropping number density and the freeze-out where the density becomes constant, due to the universe expanding and cooling down. Figure taken from [52].

with n_{EQ} the number density at equilibrium. Particles with a larger interaction cross section would then continue to annihilate for a longer period of time and would be less abundant.

The interaction cross section of the annihilating dark matter particles can be inferred from the current estimates of the dark matter abundance in the universe, and can in this case not be larger than the cross section of the weak interaction. According to this model, WIMPs would be the perfect candidates for dark matter. In general, they are hypothetical new elementary particles that interact gravitationally and through any other force which is as weak or weaker than the Standard Model weak interaction, and they could have been produced thermally as described in this model. Since WIMPs have a relatively large mass, they would also constitute cold dark matter, which would fit the observed large scale structure of the universe. The coincidence of WIMPs fitting so well into this model and corresponding to the current observations is known as the “WIMP miracle”.

Many more dark matter candidates are discussed in literature, such as but not limited to heavy fourth generation neutrinos [53], Kaluza-Klein states in ADD [54] or RS [55] extra dimensions models, superheavy dark matter or Wimpzillas [56], self-interacting dark matter [57], charged massive particles (CHAMPS) [58], and Q-balls [59]. More detailed reviews are given in [36, 60, 61].

2.2.3 Detection of dark matter

The detection of dark matter can be categorised in three groups, based on the diagram shown in Figure 2.7. In the case of direct detection experiments, the studied process is the scattering of dark matter off ordinary matter. Experiments searching for dark matter with the indirect

approach look for particles or radiation produced in the annihilation of dark matter particles. Finally, at collider experiments, attempts are made to produce and detect dark matter particles by colliding Standard Model particles at high energies.

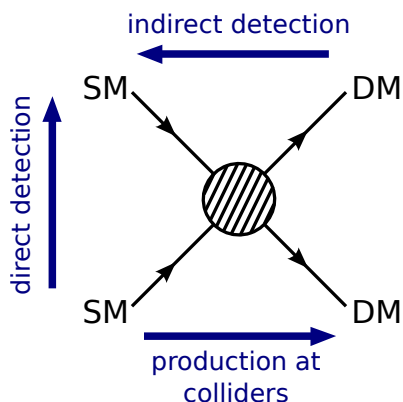


Figure 2.7: Diagram illustrating the three used methods to detect dark matter.

655 2.2.3.1 Direct detection experiments

This category of experiments is based on the fact that if our galaxy is filled with a static halo of dark matter particles, then many of them should pass through the Earth as it rotates around Galactic Center, and they could be detected by looking for the interaction of such particles with matter. This is for example done by recording the recoil energy of nuclei when WIMPs scatter off them. In order to determine the expected rate of events per unit detector material mass, the WIMP-nucleon scattering cross section and the density and velocity distribution of the WIMPs in the solar neighbourhood are needed.

There are several types of scattering processes which can be classified according to two relevant characteristics: elastic or inelastic scattering and spin-dependent or spin-independent scattering. In the case of elastic scattering, the WIMP simply scatters off a nucleus as a whole, causing it to recoil. The recoil energy spectrum can then be measured by detecting the emitted scintillation light with very sensitive detectors or by measuring very small temperature changes due to crystal vibrations. Taking a Maxwell-Boltzmann velocity distribution with a characteristic velocity our galactic rotation velocity of about 270 km/s, the recoil spectrum is exponential with typical energies of $\langle E \rangle \sim 50$ keV. This range of energies is easily detectable by current experiments, which can detect recoils as low as 1-10 keV. Instead, when the WIMP scatters inelastically, it interacts with the orbital electrons of the target, exciting the electrons or ionising the target. Differently, the WIMP could also excite the target nuclei, which would then emit a photon about a nanosecond after the observed recoil. This signature has, however, to compete with the background from natural radioactivity.

The spin dependence or independence of the scattering depends on the coupling of the WIMPs to the Standard Model particles. Spin-dependent interactions result from couplings to the spin content of a nucleon, yielding cross sections that are proportional to $J(J+1)$ instead of the number of nucleons. For spin-independent interactions, the cross section instead increases considerably with the mass of the target nuclei. The sensitivity for spin-independent scattering is therefore much enhanced over the spin-dependent one in experiments which use heavy atoms.

Numerous direct detection experiments are currently operational or in development. They use one or more techniques to measure the nuclear recoil, by detecting the scintillation light, the change in temperature, or the ionisation. Some experiments also try to separate the WIMP signatures from the background by looking for an annual modulation in the rate, which arises due to the Earth's movement around the Sun. This effect causes the Earth to have a relative

velocity with respect to the galaxy's reference frame, given by

$$v_E = 270 \text{ km/s} (1.05 + 0.07 \cos(2\pi(t - t_m))), \quad (2.21)$$

where the time is in units of years and t_m is approximately the beginning of June. As a result, a small variation of about 7% in the WIMP flux can be measured in the direct detection rate.

Currently, there is some tension between the results obtained by the different experiments, as some observations can be interpreted as dark matter signals, while other experiments are ruling out those models. The DAMA experiment for example observes an annual modulation in the event rate, pointing to the existence of WIMPs scattering elastically off the sodium and iodine nuclei in the detector [62]. Other experiments, such as SuperCDMS [63], EDELWEISS-III [64], CRESST-II [65], XENON100 [66], have seen no evidence for dark matter so far and placed limits on many dark matter models, creating a tension with the observed signal at DAMA. For WIMP masses above a few GeV, the strongest limit of direct detection experiments for spin-independent interactions is currently given by LUX [67]. For a spin-dependent WIMP-proton cross section, the most stringent limit is set by the PICO experiment [68], while the PandaX experiment places the strongest limit on the WIMP-neutron cross section [69]. An overview of the existing limits and signal observations is given in Figure 2.8, showing the mentioned experiments, and a more complete review of the existing direct detection results is given in [70].

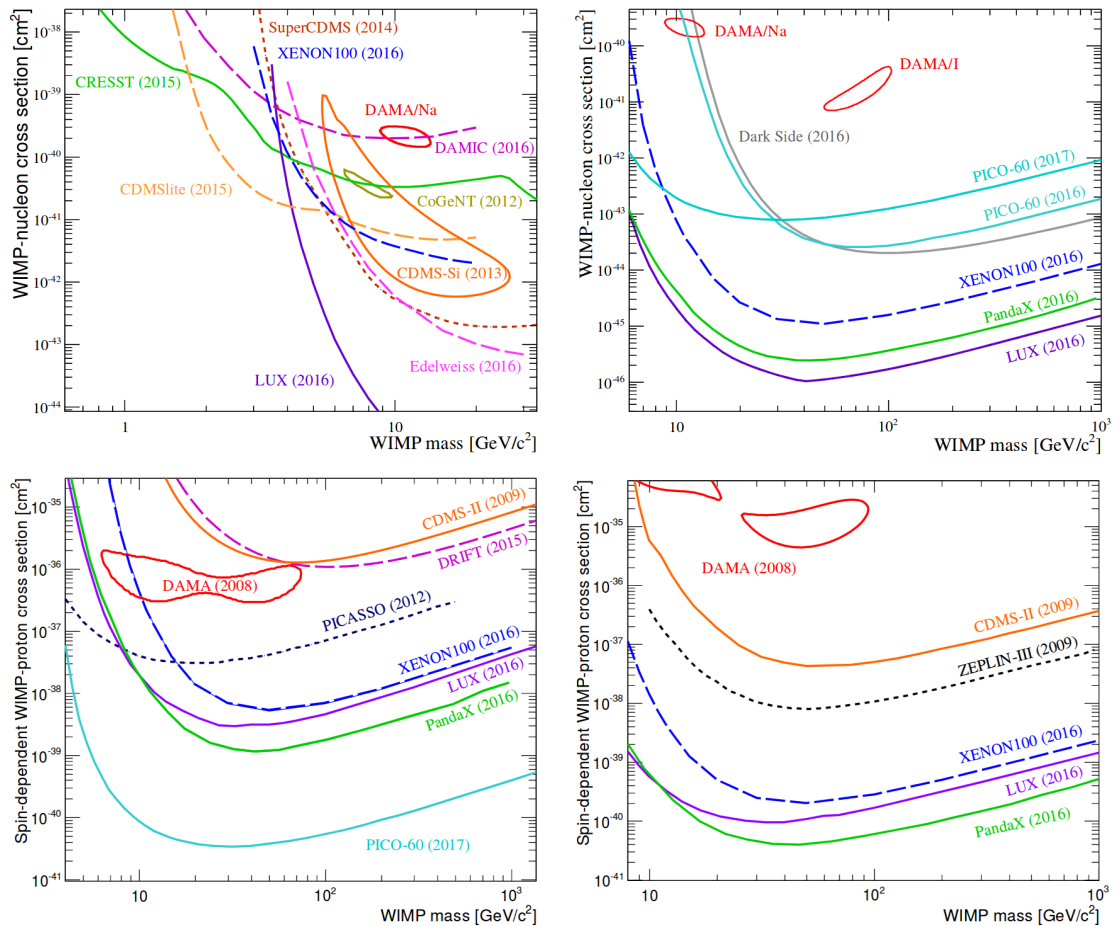


Figure 2.8: Overview of the current limits for spin-independent WIMP-nucleon interactions at low (top left) and high (top right) WIMP masses, spin-dependent WIMP-proton interactions (bottom left), and spin-dependent WIMP-neutron interactions (bottom right, the y axis title wrongly states WIMP-proton cross section). The observed signals from DAMA, CoGeNT, and CDMS-Si are shown as well. Figure taken from [70].

703 **2.2.3.2 Indirect detection experiments**

704 The indirect detection of dark matter is performed by looking for radiation produced in dark
 705 matter annihilations. A reasonable place to look at would then be in regions with large dark
 706 matter densities and thus larger annihilation rates, which will result in a higher flux of the studied
 707 radiation. Some examples are dense regions of the galactic halo such as the galactic centre,
 708 or objects like the Sun or the Earth, which could also capture dark matter particles through
 709 scattering with nucleons in their core. In the latter case, only neutrinos would be able to escape
 710 those dense objects. Other annihilation products include gamma rays, positrons, and antiprotons.

711 In order to observe gamma rays directly, the detectors must be placed in space, as photons
 712 of the relevant energy range (GeV to TeV) interact with matter via e^+e^- pair production and
 713 cannot traverse more than a surface density of about 38 g cm^{-2} . The gamma rays will not
 714 reach the ground-based telescopes as the Earth's atmosphere is 1030 g cm^{-2} thick. Neverthe-
 715 less, efforts are being made to observe gamma rays indirectly via ground-based experiments
 716 as well, by detecting the secondary particles and the Cherenkov light produced by their pas-
 717 sage through the Earth's atmosphere. In the energy range between approximately 100 MeV
 718 and 100 GeV, gamma ray telescopes on satellites such as the Fermi Large Area Telescope [71]
 719 are being used. Above 100 GeV, the ground-based Imaging Air Cherenkov Telescopes such as
 720 HESS [72], MAGIC [73], and VERITAS [74] become more adequate.

721 Neutrinos can also be produced in the annihilation of dark matter particles, but they are con-
 722 siderably more difficult to detect than gamma rays due to their weak interaction with ordinary
 723 matter. They are not easily absorbed, which makes it possible to observe them with underground,
 724 low-background experiments. Very energetic neutrinos, in the GeV-TeV range, are most easily
 725 observed by detecting the Cherenkov light from muons produced through charge current interac-
 726 tions of the neutrinos inside of or close to the detector volume. Two very large neutrino detectors
 727 are ANTARES in the Mediterranean Sea [75] and IceCube at the South Pole [76].

728 Additionally, evidence for dark matter annihilations can also be found by studying the spec-
 729 tra of cosmic positrons and antiprotons. Contrary to neutrinos and gamma rays, these charged
 730 particles do not point to their source, as their trajectory is modified by the presence of galactic
 731 magnetic fields. Currently, the main detector for positrons and antiprotons is AMS [77], which
 732 is operating on the International Space Station. Until 2016, PAMELA [78] was also active on
 733 board of the Resurs-DK1 satellite.

734 Finally, radio emissions from the galactic halo, and in particular from the galactic centre,
 735 can also provide evidence for dark matter annihilation. Electrons and protons produced in dark
 736 matter annihilations will emit synchrotron radiation at radio wavelengths as they move through
 737 galactic magnetic fields. This type of searches is performed with radio telescopes and belongs
 738 to the realm of classical astronomy.

739 **2.2.3.3 Collider experiments**

740 Since dark matter particles are usually assumed to be neutral and to interact only weakly with
 741 ordinary matter, they are expected to pass through the detectors at colliders without leaving a
 742 signal, similar to neutrinos. These particles can however still be searched for at colliders as well,
 743 when they are produced in association with other visible particles which are detected as jets or
 744 charged leptons. The dark matter particles are then observed as missing energy, as they create
 745 an imbalance in the net momentum in the transverse plane perpendicular to the colliding beams,
 746 which should be zero. One of these flagship analyses is the monojet analysis, looking for dark
 747 matter produced together with one or more jets [79, 80]. Similarly, many more searches are
 748 performed at the CMS and ATLAS experiments at the LHC by looking for signatures containing
 749 missing energy. Recent summaries are given in [81] and [82].

750 Additionally, other signatures without missing energy can also be used to search for dark
 751 matter. If the dark matter particle is produced in a cascade of decays for example, different sig-
 752 natures can be obtained, such as displaced vertices [83], disappearing tracks [84], and displaced

lepton-jets [85]. Furthermore, in dijet searches [86–88], resonances in the mass spectrum are being looked for, as this could point to the existence of a new dark matter mediator. If the dark matter particles couple to quarks via a dark matter mediator, this mediator can either decay to a pair of dark matter particles or a pair of Standard model quarks which can be observed as a pair of jets. Finally, for some particular types of dark matter candidates, such as strongly interacting massive particles (SIMPs) [89] or heavy stable charged particles (HSCPs) [90,91], more unusual signatures are expected. This is currently a developing area of dark matter research, and more and more searches looking for new signatures are appearing.

In Figures 2.9 and 2.10, recent limits from dark matter searches at the CMS experiment are compared to the direct detection results, for spin-dependent and spin-independent interactions, respectively.

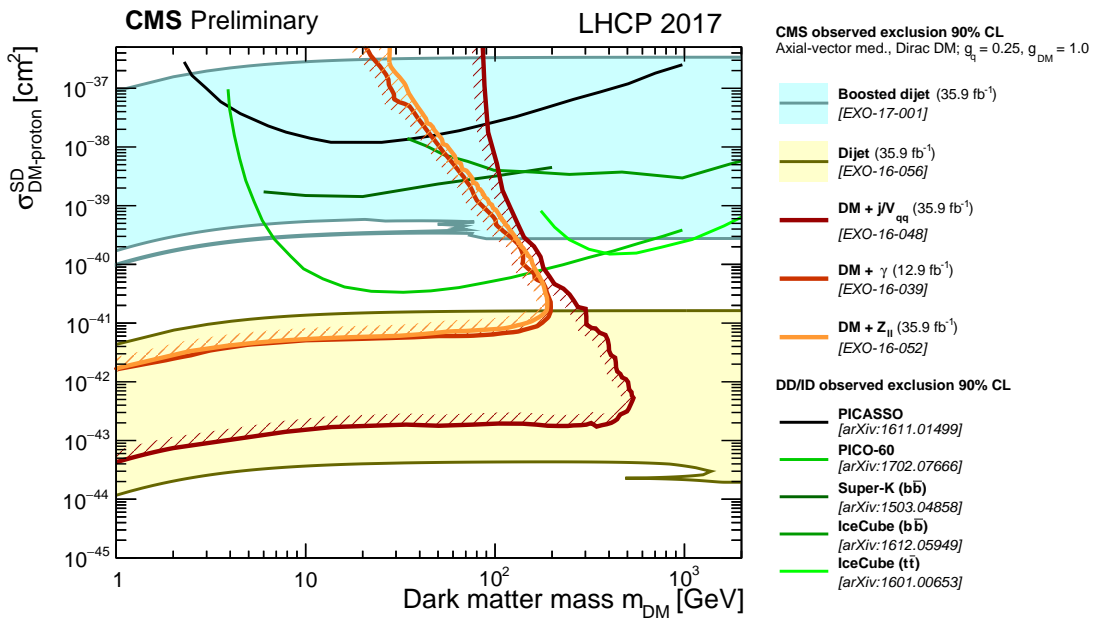


Figure 2.9: A comparison of CMS results to direct detection experiments in the $m_{\text{DM}} - \sigma_{\text{SD}}$ plane. The limits are shown at 90% CL. The shown CMS contours are for an axial-vector mediator with Dirac dark matter and couplings $g_q = 0.25$ and $g_{\text{DM}} = 1.0$. The spin-dependent exclusion contours are compared with limits from the PICASSO and PICO experiments, the IceCube limit for the $t\bar{t}$ and $b\bar{b}$ annihilation channels, and the Super-Kamiokande limit for the $b\bar{b}$ annihilation channel. It should be noted that the CMS limits do not include a constraint on the relic density and also the absolute exclusion of the different CMS searches as well as their relative importance will strongly depend on the chosen coupling and model scenario. Therefore, the shown CMS exclusion regions in this plot are not applicable to other choices of coupling values or models. Figure taken from [92].

2.2.4 From EFTs to simplified models

In order to efficiently look for dark matter at colliders, effective field theories (EFTs) have been used extensively to model the dark matter signal. The EFT models assume the dark matter production can be described as a contact interaction defined by an effective mass scale and coupling structure. This contact interaction is for example illustrated in Figure 2.11 for the monojet final state where the dark matter pair is produced in association with an initial state radiation jet. The resulting signal models can then be classified by coupling structure, and the effective scale Λ can be extracted for a specific model, defining both the coupling strength and the scale of the

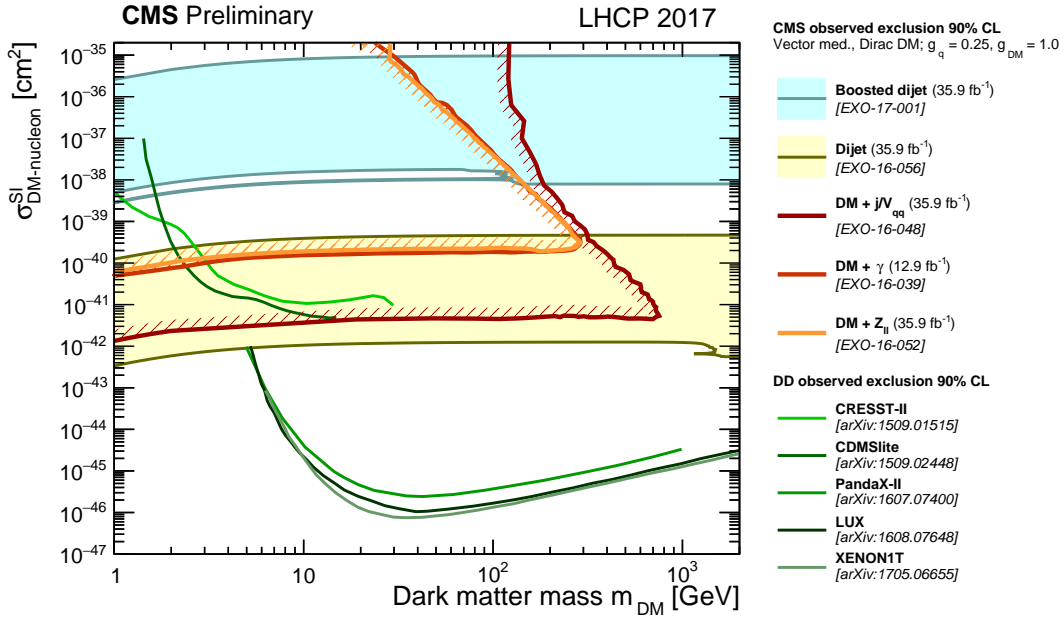


Figure 2.10: A comparison of CMS results to direct detection experiments in the $m_{\text{DM}} - \sigma_{\text{SI}}$ plane. The limits are shown at 90% CL. The shown CMS contours are for a vector mediator with Dirac dark matter and couplings $g_q = 0.25$ and $g_{\text{DM}} = 1.0$. The spin-independent exclusion contours are compared with the XENON1T 2017, LUX 2016, PandaX-II 2016, CDMSlite 2015 and CRESST-II 2015 limits, which constitutes the strongest documented constraints in the shown mass range. It should be noted that the CMS limits do not include a constraint on the relic density and also the absolute exclusion of the different CMS searches as well as their relative importance will strongly depend on the chosen coupling and model scenario. Therefore, the shown CMS exclusion regions in this plot are not applicable to other choices of coupling values or models. Figure taken from [92].

theory. An EFT is characterized by a total of 3 parameters, the dark matter mass, the EFT scale, and the EFT coupling structure. However, this approach has several limitations [93–95]. First, it implicitly assumes that the dark matter production happens through a heavy mediator, which is not resonantly enhanced at the LHC. Additionally, for low enough effective scales, the EFT breaks down. Finally, the incompleteness of the EFT makes a comparison with direct detection experiments difficult or inconsistent. Due to the limitations of EFTs, there has been a trend in the past few years to instead use simplified models which allow for a fair comparison to low energy underground direct detection experiments. In a simplified model the effective scale is then replaced by a physical mediator. The resulting models contain six parameters that can be scanned to search for dark matter, namely the coupling structure, the dark matter mass, the mediator scale, the couplings to the Standard Model and the dark matter, and, if the mediator also couples to other particles than the quarks and dark matter particles, the mediator width. This transition has been overseen by the joint ATLAS/CMS dark matter forum [96] by establishing a well defined set of benchmark models to enable the combination of different channels and the recasting of dark matter models against direct and indirect detection searches [97].

In the two dark matter searches covered in this thesis, the results have been interpreted in terms of simplified models. The monojet search described in Chapter 5 includes several simplified models recommended by the dark matter forum. Four types of mediators are considered, i.e. a vector, axial-vector, scalar, and pseudoscalar mediator. In the case of a scalar or pseudoscalar coupling, the production mode is dominated by gluon fusion. As illustrated in the right diagram of Figure 2.12, the scalar is produced through a t or b quark loop. A Yukawa coupling is as-

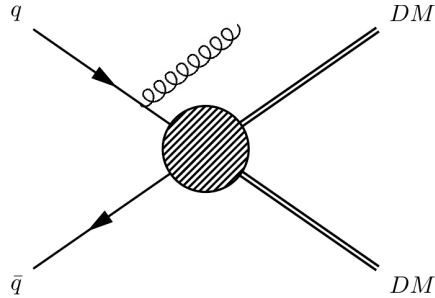


Figure 2.11: Illustration of EFT dark matter production in the monojet final state.

sumed for the coupling of the mediator to Standard Model particles, proportional to the mass of the particle. For a vector or axial-vector mediator, the production happens through the fusion of two quarks into a heavy mediator, similarly to the Z and W boson production. The coupling to quarks and potentially leptons is taken to be unity, and universal for all flavours. For all mediator types, the coupling to the dark matter particles is assumed to be unity. In addition, the minimal width assumption is made, implying that the mediator couples to all Standard Model and the dark matter particle and no extra particles are introduced. If such particles would be present, the width would increase and the sensitivity of the analysis would be reduced. A scan is then performed over the mass of the dark matter candidate and the mass of the mediator.

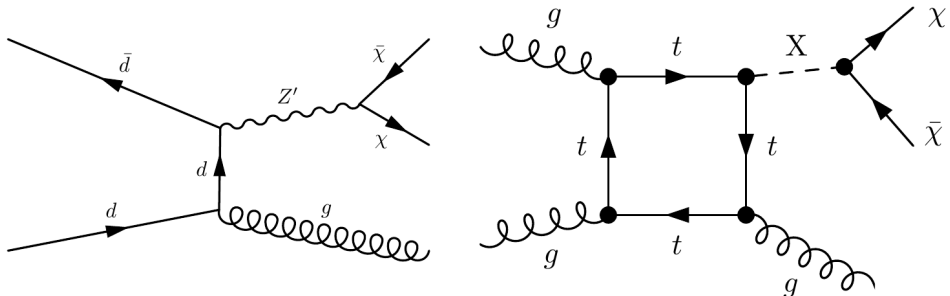


Figure 2.12: The vector (left) and scalar (right) production diagrams in the monojet final state.

2.3 Strongly Interacting Massive Particles

As no observation of dark matter has been made so far, despite many searches probing the more popular models described in the previous section, many scenarios now venture beyond minimal models or give up basic assumptions for the WIMP. In the following model, which is studied in this thesis, the interaction cross section of the dark matter with normal matter is so high that the particles are no longer WIMPs, but so-called SIMPs. This model is not part of the models recommended by the dark matter forum, but can also be motivated by the long lasting interest for self-interacting dark matter (SIDM)⁴ particles with a large cross section [57], which could help to explain observations that present a challenge for the cold dark matter scenarios, such as the missing satellites or core-cusp problems [98–101]. While it is possible to create models with a strongly interacting hidden sector that is weakly coupled to the Standard Model particles, SIDM particles that interact rather strongly with the known matter particles can be considered as well.

⁴Incidentally, self-interacting and strongly interacting share the same abbreviation, such that SIDM can also stand for strongly interacting dark matter and SIMP for self-interacting massive particles in the literature.

2.3.1 The SIMP simplified model

In this simplified model, the dark matter particles χ can be produced at the LHC in pairs, through a new strong interaction with a new mediator ϕ , as illustrated in Figure 2.13. These SIMPs are neutral and stable, and are generated off-shell as the mediator is very light, of the order of the pion mass: $m_\phi = 140$ MeV. We only consider the case of fermionic candidates, since the bosonic form is ruled out by constraints coming from neutron stars and black holes, as is described in Section 2.3.2. Both the cases with a scalar or a vector mediator can be studied, and the corresponding interaction Lagrangian is

$$\mathcal{L}_{\text{int}} = \begin{cases} -g_\chi \phi \bar{\chi} \chi - g_q \phi \bar{q} q & \text{(scalar mediator)} \\ -\tilde{g}_\chi \phi_\mu \bar{\chi} \gamma^\mu \chi - \tilde{g}_q \phi_\mu \bar{q} \gamma^\mu q & \text{(vector mediator)} \end{cases} \quad (2.22)$$

with $g_\chi g_q, \tilde{g}_\chi \tilde{g}_q < 0$ to avoid the formation of bound states. For simplicity we assume that the SIMPs have a universal coupling to quarks, although a flavour dependent coupling could be preferred, as light SIMPs with a significant coupling to b or c quarks are probably constrained by B and D meson phenomenology. SIMPs lighter than about 5 GeV could for example appear in the decay of b or c quarks, and would be constrained by limits on the invisible decay of B and D mesons.

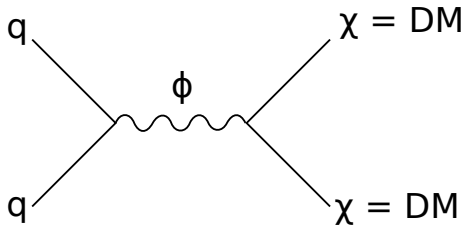


Figure 2.13: Feynman diagram showing the production of a SIMP pair, through a new low-mass mediator.

Introducing a new strong interaction between quarks can however modify nuclear potentials. In order to keep the impact small, the mediator is assumed to not modify nuclear potentials by more than $\mathcal{O}(10\%)$, such that $g_{\chi N} \lesssim 0.3 g_{\pi NN} \sim 3$ for a mediator with the mass of a pion, where $g_{\pi NN} \sim 13$ is the effective pseudoscalar pion-nucleon coupling [102]. The quoted values are however not very precise, as a large spread of values can be found in the literature for meson-nucleon effective couplings, sometimes differing by a factor 2 or more (see e.g. [103] for comparison). This shows the difficulty of dealing with strong interactions in the framework of effective field theories, which arise because contributions from many mesons need to be taken into account, each of them with a different coupling. No constraints on modified strong interactions at low energies seem to exist in literature so far, however searches at fixed-target experiments do place constraints on the existence of strongly interacting stable neutral particles.

In summary, the model has 4 free parameters: the two couplings, the mass of the mediator m_ϕ , and the mass of the SIMP m_χ . At the LHC, only the product of the couplings appears, while astrophysical observations constrain both the dark matter self-interaction and the interaction with the Standard Model.

2.3.2 Experimental constraints

Naively, one would expect such an unusual model with strong interactions not to be viable, as various types of experiments and observations set constraints on SIMPs as dark matter candidates. However, some of these limitations can be avoided by the assumptions in the model

described above. The relevant existing measurements are described below, showing there is a still a part of phase space which remained unexplored so far.

Bound states

Searches for heavy isotopes, in particular heavy water, constrain the formation of bound states between SIMPs and nucleons, ruling out particles with a mass below 10 TeV for the scenario with SIMPs as dominant contribution to dark matter. This constraint is evaded by assuming a purely repulsive *SIMP-nucleon* interaction with opposite sign couplings, as is specified in the Lagrangian (2.22). In the vector mediator case, vector mediators would however couple to the dark matter antiparticles with an opposite charge. This is avoided if no dark matter antiparticles are around, i.e. if the abundance of dark matter is asymmetric. A reason for having asymmetric SIMPs is that if they are the dominant source of dark matter, then the dark matter abundance is set by either an asymmetry or through a non-thermal mechanism. In the case of a symmetric *SIMP* candidate, the dark matter abundance is determined by thermal freeze-out, and it can only be a sub-dominant component. Additional constraints also exist on the dark matter self-interacting strength from halo shapes and merging galaxies such as the Bullet cluster [104, 105].

Earth heating

A second argument for an asymmetric abundance of SIMPs comes from experiments measuring the heat emitted from the Earth's core. For the typical SIMPs cross sections, the dark matter particles can be captured by the Earth and accumulate in its core over time. Annihilating SIMPs would then provide a substantial source of heat and could modify the Earth's heat flow. This can be measured by detectors in deep underground shafts [106] and rules out the scenario with symmetric SIMPs.

Neutron stars and black holes

In the asymmetric scenario, light scalar dark matter particles can however be collected in the cores of neutron stars and cause them to collapse into black holes. Bosonic dark matter candidates are therefore excluded, and we consider only fermionic candidates as mentioned previously.

Direct detection searches

Many bounds on the *SIMP* parameter space come from the direct detection searches as well. Underground experiments, such as CDMS and XENON, place strong constraints at smaller cross sections, about 5 orders of magnitude below the *SIMP* cross section, as can be seen from Figure 2.14. At the higher cross sections considered here, the SIMPs are stopped by the Earth's atmosphere, and they cannot reach the underground detectors. At higher altitudes however, space or airborne experiments such as RSS [107], a balloon-based experiment with a silicon semiconductor detector, and XQC [108], a sounding rocket experiment, exclude SIMPs in some regions of phase space. More details on these constraints can be found in [106], where they have been extensively reviewed.

Nucleosynthesis and cosmic rays

There are also bounds from primordial nucleosynthesis and cosmic rays, reviewed in [109] and [110]. The protons in cosmic rays can scatter off dark matter particles and create neutral pions, which decay to photons and could be detected in gamma ray telescopes. Although limits have been placed on dark matter-nucleon interactions [110], these constraints depend on many assumptions and adopt a form of the dark matter density near the galactic core. Since the considered model describes a nonstandard form of dark matter with a relatively strong interaction with baryons, these densities may be considerably different.

CMB and large scale structure

Observations of the CMB anisotropies and the large scale structure power spectrum, in-

897 cluding from the Lyman- α data [111, 112] additionally also place strong constraints on
 898 interactions between dark matter and baryons.

899 Fixed-target experiments

900 Finally, a relatively old fixed-target experiment led in 1976 at FNAL with a beam of
 901 neutral particles produced by 300 GeV protons hitting a beryllium target was used to
 902 look for massive, strongly interacting, neutral particles [113]. The mass of the particles
 903 was determined using their flight time and their kinetic energy which was measured in a
 904 calorimeter. Neutral particles with a mass larger than 2 GeV were searched for, in order to
 905 discriminate the candidates from the background of neutrons and lighter hadronic states,
 906 up to $m_\chi \lesssim \sqrt{E}/2 \approx 12$ GeV, limited by the beam energy of $E = 300$ GeV. Single
 907 particle production was considered, but the results apply to pair production as well when
 908 they are translated into the case where 2 neutral particles are boosted and fly away in the
 909 same direction. The search showed no significant excess above the expected background
 910 and limits were placed on the invariant production cross section per nucleon versus the
 911 neutral particle interaction cross section. As an example, for an interaction cross section
 912 of 1 mb, a limit on the total production cross section of about $2.5 \times 10^{-35} \text{ cm}^2 = 25 \text{ pb}$
 913 is found, and this limit is reported by the Particle Data Group [114]. Comparing the
 914 considered SIMP model to this result by simulating the pair production at $\sqrt{s} = 25$ GeV,
 915 one can conclude that SIMPs between 2 and about 6 GeV are already excluded by this
 916 experiment [6].

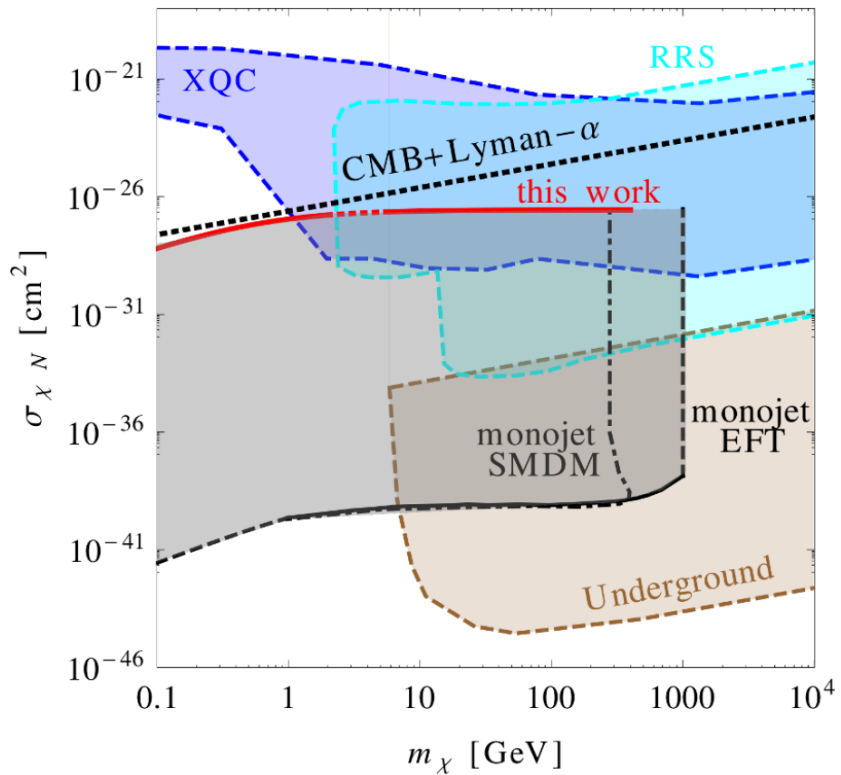


Figure 2.14: Summary plot showing the SIMP model (red) in comparison with the most important applicable constraints, coming from the LHC monojet analyses (black), the atmospheric XQC and RRS experiments (blue), underground experiments (brown), and the CMB observations and Lyman- α data (black dashed line). Figure taken from [6].

3

917

918

The LHC and the CMS Detector

919 In order to investigate the currently unsolved mysteries of particle physics, such as the existence
920 of dark matter, many experiments can be conducted, among other things at particle colliders.
921 The largest particle accelerator in the world is the LHC, located at the European Organization
922 for Nuclear Research (CERN) in Geneva, Switzerland. At this accelerator, protons are being
923 accelerated at energies up to 6.5 TeV, giving rise to a record centre-of-mass energy of 13 TeV
924 in the proton collisions. Using data from the collisions generated at the interaction points along
925 the accelerator ring, the Standard Model can be tested in many ways and searches for particles
926 beyond the Standard Model can be performed.

927 In Section 3.1 more details are given about the LHC and the 4 main experiments situated
928 at the interaction points. In particular, the general-purpose Compact Muon Solenoid (CMS)
929 detector is described in Section 3.2.

930 3.1 The Large Hadron Collider at CERN

931 The LHC was built in the already existing Large Electron Positron (LEP) collider tunnel, which
932 was excavated in the 1980's and has a circumference of 27.6 km. Contrary to the LEP col-
933 linder, the LHC accelerates particles of the same charge, namely protons or lead ions. Much
934 higher luminosities can therefore be reached, since only particles are used and the generation
935 of antiparticles is not needed. This was the limiting factor at the Tevatron, where protons and
936 antiprotons were used. Additionally, at the probed energies the colliding particles are not the
937 protons or ions, but their constituents, which carry a varying fraction of the total momentum.
938 This makes the LHC an ideal instrument for exploration at higher energies, as the collisions
939 naturally cover a wide energy range.

940 3.1.1 The LHC injector chain

941 The protons (or lead ions) can not directly be injected in the LHC, but need to be accelerated
942 gradually in several pre-accelerators, as illustrated in Figure 3.1. For the proton beams, the LHC
943 injection chain starts at a bottle of hydrogen, where protons are stripped from the hydrogen atoms
944 and accelerated up to 50 MeV by a linear accelerator (LINAC2). The protons are then transferred
945 to a chain of circular accelerators, starting with the Proton Synchrotron Booster (PSB) which
946 accelerates them to an energy of 1.4 GeV. Next, the protons go through the Proton Synchrotron
947 (PS) and are delivered to the Super Proton Synchrotron (SPS) at an energy of 26 GeV. Finally,
948 the protons are injected in the LHC in opposite direction with an energy of 450 GeV.

The lead ions are first accelerated in a different linear accelerator, LINAC3, before being injected in the Low Energy Ion Ring (LEIR) at an energy of 4.5 MeV per nucleon. Here the ions are accelerated to an energy of 72 MeV per nucleon, and they then follow the same path as the protons through the PS, where they are accelerated to 5.9 GeV and stripped from the last of their electrons, and the SPS, where they are accelerated to 177 GeV. The record centre-of-mass energy for heavy ion collisions at the LHC so far has been 5.02 TeV and 8.16 TeV, for lead-lead (Pb-Pb) and proton-lead (p-Pb) collisions in 2015 and 2016, respectively.

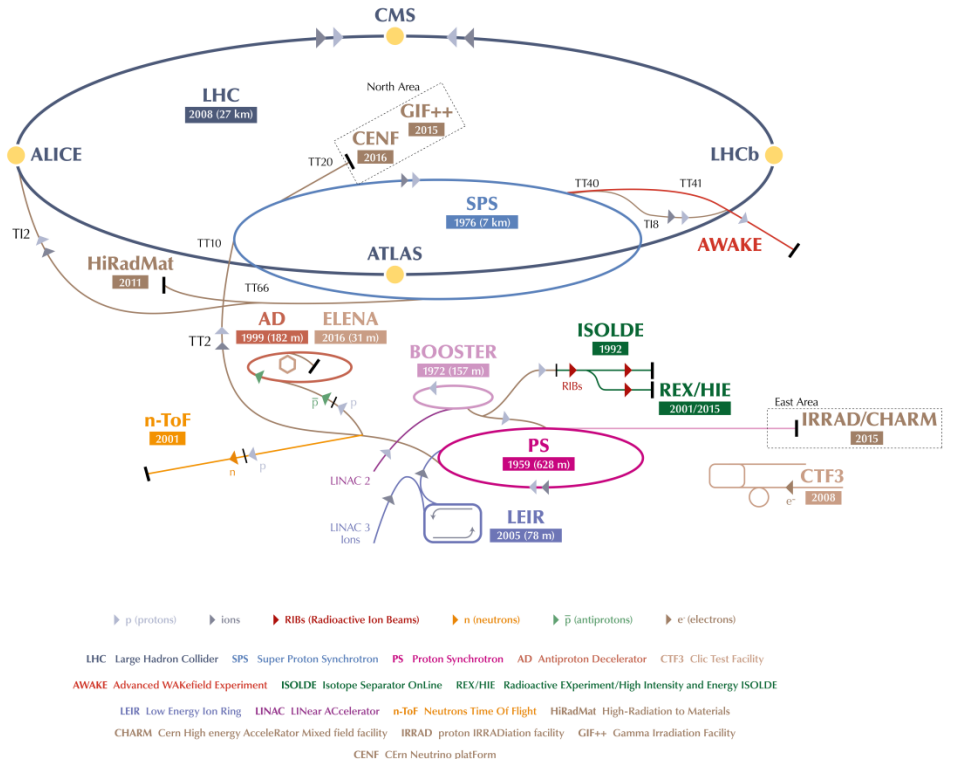


Figure 3.1: Schematic view of the various linear and circular accelerators of the CERN accelerator complex, including the LHC injection chain. Figure taken from [115].

3.1.2 The Large Hadron Collider

The most relevant specifications for a particle physics accelerator are the maximum energy and the luminosity that can be reached. High energy is necessary in order to be able to create new heavy particles, which are for example predicted in many theories beyond the Standard Model.

The protons are kept on the correct orbit by the 1232 LHC dipole magnets. These magnets are cooled down to 1.9 K with liquid Helium and supplied with a current of 12 kA to reach the design field of 8.33 T. This limits the maximum beam momentum of the accelerator to

$$p = B/\rho = 8.33 \text{ T}/2804 \text{ m} = 7 \text{ TeV}/c, \quad (3.1)$$

with ρ the bending radius of the tunnel. The protons are accelerated up to the desired energy by radio-frequency (RF) cavities, which produce an oscillating electric field.

A high event rate or luminosity \mathcal{L} is equally important, to obtain a sufficiently high number of collisions. For a process with cross section σ , this rate is

$$\frac{dN}{dt} = \mathcal{L}\sigma. \quad (3.2)$$

In order to achieve the high design luminosity of $10^{34} \text{ cm}^{-2}\text{s}^{-1}$ in the LHC, the protons are concentrated in bunches which are focused by strong quadrupole magnets around the interaction regions. The RF frequency is 400 MHz, which corresponds to a wavelength of 75 cm and confines the protons into buckets of 2.5 ns. The LHC circumference would then allow for 35640 buckets in total, which would result in bunch crossings spaced by only 37.5 cm. A more realistic spacing is 25 ns, corresponding to one bunch per 10 RF buckets. Additionally, 225 ns gaps are present between the bunch trains, corresponding to the rise time of the injection kicker magnets. One gap of 3 μs is necessary as well to allow clean beam dumps. These requirements limit the number of bunches to a maximum of 2808.

After almost 25 years of design and construction, the LHC was completed in 2008 and the commissioning of the machine started. However, during a powering test on 19 September of the same year an electric arc developed inside a bus bar which led to a large release of helium and a pressure wave that caused extensive mechanical damage to the affected LHC sector. This incident delayed the first collisions, with one bunch per beam and at a beam energy of 900 GeV, until late 2009. During 2010 and 2011 a centre-of-mass energy of 7 TeV was used for the collisions, which was then increased to 8 TeV in 2012. The instantaneous luminosity was also increased, starting from $2 \times 10^{32} \text{ cm}^{-2}\text{s}^{-1}$ in 2010 to more than $6 \times 10^{33} \text{ cm}^{-2}\text{s}^{-1}$ in 2012. During the 3 years of data-taking in Run 1, data corresponding to an integrated luminosity of 45.0 pb^{-1} , 6.1 fb^{-1} , and 23.3 fb^{-1} , respectively, were delivered. After Run 1, a long shutdown (LS1) of 2 years followed, which was used to correct the problems that were discovered in the aftermath of the incident at the startup in 2008, and to upgrade and consolidate the experiments located on the LHC ring.

In 2015, the LHC restarted operations with Run 2, at an even higher centre-of-mass energy of 13 TeV. During 2016 the design luminosity of $10^{34} \text{ cm}^{-2}\text{s}^{-1}$ was exceeded and a total of 41 fb^{-1} of data were delivered. A comparison of the delivered integrated luminosity per year is shown in Figure 3.2.

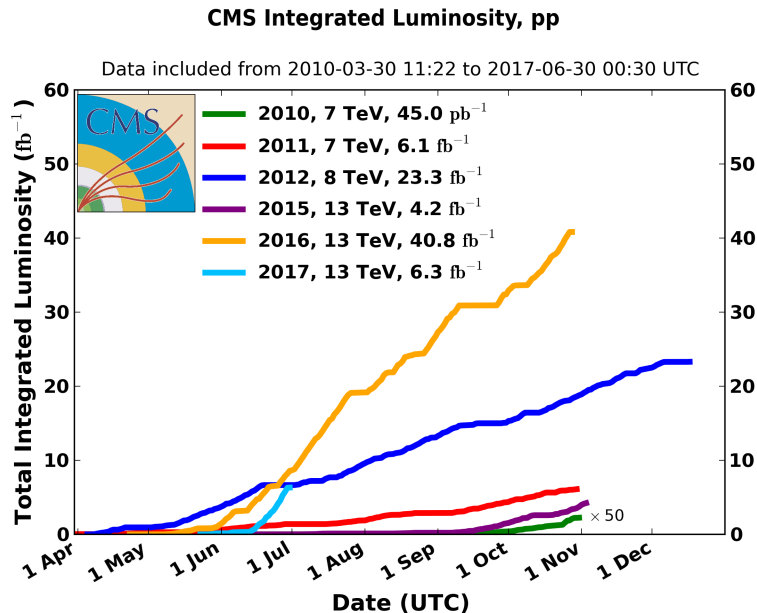


Figure 3.2: Overview of the integrated luminosity delivered to the CMS detector during Run 1 (2010 to 2012) and Run 2 (2015 to 2017).

3.1.3 The experiments at the LHC

There are four interaction points (IPs) where the proton or lead ion beams of the LHC can collide, and around each of these points large particle detectors were built in order to record the generated collisions. The ATLAS and CMS detectors, located at IP1 and IP5, are both high luminosity general-purpose detectors and consist of several layers surrounding the IP in an onion-like structure to avoid particles escaping detection. These detectors can cover a wide range of high energy physics, from precision measurements of the Standard Model to searches beyond the Standard Model. At IP2 the ALICE detector is specialized in heavy ion collisions with low instantaneous luminosities, around $10^{27}\text{cm}^{-2}\text{s}^{-1}$. With this detector information is gathered about the quark-gluon plasma, a state of matter that exists at extremely high temperatures and densities where quarks and gluons are no longer confined in hadrons. The fourth main detector, LHCb, is located at IP8 and requires instantaneous luminosities of the order of a few $10^{32}\text{cm}^{-2}\text{s}^{-1}$. Using this detector b quarks are being studied, focusing among other things on the matter-antimatter asymmetry in the universe.

3.2 The CMS detector

The searches described in this thesis were conducted using data collected with the CMS detector, a general-purpose detector located on the LHC ring. It consists of the typical components of a particle physics detector, namely a tracker, an electromagnetic calorimeter (ECAL), a hadronic calorimeter (HCAL), a solenoidal magnet, and muon detectors. One peculiar aspect is however that both calorimeters are situated inside the superconducting magnet. This design was chosen in order to improve the energy resolution by reducing the amount of material in front of the calorimeters. The overall detector has a length of 21.6 m, a diameter of 14.6 m and a total weight of 12500 t. A schematic overview is shown in Figure 3.3.

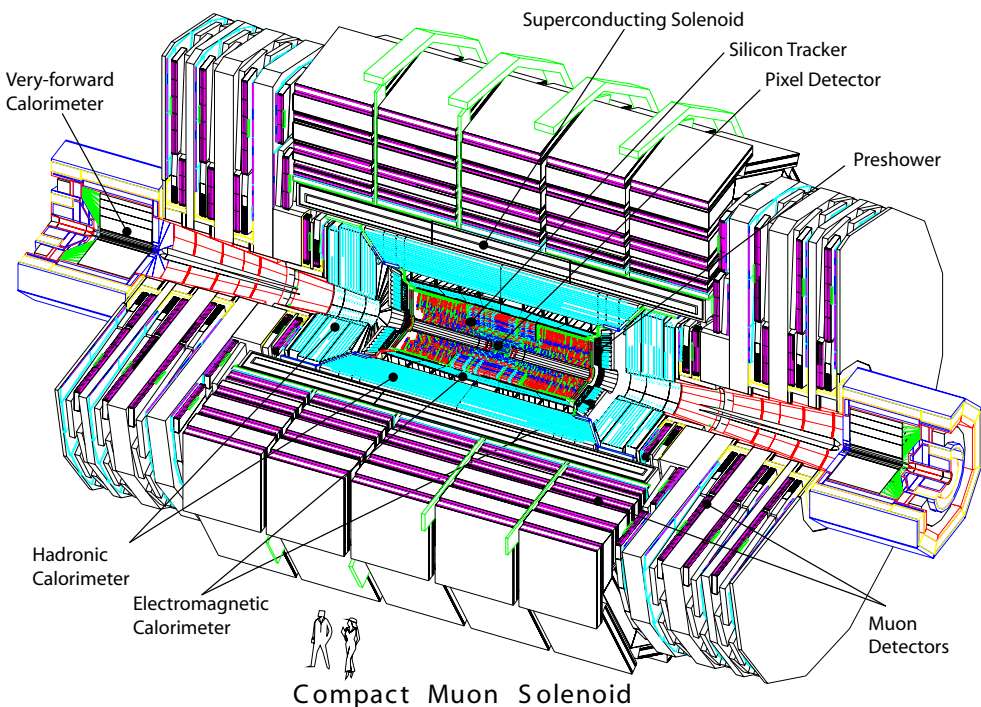


Figure 3.3: The CMS detector, consisting of the pixel and strip tracker, the electromagnetic calorimeter (ECAL) with preshower, the hadronic calorimeter (HCAL) with its forward component, and the muon systems. Figure taken from [116].

1016 The CMS coordinate system places the origin at the nominal collision point. The x axis
 1017 is perpendicular to the beam and points towards the centre of the LHC ring, the y axis is ver-
 1018 tical and pointing upwards, and the z axis is defined anticlockwise along the beam direction.
 1019 The azimuthal angle ϕ is then defined in the xy plane, relative the the x axis and the polar an-
 1020 gle θ is measured with respect to the z axis. In general, the polar angle is converted into the
 1021 pseudorapidity

$$\eta = -\ln \left(\tan \frac{\theta}{2} \right) \quad (3.3)$$

1022 for convenience, since differences in pseudorapidity are invariant under Lorentz boosts along the
 1023 z axis. A pseudorapidity of 0 corresponds to the direction perpendicular to the beam ($\theta = \pi/2$),
 1024 and an infinite pseudorapidity corresponds to the direction parallel to the beam ($\theta = 0$).

1025 Due to the conservation of momentum before and after the collision, the momenta of the
 1026 particles in the final state of a collision should be balanced in the transverse plane. Another
 1027 variable that is therefore often used in particle physics is the transverse momentum of a particle,
 1028 defined as

$$p_T = p \cdot \sin \theta. \quad (3.4)$$

1029 3.2.1 The tracker

1030 The innermost part of the CMS detector, closest to the IP, is the tracking system, which is de-
 1031 signed to provide a precise measurement of the trajectories of charged particles. This all-silicon
 1032 detector is divided into a pixel and a strip detector, with a layout as shown in Figure 3.4. The
 1033 inner part, consisting of pixel modules, provides very precise 3D hits, which are important for
 1034 vertex reconstruction and track seeding. This allows to have a precise measurement of sec-
 1035 ondary vertices and track impact parameters, necessary for the efficient identification of e.g.
 1036 heavy flavour particles. As the hit occupancy is lower in the outer part of the detector, a larger
 1037 cell size can be afforded, and silicon strips are used instead of pixels. This strip detector pro-
 1038 vides a large lever arm and a link to the calorimeters and the muon system. The tracker covers a
 1039 pseudorapidity range $|\eta| < 2.5$.

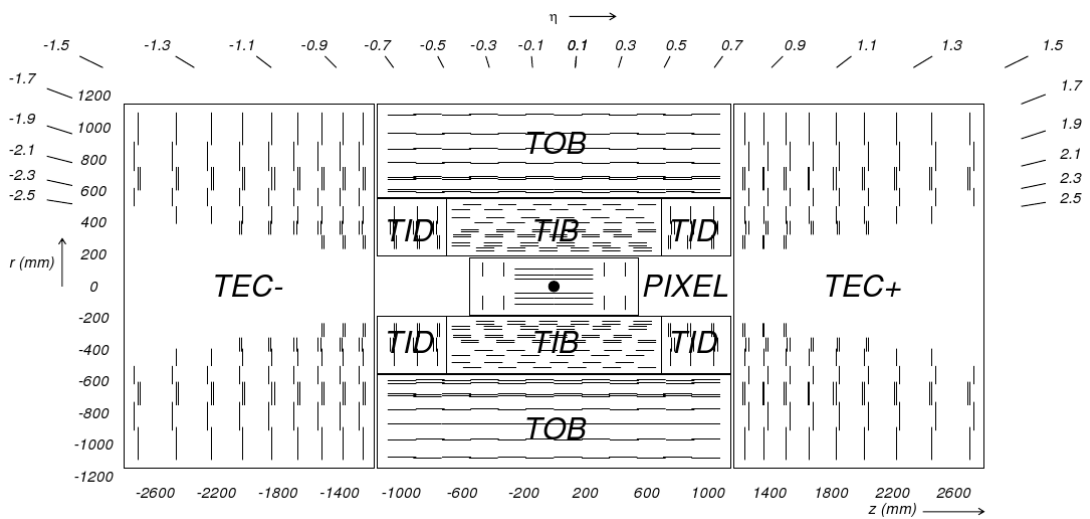


Figure 3.4: A transverse view of the pixel and strip tracker detectors. Figure taken from [116].

1040 3.2.1.1 The pixel tracker

1041 The pixel tracker was replaced during the extended technical stop in 2016 and 2017 [117], as a
 1042 part of the CMS Phase 1 upgrades. As the data used for this thesis were recorded before that,

1043 only the so-called Phase 0 detector is described here.

1044 For the pixel modules n+ pixels on n-substrate are used, allowing the sensors to also work
 1045 in under-depletion after type inversion. The 1440 modules are arranged in several cylindrical
 1046 layers and disks, as illustrated in Figure 3.4. The barrel, consisting of 3 pixel layers surrounding
 1047 the beam pipe at radii of 4.4, 7.3 and 10.2 cm, is complemented by the forward pixel detector,
 1048 composed of 2 endcap disks on each side extending from 6 to 15 cm in radius. The barrel and the
 1049 forward parts contain respectively 48 million and 18 million pixels with a size of $100 \times 150 \mu\text{m}^2$,
 1050 covering a total area of 1.06 m^2 .

1051 In the barrel, the magnetic field of CMS is perpendicular to the drift of the electrons to the
 1052 collecting pixels, which results in a Lorentz drift. This drift leads to a spread of the charge over
 1053 several pixels. Since the read-out of the modules is analogue, an improved spatial resolution
 1054 can therefore be achieved with charge interpolation. In the forward pixel detector the drift of
 1055 the electrons would be parallel to the magnetic field so in order to profit from the Lorentz angle,
 1056 the modules are tilted by 20° in a turbine-like arrangement, as can be seen in Figure 3.5. A
 1057 spatial resolution of $10 \mu\text{m}$ ($30 \mu\text{m}$) can be achieved in the local directions x (y) of the module,
 1058 respectively. In the barrel x is the longitudinal direction perpendicular to the beam and y is the
 1059 longitudinal direction parallel to the beam.

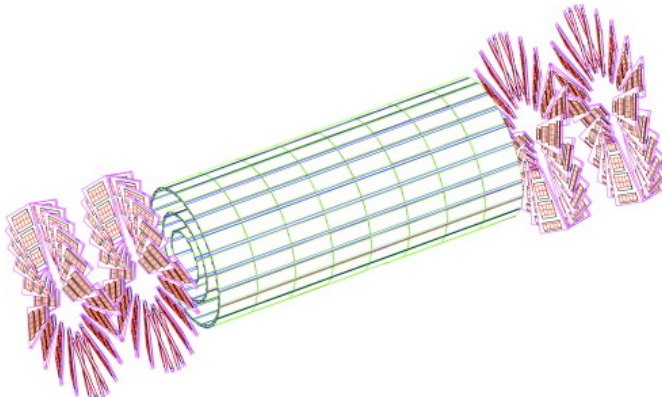


Figure 3.5: A 3D view of the barrel and forward pixel detector. Figure taken from [118].

1060 The signals from the pixel sensors are read out by custom read-out chips (ROCs), which
 1061 amplify and store the signals, and already apply zero-suppression on-detector. The data rate
 1062 from the detector to the Front End Drivers (FEDs) is therefore not constant for every event.
 1063 Additionally, if there are too many hits on a pixel module for a given event, they can not all be
 1064 stored on the finite buffer of the ROC. Consequently, as the instantaneous luminosity increases
 1065 the pixel modules start to show a “dynamic inefficiency” which is most pronounced in the first
 1066 layer, closest to the beampipe. This was one of the main motivations for the Phase 1 upgrade of
 1067 the pixel detector.

1068 **3.2.1.2 The strip tracker**

1069 The outer part of the tracker consists of 15 148 strip modules, which are distributed among
 1070 multiple barrel layers and endcap disks and make up a total active area of 198 m^2 . The inner part
 1071 is composed of 4 Tracker Inner Barrel (TIB) layers with 3 Tracker Inner Disks (TID) on each
 1072 side. Surrounding these are 6 Tracker Outer Barrel (TOB) layers and the 2 Tracker EndCaps
 1073 (TEC), which are composed of 9 disks. This geometric arrangement is shown in Figure 3.4,
 1074 with double lines to indicate back-to-back modules. These so-called double-sided modules are
 1075 mounted with a stereo angle of 100 mrad to improve the 3D point resolution by providing a
 1076 measurement of the z and r coordinate in the barrel and disks, respectively. The choice of strip
 1077 pitches is driven by the two particle separation capability and two-hit resolution, and ranges

1078 from 80 μm to 205 μm . The length of the strips varies from 63 mm to 117 mm, minimizing the
 1079 occupancy and noise levels.

1080 In the TOB and the 3 outermost rings of the TEC two silicon sensors are daisy chained, while
 1081 single sensors are used in the inner part. This is done to limit the number of read-out channels,
 1082 since the area that had to be instrumented is larger in the outer region. The larger cell size can
 1083 be afforded due to the lower occupancy in the outer part. However, the noise of the sensors also
 1084 increases with strip length, so thicker silicon sensors, 500 μm compared to 320 μm in the inner
 1085 part, are used in order to collect more signal per traversing particle.

1086 The strip sensors are single sided p-on-n type silicon. The signals from the sensors are
 1087 amplified, shaped, and stored by 4 or 6 custom APV25 chips per module. When the trigger has
 1088 made a positive decision, the analogue signals from two APV25 chips are multiplexed and sent
 1089 to the FED boards in the service cavern via optical fibres, where they are converted to digital
 1090 signals. The FEDs then perform pedestal and common mode subtraction as well as cluster
 1091 finding. Additionally, the data is sparsified in these off-detector electronics, before being sent to
 1092 the CMS central data acquisition (DAQ). Due to charge sharing, this analogue read-out scheme
 1093 also results in an improved spatial resolution of 15 to 40 μm , depending on the position of the
 1094 modules and the strip pitch.

1095 3.2.2 The electromagnetic calorimeter

1096 Surrounding the tracker, the CMS electromagnetic calorimeter (ECAL) is designed to measure
 1097 the energy of photons and electrons. It is composed of 75 848 lead tungstate (PbWO_4) crystals
 1098 arranged in a cylindrical barrel and 2 endcaps. The barrel crystals measure $22 \times 22 \text{ mm}^2$ at the
 1099 front face of crystal, and $26 \times 26 \text{ mm}^2$ at the rear face, which corresponds to approximately
 1100 0.0174×0.0174 in $\eta\phi$. The length of the crystal is 230 mm, corresponding to 25.8 radiation
 1101 lengths. In the endcaps, the crystals have a rear face cross section of $30 \times 30 \text{ mm}^2$, front face
 1102 cross section of $28.62 \times 28.62 \text{ mm}^2$, and a length of 220 mm, corresponding to 24.7 radiation
 1103 lengths. The crystals are arranged such that they are off-pointing with respect to the centre of
 1104 the detector, and instead point at a focus 1.3 m beyond the interaction point, in order to avoid
 1105 cracks between the crystals to be aligned with the trajectories of the particles.

1106 The high density material was chosen due to its short radiation length and small Molière ra-
 1107 dius, resulting in a small lateral spread of the electromagnetic shower generated by an incoming
 1108 photon or electron. This allows for a fine granularity, a better shower separation, and a compact
 1109 calorimeter. Additionally, this scintillating material has a fast response, as about 80% of the light
 1110 is emitted during the first 25 ns. The scintillation light is collected by photodetectors, digitized,
 1111 and read out.

1112 The layout of the ECAL is shown in Figure 3.6, with the barrel (EB) extending up to $|\eta| <$
 1113 1.470 and the endcaps (EE) on each side covering the range $1.479 < |\eta| < 3.0$. A preshower
 1114 detector (ES) is positioned in front of the endcap crystals, covering the pseudorapidity range
 1115 between $|\eta| = 1.653$ and $|\eta| = 2.6$. This detector consists of a layer of lead which initiates an
 1116 electromagnetic shower from incoming photons or electrons, and a layer of silicon sensors which
 1117 measures the deposited energy. The main goal of this 20 cm thick detector is to discriminate
 1118 between photons and neutral pions.

1119 The energy resolution of calorimeters can be parametrized by the following stochastic (S),
 1120 noise (N), and constant (C) terms:

$$\left(\frac{\sigma}{E}\right)^2 = \left(\frac{S}{\sqrt{E}}\right)^2 + \left(\frac{N}{E}\right)^2 + C^2 \quad (3.5)$$

1121 The stochastic term represents contributions from the shower containment, the number of pho-
 1122 toelectrons and the fluctuations in the gain process. The noise term takes into account all noise
 1123 components, such as electronics and digitization noise. Finally, the constant term characterizes
 1124 among others energy leakage from the back of the calorimeter crystals and non-uniformities of

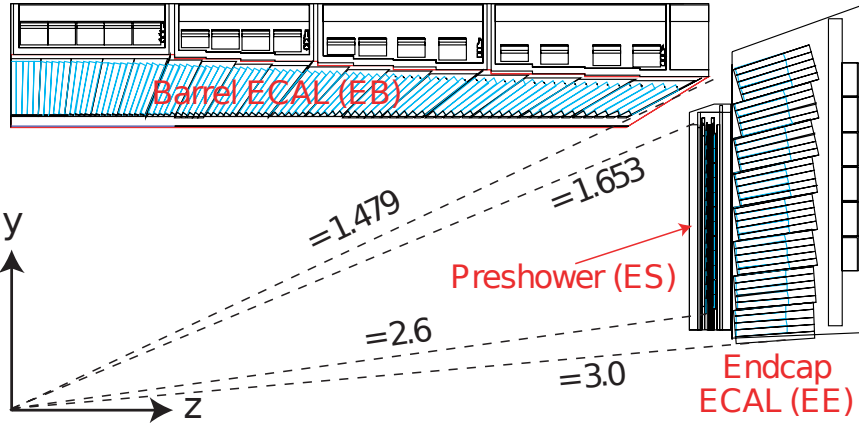


Figure 3.6: A transverse view parallel to the beamline showing one quarter of the ECAL, with its barrel (EB), endcap (EE), and preshower (ES) detectors. Figure taken from [118].

1125 the longitudinal light collection. The latter term dominates the energy resolution for high-energy
 1126 electron and photon showers. Figure 3.7 shows the energy dependence of this resolution for in-
 1127 cident electrons as measured in a beam test, as well as the determined stochastic, noise, and
 1128 constant terms obtained by fitting equation 3.5 to the data.

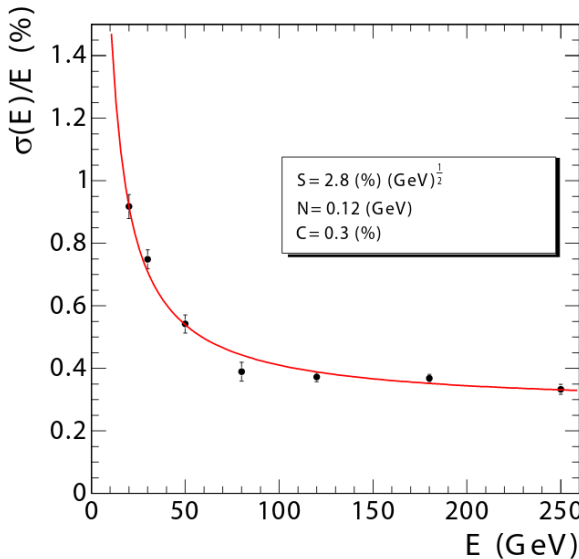


Figure 3.7: The ECAL energy resolution as a function of the electron energy, measured from a beam test. The stochastic (S), noise (N), and constant (C) are given as well. Figure taken from [116].

1129 A more recent measurement of the energy resolution was performed using electrons from
 1130 Z boson decays in collision data. In the central region, up to $|\eta| < 0.8$, it was measured to be
 1131 better than 2%. Outside of this region, in the more forward direction, the energy resolution is
 1132 2-5% [119]. The reconstruction of the electrons and photons will be discussed in Section 4.3.2.

3.2.3 The hadronic calorimeter

The hadronic calorimeter (HCAL) surrounds the ECAL with the aim to measure the energy of charged and neutral hadrons. The missing transverse energy can then be inferred from this measurement together with the measured energies in the ECAL, in order to identify neutrinos or exotic particles. The HCAL consists of brass absorber plates interleaved with plastic scintillator tiles.

Figure 3.8 shows a longitudinal quarter view of the different HCAL components. A cylindrical barrel (HB) covers the region up to $|\eta| < 1.4$ and is complemented by endcaps (HE) on each side, extending the pseudorapidity range to $|\eta| < 3.0$. In the central region, the stopping power of the ECAL and HCAL barrel is not sufficient to contain the entire hadron showers of very energetic jets. The HCAL was therefore extended outside the solenoid with an outer calorimeter (HO), which uses the magnet coil as absorber and consists of scintillators. Two layers are positioned at $\eta = 0$, where the absorber depth is minimal, and only 1 layer is used for the 2 rings on each side of the central ring. Finally, a forward calorimeter (HF) is positioned at 11.2 m from the IP covering $3.0 < |\eta| < 5.2$. Unlike the other HCAL components, this detector consists of iron and quartz fibres, which are radiation-hard. This is an important aspect for the choice of active material since it is exposed to very large particle fluxes. A signal is generated by the charged shower particles which generate Cherenkov light.

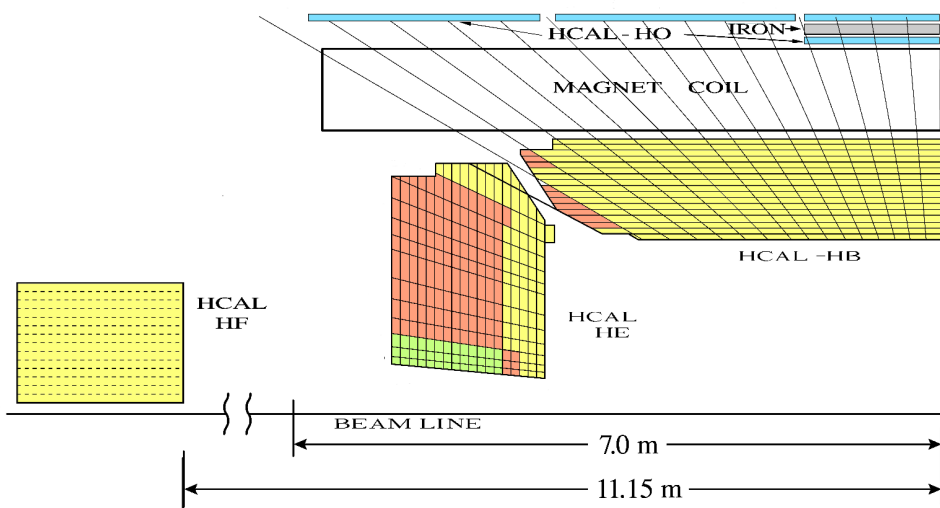


Figure 3.8: A quarter view of the hadronic calorimeter (HCAL), parallel to the beamline. The barrel (HB), endcap (HE), outer (HO), and forward (HF) detectors are indicated. Figure taken from [116].

The optical signals from the scintillators in the HB and HE are converted to electrical signals by multichannel hybrid photodiodes, while silicon photomultipliers (SiPMs) are used in the HO. In the HF, the Cherenkov light emitted in the quartz fibres is detected by standard photomultiplier tubes (PMTs), since the magnetic field is much smaller in this region.

The expected transverse energy resolution for jets reconstructed from calorimeter information is shown in Figure 3.9 for various pseudorapidity regions: barrel jets ($|\eta| < 1.4$), endcap jets ($1.4 < |\eta| < 3.0$), and very forward jets ($3.0 < |\eta| < 5.0$). Details about the reconstruction of jets from calorimeter and tracking information will be given in Section 4.3.7.

3.2.4 The muon system

The outermost detector, located entirely on the outside of the solenoid, is a dedicated muon detection system. The purpose of this subsystem is muon identification, momentum measurement,

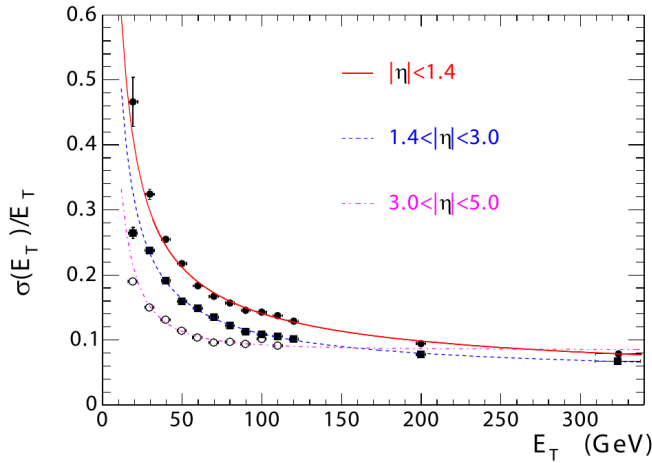


Figure 3.9: The jet transverse energy resolution as a function of the jet transverse energy, for barrel jets ($|\eta| < 1.4$), endcap jets ($1.4 < |\eta| < 3.0$), and very forward jets ($3.0 < |\eta| < 5.0$). Figure taken from [116].

and triggering. As illustrated in Figure 3.10, the layers of muon chambers are embedded in the iron yoke constraining the magnetic field lines. The strong magnetic field completely saturates the return yoke with a field of about 2 T, in opposite direction with respect to the field inside the magnet.

Three different types of gas-ionisation detectors are used. In the barrel, Drift Tubes (DTs) are installed, covering the pseudorapidity range up to $|\eta| < 1.2$, while Cathode Strip Chambers (CSCs) are used in the endcap region ($0.9 < |\eta| < 2.4$). The DTs are designed for the low muon rates that are expected in the barrel and thus have a slower response time than the CSCs, which are used at larger pseudorapidities due to the higher flux and the larger and non-uniform magnetic field. Resistive Plate Chambers (RPCs) complement the DT and CSC systems in the pseudorapidity region up to $|\eta| < 1.8$. They have a good time resolution but a worse spatial resolution than the DTs or CSCs, and provide a fast response which is much shorter than the 25 ns between 2 consecutive bunch crossings, making them very well suited to trigger on muons.

The offline muon reconstruction efficiency in simulated events containing one muon is typically between 95% and 99%, except for the regions between 2 DT wheels ($|\eta| = 0.25$ and $|\eta| = 0.8$) and the transition region between the DTs and CSCs ($|\eta| = 1.2$), where the efficiency drops to 92%. The reconstruction of muons using the information from the tracker and the muon detectors will be detailed in Section 4.3.4. For central muons with a small momentum, the offline momentum resolution of the standalone muon system is about 9%. At momenta around 1 TeV, the resolution varies from 15% to 40%, depending on the pseudorapidity. As demonstrated in Figure 3.11, performing a global momentum fit using the tracker as well improves the resolution by an order of magnitude at low muon momenta. At high momenta the resolution of the full system is about 5%.

3.2.5 Trigger and data acquisition

Collisions are provided by the LHC at high interaction rates, with an interval of 25 ns between bunch crossings. This corresponds to a frequency of 40 MHz. Additionally, multiple collisions occur at the same time, depending on the luminosity. Since it is impossible to store and process the large amount of data produced in the collisions at this high rate, a severe rate reduction is needed. This rate reduction is performed by the trigger system, which decides whether to store or reject an event. Since this decision process is constrained in time, the computing time is optimized by rejecting uninteresting events as quickly as possible. The rate is reduced to 1 kHz

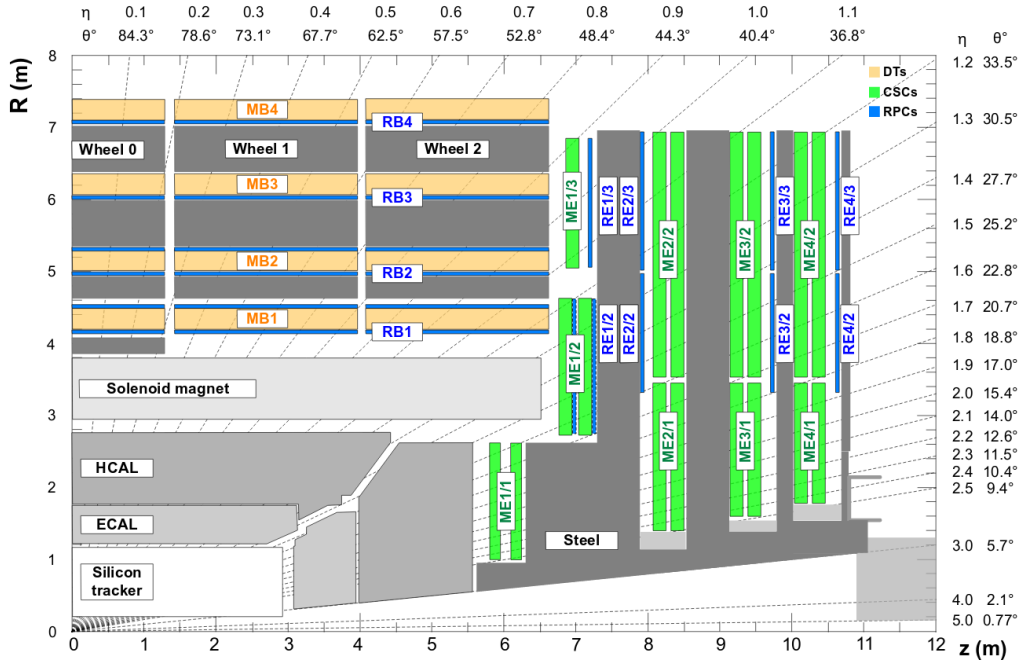


Figure 3.10: A transverse view of one quarter of CMS showing the position of the 3 types of muon detectors. The Drift Tube (DT) are located in the barrel, the Cathode Strip Chamber (CSC) in the endcaps, and the Resistive Plate Chamber (RPC) in both regions up to $|\eta| < 1.8$. Figure taken from [120].

in two steps by the Level-1 (L1) Trigger and the High-Level Trigger (HLT).

The L1 Trigger decision is based on information from the calorimeters and muon systems, following the structure illustrated in Figure 3.12. At the lowest level, the Local Triggers are based on energy deposits in calorimeter towers and track segments or hit patterns in the muon system. Regional triggers, indicated as Calo Trigger Layer 1 and Muon Track-Finder Layer in the figure, then combine this information and use pattern logic to determine trigger objects such as jet or muon candidates in separated spatial regions. The candidates are ranked based on their energy or momentum and quality, reflecting the level of confidence assigned to the L1 parameter measurements. Finally, the Calo Trigger Layer 2 and the Global Muon Trigger (GMT) determine the highest-rank calorimeter and muon objects across the whole detector and transfer them to the Global Trigger, which makes the final decision to accept or reject an event. Following this procedure, the L1 Trigger thresholds are tuned to reduce the event rate and keep it below 100 kHz. The L1 Trigger is composed of custom electronics located partially on the detectors, and partially in the underground service cavern. The L1 decision needs to be made and distributed to the detector front-end electronics within 3.8 μ s [121].

The readout of the data proceeds as illustrated in Figure 3.13. When an event is accepted by the L1 Trigger, the data from about 740 FEDs is read out by the Readout Units (RUs). For so-called *legacy* systems, i.e. systems which are using VME-based hardware from the initial installation, the FEDs are read out by custom Front-End-Readout-Link (FRL) cards, while for systems that changed their readout architecture from the VME standard to the newer μ TCA standard during or after LS1 they are read out via the newer Front-End-Readout-Optical-Link (FEROL) cards. The event fragments are then sent over the event-builder switch to the Builder Units (BUs), which assemble the events. Next, the events are distributed to the Filter Units (FUs) by a large switch network.

The HLT software system is implemented in this filter farm, which uses more than 15 000 CPU cores for the final event selection. In this second step, the HLT reduces the event rate

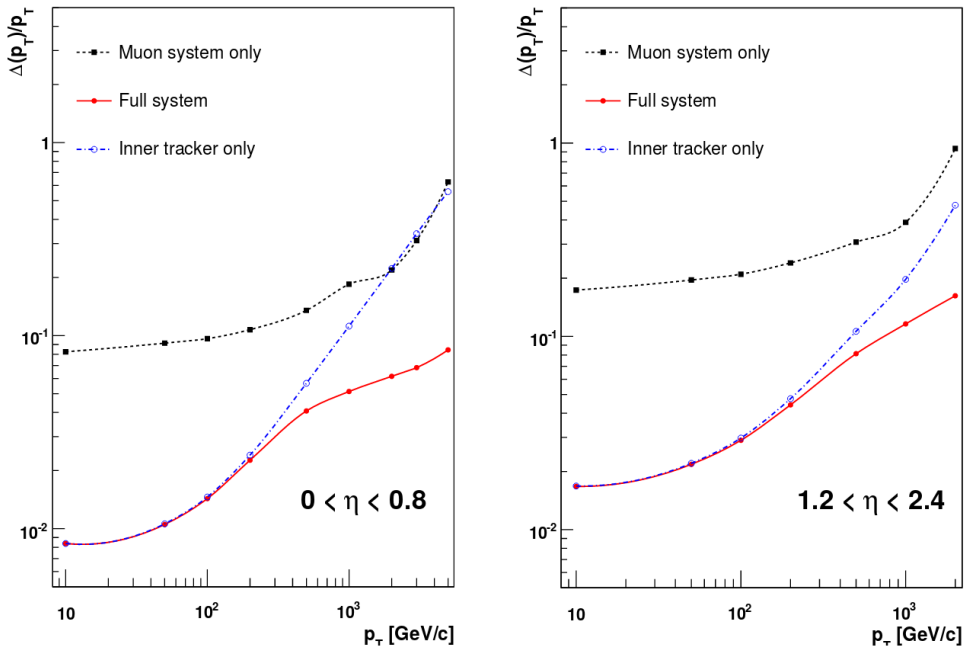


Figure 3.11: The muon transverse momentum resolution as a function of transverse momentum for low (left) and (high) pseudorapidities. The resolution is shown for the muon system and the tracker separately, and for the full system. Figure taken from [116].

further to 1 kHz. The complete read-out data, including information from the pixel and strip tracker, are available for this step. New objects can therefore be reconstructed such as e.g. tau leptons and b-jets, as is done in the offline software, but speed-optimized.

3.2.6 CMS performance in Run 2

The number of collisions recorded at the experiments will differ from the amount delivered by the LHC. Data loss can be caused by e.g. problems with a particular subdetector, data acquisition, the trigger rate, or the infrastructure. During Run 2, CMS achieved a data taking efficiency of 89% and 92% in 2015 and 2016, respectively. The comparison between the delivered and recorded cumulative integrated luminosity in 2016 is shown in Figure 3.14. Subsequently, the recorded data is certified by the offline Data Quality Monitoring (DQM), to ensure that the data are suited for physics analysis. The efficiency of this certification process with respect to the amount of recorded data was 80% in 2015 and 96% in 2016. This is shown in Figure 3.14 as well for 2016.

The detector was in good condition during data taking in 2015 and 2016. Figure 3.15 shows the active fraction of channels per subdetector, and the evolution from 2015 to 2016. In 2016, all subdetectors have an active fraction higher than 97.5%, except for the strip tracker, which has the largest number of channels and has an active fraction well above 95%. For this subdetector, channels that are not included or masked are accounted for, as well as channels that are identified as out-of-sync or irresponsible by the back end electronics, or as too noisy or inefficient from further analysis.

3.2.6.1 Pre-amplifier saturation in the APV25 chip

During Run 2, the instantaneous luminosity delivered by the LHC increased continuously, and even exceeded the design luminosity of $10^{34} \text{ cm}^{-2}\text{s}^{-1}$ in 2016. As the luminosity increased, a dynamic inefficiency appeared in the strip tracker, which was most noticeable in the first layer

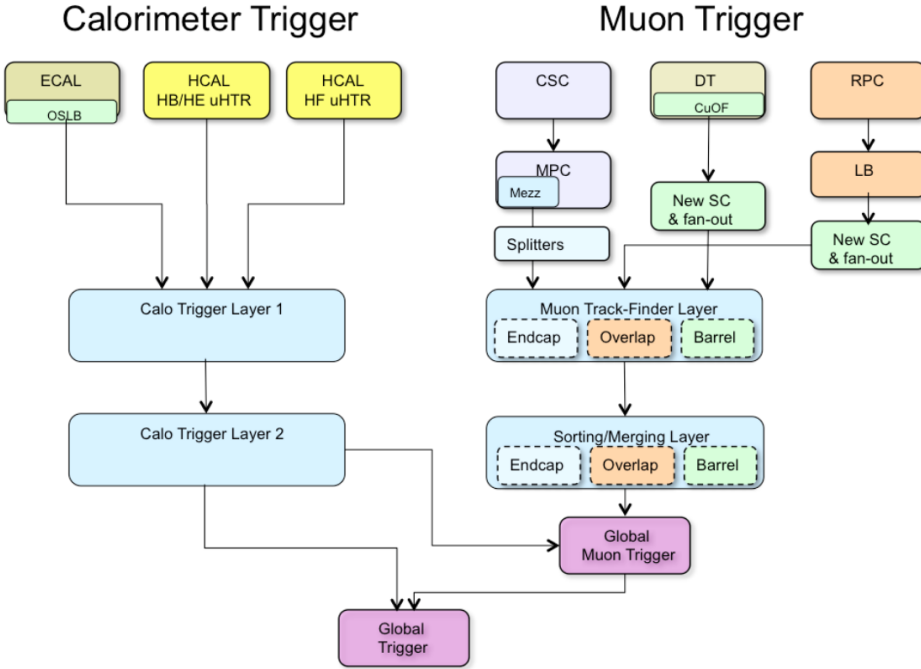


Figure 3.12: Schematic overview of the L1 Trigger. Figure taken from [121].

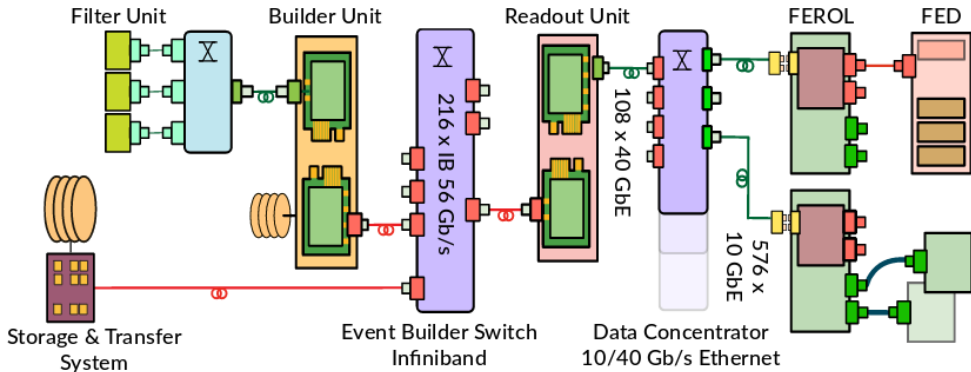


Figure 3.13: Schematic of the data acquisition (DAQ) system. Figure taken from [122].

of the TOB. The symptoms were a change in the signal-to-noise ratio and loss of hits. As can be seen from Figure 3.16, the most probable value (MPV) of the signal-to-noise ratio is shifted towards lower values and the low tail increased as well. The loss of hits is clearly visible in Figure 3.17, showing the change in number of hits per track for increasing instantaneous luminosities. The run periods indicated in the plot refer to a subset of the data taken over the course of the year. Run period boundaries are typically defined by changes in the LHC running conditions, changes to the detector configuration or calibration, or other parameters. The number of hits decreases for later run periods such as D and F, as the instantaneous luminosity increases. This loss of hits results in less and shorter tracks.

The origin of this inefficiency was eventually tracked down to saturation effects in the pre-amplifier of the APV25 chip. The pre-amplifier decay time changes significantly with temperature. As the operating temperature of the strip tracker was lowered from $+4^{\circ}\text{C}$ to -15°C coolant temperature during LS1, the decay time was no longer sufficient to cope with the high luminosities. The dynamic inefficiency was cured in August 2016 by changing the pre-amplifier drain

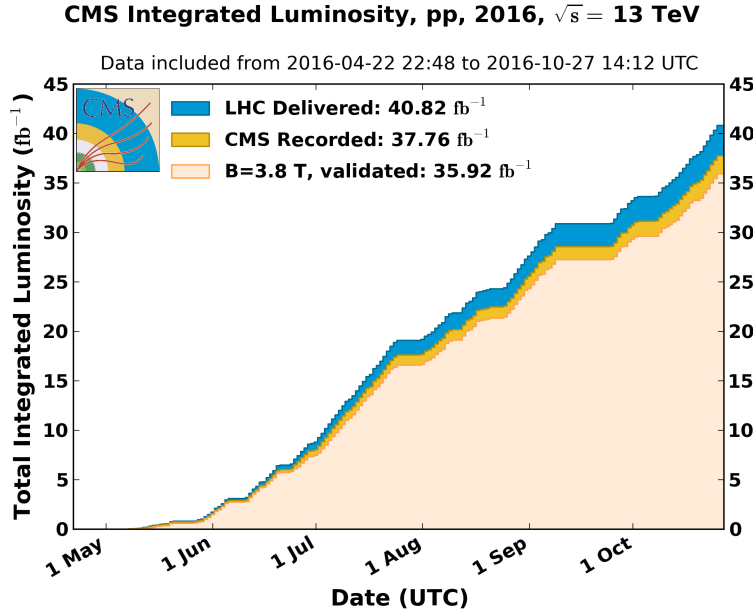


Figure 3.14: The cumulative distribution of the instantaneous luminosity delivered by the LHC (blue), recorded by CMS (yellow), and certified as good for physics analysis (light orange) in 2016. Figure taken from [123].

speed. This led among other things to the recovery of the muon efficiency, which showed a large drop for the highest luminosities before the change and an essentially flat behaviour afterwards, as demonstrated in Figure 3.18. This is a crucial effect, for example for the analysis described in Chapter 6, where the difference between the two drain speed settings is clearly visible.

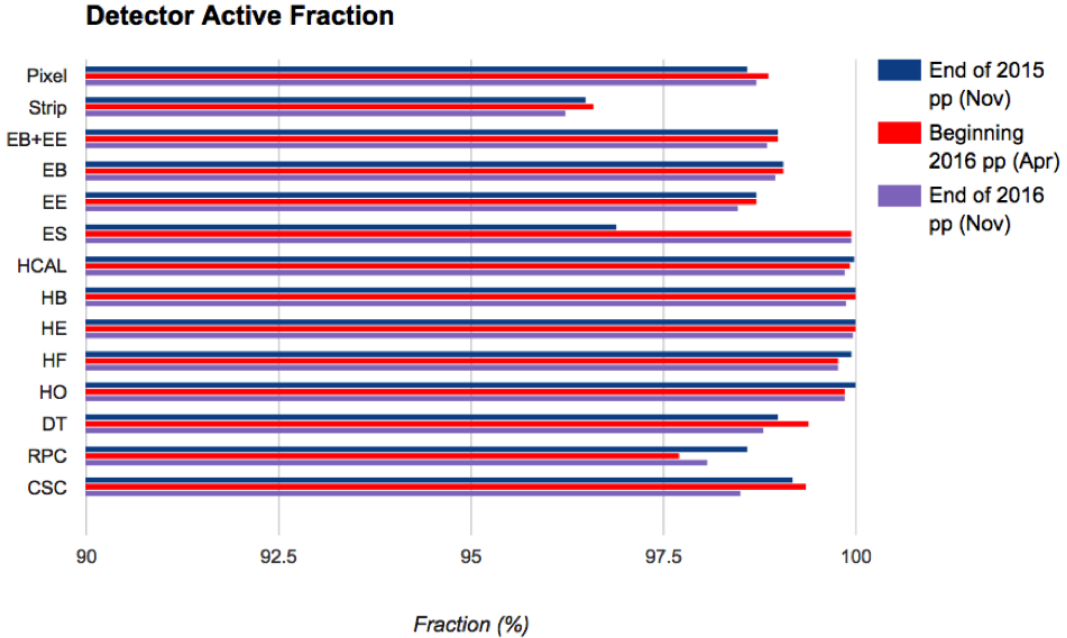


Figure 3.15: Fraction of active channels per subdetector, compared for the end of data taking in 2015, and the beginning and end of data taking in 2016. Figure taken from [124].

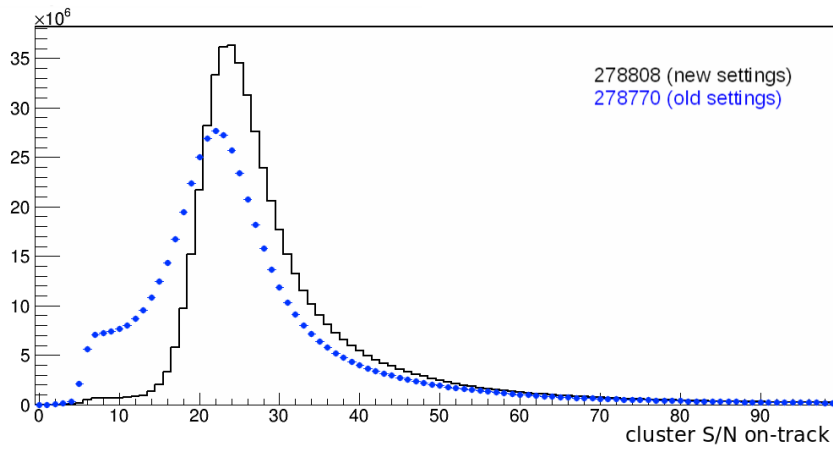


Figure 3.16: The signal-to-noise ratio for clusters on reconstructed tracks in the first layer of the TOB for two different runs in summer 2016. The first run (blue) is affected by the saturation effects in the APV25 pre-amplifier, resulting in a downward shift of the peak and an increase of the distribution at low values. In the second run (black), after the change of pre-amplifier drain speed, the distribution has its standard shape again. Figure taken from [125].

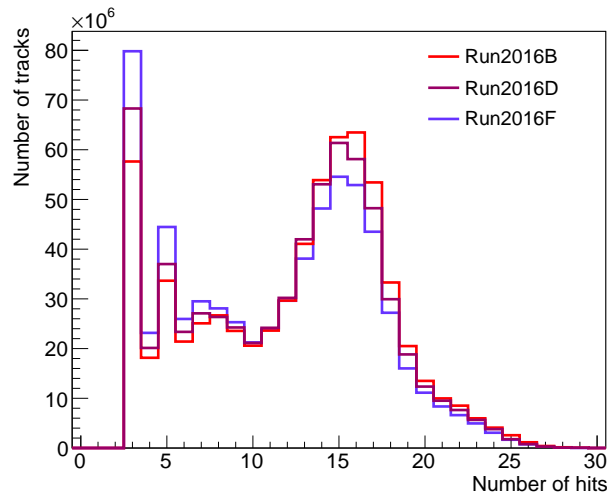


Figure 3.17: The number of hits per track for run periods B, D, and F, showing the effect of the increasing instantaneous luminosity.

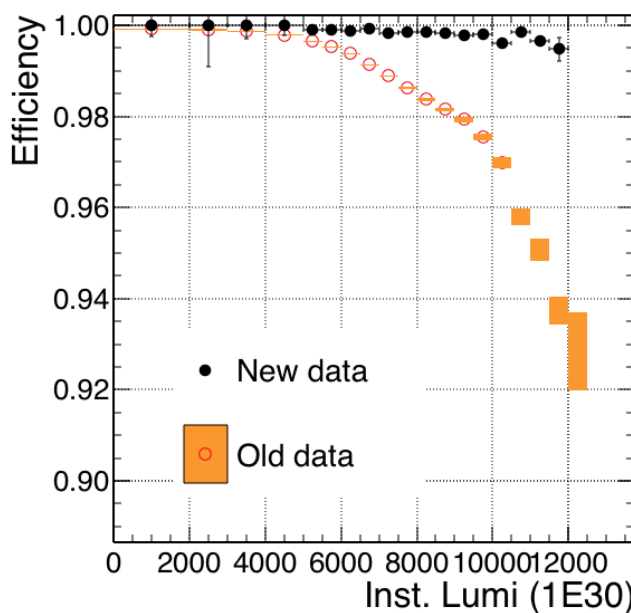


Figure 3.18: The muon efficiency as a function of the instantaneous luminosity for before (orange) and after (black) the change of pre-amplifier drain speed which cured the dynamic inefficiency. Figure taken from [125].

4

1261

1262

Event Simulation and Reconstruction

1263 In order to use the recorded data, the obtained signals coming from various parts of the detector
1264 must be reconstructed to be able to identify the particles in the event. Additionally, to com-
1265 pare the experimental results with theory, events are generated and the resulting signals in the
1266 detector are simulated, as detailed in Sections 4.1 and 4.2, respectively. The event reconstruc-
1267 tion is detailed in Section 4.3. Finally, some details about the simulation of SIMPs are given in
1268 Section 4.4.

1269 4.1 Event generation

1270 The event structure at the LHC is complicated by the composite nature of the colliding protons,
1271 as demonstrated in Figure 4.1. This sketch shows the hard interaction in red, with a tree-like
1272 structure surrounding it, representing the ensuing shower. In this hard scattering, the quark or
1273 gluon constituents of the protons, called partons, will interact according to a so-called parton
1274 distribution function (PDF), which is determined by the parton’s momentum fraction and the
1275 momentum transfer. Due to their colour charge, the partons involved in the hard interaction will
1276 induce parton showers consisting of a cascade of radiation from QCD processes. This is shown
1277 in blue for the incoming partons and in red for the outgoing partons. The produced partons
1278 will also hadronize due to colour confinement, as illustrated in green, with hadron decays in
1279 dark green and radiated photons in yellow. Finally, the purple interaction represents a second
1280 interaction between the proton remnants. Next to these multiple parton interactions, additional
1281 activity in the event can also come from pileup. All these aspects must be taken into account
1282 when generating events, as detailed below.

1283 Hard scattering

1284 In the hard interaction, two partons of the colliding protons, will interact with a certain
1285 probability at a given momentum transfer. This is parametrized by the PDFs $f(x, Q^2)$,
1286 were x is the proton’s momentum fraction and Q^2 is the momentum transfer scale. Experi-
1287 mentally determined PDFs are available from various groups, including e.g. CTEQ [127],
1288 MRST/MSTW [128], and NNPDF [129]. An example of such PDFs obtained by the
1289 NNPDF group is shown in Figure 4.2. This figure shows that the valence quarks in the
1290 proton, namely the up and down quarks it is made of, have a larger momentum fraction
1291 than the remaining sea quarks, which appear as virtual quark-antiquark pairs forming from
1292 gluons and annihilating again. The PDFs are then convoluted with the matrix element of
1293 the hard scattering, which is the process of interest where the two colliding partons create

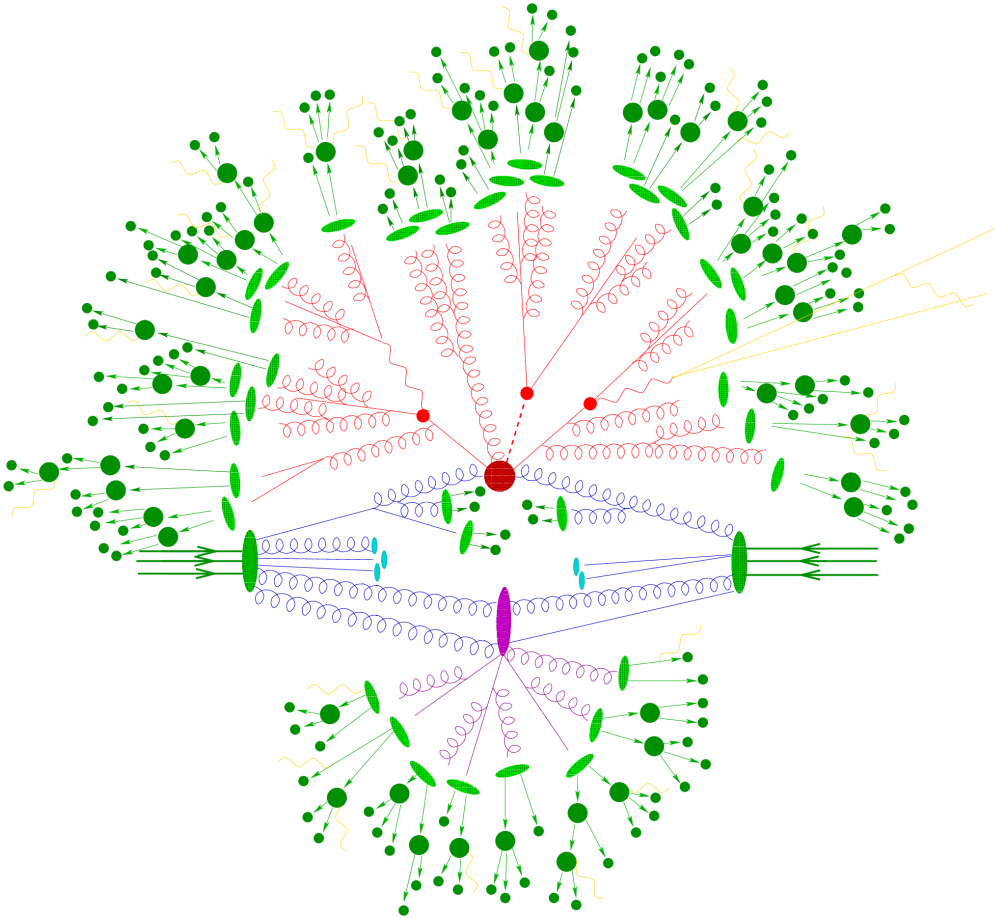


Figure 4.1: Illustration of an event showing the hard scattering, parton shower, hadronisation, and underlying event. Figure taken from [126].

1294 high-energetic final state particles. This is done using an event generator, such as MAD-
 1295 GRAPH5_aMC@NLO [130] and POWHEG [131]. With MADGRAPH5_aMC@NLO the
 1296 matrix element can for many processes be calculated at tree-level or leading order (LO),
 1297 and since the addition of aMC@NLO at next-to-leading order (NLO) as well. This gen-
 1298 erator was used to produce most of the background processes for the Monojet analysis
 1299 detailed in Chapter 5 and for the SIMP signal used in Chapter 6. POWHEG is able to
 1300 generate events using NLO computations, but only for a relatively limited number of
 1301 physics processes. This generator was used to produce the monojet signal samples and
 1302 the background processes from single-top production. Since NLO calculations are more
 1303 time-consuming, one can instead use the less precise method of scaling a LO cross section
 1304 to the NLO level by using a so-called k-factor, defined as the ratio of the NLO and LO
 1305 cross sections. However, these k-factors often need to be determined as a function of the
 1306 relevant kinematic variables as they depend on the kinematic phase space and the probed
 1307 energy scale.

1308 Parton showering

1309 Since the colliding partons have a colour charge, the hard scattering will be accompanied
 1310 by a cascade of radiation from QCD processes. The partons will for example radiate soft
 1311 gluons or split into two collinear partons. This radiation can originate from the incoming
 1312 partons, which is referred to as initial state radiation (ISR), or the outgoing partons in
 1313 the final state, the so-called final state radiation (FSR). The perturbative evolution of the
 1314 cascade can be modelled using the DGLAP (Dokshitzer-Gribov-Lipatov-Altarelli-Parisi)

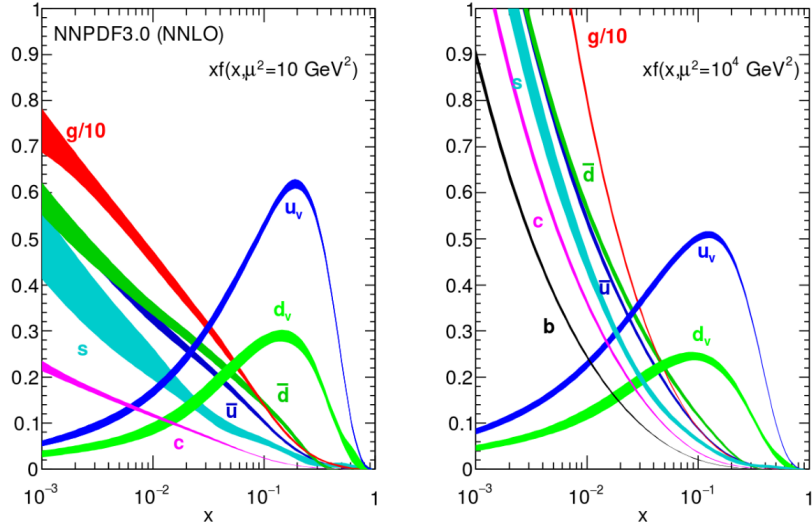


Figure 4.2: The parton distribution functions multiplied by the momentum fraction x at energy scales $Q^2 = 10 \text{ GeV}^2$ (left) and $Q^2 = 10000 \text{ GeV}^2$ (right), obtained in the NNLO NNPDF 3.0 global analysis. Figures taken from [129].

equations [132–134]. These equations describe the time evolution of the probability of a ‘mother’ parton to split into ‘daughter’ partons at an energy scale Q^2 . The momentum of the mother is then divided among the daughter partons, which can in turn split into other partons at a lower Q^2 scale. The cascade continues down to an energy scale Λ_{QCD} where the strong interaction becomes non-perturbative. The resulting number of jets can vary depending on the modelled process.

Hadronisation

The next step after the showering is the hadronisation of the coloured particles produced in the parton shower, transforming them into colour-neutral hadrons. Since this happens at low energy scales where the perturbative approach of QCD is not valid, phenomenological models have to be used. For most of the processes considered in this thesis, the showering and hadronisation is done with PYTHIA 8 [135], using a standard set of parameters which were tuned to reproduce the experimental data. In PYTHIA, the string Lund model [136] is used, based on string fragmentation. This model starts from the idea of a string connecting a quark q and an antiquark \bar{q} , following the assumption of linear confinement. As the two quarks move away from each other, the string stretches and the potential energy stored in the string increases. The increase in potential energy is assumed to be proportional to the distance between the quarks. When the energy becomes sufficient to produce a new pair of quarks $q'\bar{q}'$ with mass m , the string breaks and the original quark pair is split into two new pairs, $q\bar{q}'$ and $q'\bar{q}$. If the invariant mass of the new strings is large enough, the same process is repeated, leading to a new break-up. This procedure continues until only colour-neutral hadrons with an on-shell mass remain.

Additional activity in the event

In addition to ISR and FSR, also beam remnants and multiple parton interactions give rise to additional activity in the event, referred to as the underlying event. After the partons participating in the hard scattering are extracted, the remainder of the protons have a non-zero colour charge. The creation of additional hadrons during the hadronisation is therefore possible. Multiple parton interactions represent additional interactions which can take place between other incoming partons. As the probability for an additional hard interaction to occur is rather small, the activity from multiple parton interaction is typically much

1345 less energetic than the hard interaction, producing mostly low energetic hadrons. Finally,
 1346 additional collisions between other protons in the same bunch crossing, or from a previ-
 1347 ous or future bunch crossing, respectively referred to as in-time and out-of-time pileup,
 1348 add extra activity in the event. The pileup distribution is for example shown in Figure 4.3
 1349 for QCD dijet events recorded in 2016, and is compared to simulated QCD events. This
 1350 shows that there were about 20 collisions per bunch crossing on average. Typically, the
 1351 simulation does not completely agree with the data and needs to be reweighted in order to
 1352 match the data.

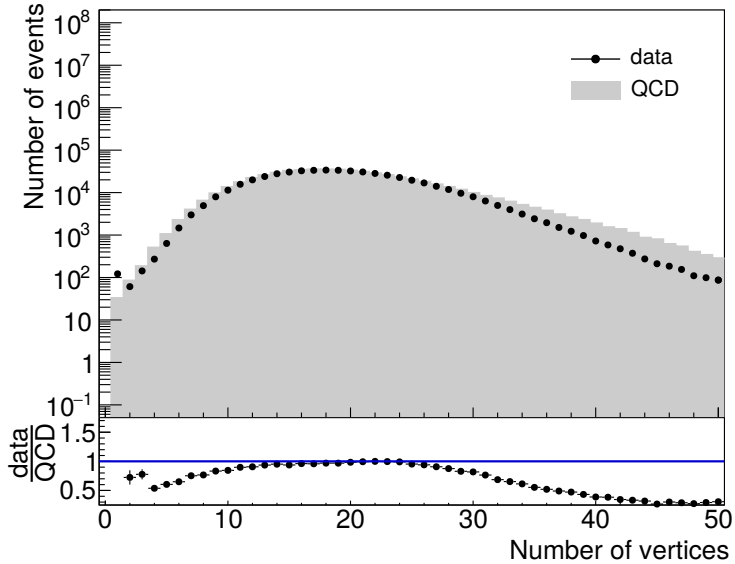


Figure 4.3: The distribution of the number of vertices for QCD dijet events recorded in 2016 compared to simulated QCD events.

1353 4.1.1 Generation of the monojet signals

1354 In the monojet analysis, the simplified models described in Section 2.2.4 are considered. The
 1355 used signal samples were generated with POWHEG, which can generate NLO vector and axial-
 1356 vector mediator production and LO scalar and pseudoscalar production. The samples were
 1357 also produced at LO with MCFM [137] as a cross check. The scanned mediator masses are
 1358 $m_\phi = 10, 20, 50, 100, 200, 300, 500, 1000, 2000, 10\,000 \text{ GeV}$, for dark matter masses of $m_\chi =$
 1359 $1, 10, 50, 100, 150, 500, 1000 \text{ GeV}$, with $m_\chi \leq m_\phi$.

1360 4.1.2 Generation of the SIMP signal

1361 For the generation of the SIMP signal, the model Lagrangian given in equation 2.22 is imple-
 1362 mented in FEYNRULES 2.0 [138]. The matrix element is then calculated at LO and events
 1363 are generated using MADGRAPH 5. The subsequent parton shower and hadronisation is done
 1364 with PYTHIA 8, using tune CUEP8M1. Several samples were produced, with SIMP masses
 1365 $m_\chi = 1, 10, 100, 200, 400, 700, 1000 \text{ GeV}$. The corresponding production cross sections are
 1366 given in Table 4.1.

m_χ [GeV]	$\sigma_{\bar{\chi}\chi}$ [pb]
1	4.46
10	4.40
100	2.55
200	0.790
400	0.0743
700	0.00485
1000	0.000571

Table 4.1: Production cross section for each SIMP mass, after $|\eta_\chi| < 2.5$ and $p_T^\chi > 200$ GeV generator level cuts.

4.2 Detector simulation

After being generated, the collision events are passed on to the CMS detector simulation, which is based on the GEANT 4 [139] simulation toolkit. This toolkit provides a description of the interaction between particles and the detector material, including effects such as bremsstrahlung of charged particles, photon conversions, energy loss of charged particles by ionization, and the showering of electrons, photons and hadrons in the calorimeters due to interaction with the material. The CMS simulation package contains the geometry of the detector with all the sensitive layers designed to detect the traversing particles, as well as the dead material regions consisting of e.g. support structures, cables and cooling pipes. A precise map of the magnetic field is also included in order to simulate the curvature of the charged particles correctly.

Next, the impact of the detector, coming from the electronic response produced by the hits in the active detector material, the digitization, the data transmission, and any reconstruction performed in the electronics such as zero-suppression or cluster reconstruction, is simulated. In this way, an event content similar to the output of the real detector is obtained. At this point the effect of pileup is also included by adding detector hits of generated proton-proton interactions on top of the hits resulting from the main interaction. Most of the simulated event samples used in this thesis are processed using this detector simulation. However, the interaction of new particles that can arise from specific theory models is not always readily described in GEANT. This is the case for the signal samples used in the analysis described in Chapter 6, so an additional step was needed in order to simulate strongly interacting massive particles (SIMPs) in the CMS detector, described in Section 4.4.

4.3 Event reconstruction

Once the detector response has been simulated, the obtained events can be reconstructed. The same method is applied for these simulated events and for data coming from the detector. First, the reconstruction of tracks is performed, with a specific track reconstruction for electrons and muons. Furthermore, the calorimeter deposits, generated by electrons, photons, and hadrons, are grouped into clusters. Additionally, the reconstruction is further improved by using the so-called particle flow (PF) algorithm described in Section 4.3.6. This algorithm greatly improves the performance for jet and hadronic τ decay reconstruction, missing transverse momentum determination, as well as electron and muon identification. Finally, the obtained particle flow (PF) candidates are clustered into jets, and the missing transverse energy can be derived.

4.3.1 Track and vertex reconstruction

The tracks of charged particles going through the CMS tracker are reconstructed with an iterative tracking approach. This is used to cope with the high occupancy of hits and consequently high combinatorics. Additionally, the first iterations search for tracks with less possible combinations,

such as tracks with many pixel hits or a high momentum. After every iteration, the hits associated with the found track are removed to reduce the combinatorics. Each iteration consists of four steps:

1. **Seed generation.** In this first step hits are combined into seeds for the subsequent track finding. In the initial iterations pixel triplets are used, then pixel pairs together with a constraint on the origin of the trajectory based on the assumption that it originated near the beam spot, in order to take gaps or non-working modules into account. Next, mixed pixel/strip triplets are taken, and finally strip-only seeds are used. These additional iterations improve the acceptance in p_T and in displacement with respect to the primary vertex.
2. **Track finding.** The seeds are used as starting point for a Kalman filter algorithm. This method extrapolates the seed trajectory outward to the next layer, taking into account the presence of the magnetic field, potential energy loss and multiple scattering. If compatible hits are found in the next layer, the parameters of the trajectory are updated. This process continues until the outermost layer of the tracking system. Using this method, a given seed can generate multiple tracks, or different tracks can share hits. A trajectory cleaner therefore determines the fraction of hits the tracks have in common and discards the track with the lowest number of hits when there are too many shared hits. If both tracks have the same number of hits, the track with the largest χ^2 value is removed.
3. **Track fitting.** The track parameters are then refitted using a Kalman filter and smoother, taking all hits determined in the track finding step into account. This is done in order to find the optimal track parameters.
4. **Track selection.** Finally, the tracks are selected based on quality requirements, such as the number of layers that have hits, the χ^2/dof , and the distance to a primary vertex. This greatly reduces the fraction of reconstructed tracks that are fake.

The performance of the track reconstruction is excellent, and a high track-finding efficiency is obtained [140] while keeping the rate of fake tracks negligible. The highest tracking efficiency is obtained for muons, which traverse the full detector volume and have an improved momentum resolution at high p_T due to tracking information from the muon detectors giving a long lever arm. For isolated muons with p_T between 1 and 100 GeV the tracking efficiency is higher than 99% for the entire η coverage of the tracker, as can be seen from the left plot in Figure 4.4. The p_T resolution is about 2-3% for a muon with $p_T = 100$ GeV up to $|\eta| < 1.6$, but worsens for higher pseudorapidities. Different types of particles interact differently with the detector material. Charged hadrons, for example, are also subject to elastic and inelastic nuclear interactions and have a tracking efficiency of 80-95% depending on pseudorapidity and transverse momentum, as shown in the right plot of Figure 4.4.

Finally, the primary vertices are reconstructed from the tracks. Since the collisions happen between bunches of protons, at the luminosities reached at the LHC multiple protons will be colliding at the same time. The particles generated in these pileup interactions are all detected simultaneously and form a challenge to disentangle them from the particles coming from the to be studied interaction.

The reconstruction is performed as detailed in Section 9.4.1 of [141], by first clustering the tracks based on their z coordinate at the point of closest approach to the beam line. The vertex position is then estimated using an adaptive vertex fit [142] with as input the collection of tracks that is expected to come from the same interaction. Next, the tracks originating from the same vertex are clustered into jets with the anti- k_T algorithm described in Section 4.3.7 using a distance parameter of 0.4.

The vertex with the highest $\sum p_T^2$ is chosen as primary vertex, where the sum runs over these reconstructed jets, as well as the remaining tracks associated to the vertex and the missing transverse momentum at this vertex, in order to take into account neutral particles. While in events with jets many tens of high-momentum tracks can usually be associated to a primary

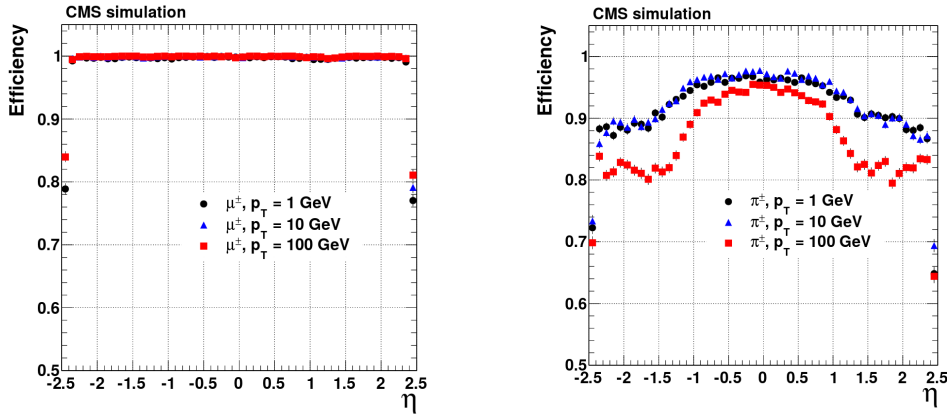


Figure 4.4: The muon efficiency (left) and pion efficiency (right) as a function of pseudorapidity, for multiple transverse momenta. Figures taken from [140]

1452 vertex, thus making primary vertex finding almost fully efficient and pure, in the case of a pair
 1453 of neutral jets, produced for example by SIMPs, this is not the case any more. The underlying
 1454 event and potentially initial state QCD radiation can still provide some tracks, but in extreme
 1455 cases a wrong vertex is chosen, arising from a hard pileup collision.

1456 4.3.2 Electron and isolated photon reconstruction

1457 Electrons are reconstructed using information from both the tracker and the calorimeters. Due to
 1458 the large amount of material present in the tracker, electrons will emit bremsstrahlung photons,
 1459 and photons will often convert into e^+e^- pairs, which can again radiate bremsstrahlung photons.

1460 For electrons, a Gaussian-sum filter (GSF) [143] candidate is taken as starting point. This
 1461 GSF candidate is obtained using 2 different methods to reconstruct the electron track from the
 1462 hits in the tracker, which should gather all radiated energy from the electron. First, the ECAL-
 1463 based approach is used, grouping ECAL clusters into superclusters. These superclusters collect
 1464 the energy of the electron and the bremsstrahlung photons in a small η window and a large
 1465 ϕ window, taking the bending of the electron track in the magnetic field into account. The
 1466 supercluster energy and position is then used to estimate the position of the corresponding hits
 1467 in the tracker layers. Subsequently, the tracker-based approach is used to find electrons missed
 1468 by the ECAL-based method. In this case, the tracks from the iterative tracking with transverse
 1469 momentum larger than 2 GeV are used. Additional requirements are placed on the number of
 1470 hits and the χ^2 of the fit, and the specific electron tracking is performed, using a GSF fit, which
 1471 is more adapted to electrons than the Kalman filter used in the iterative tracking, as it describes
 1472 the energy loss in each tracker layer. The electron seeds obtained with both methods are merged
 1473 and used as input for the full electron tracking. The obtained electron tracks are then linked
 1474 to ECAL clusters by the PF algorithm, as described in Section 4.3.6. In the case of isolated
 1475 photons, a candidate is seeded from an ECAL supercluster with transverse energy larger than
 1476 10 GeV which is not linked to a GSF track.

1477 The total energy of the accumulated ECAL clusters is corrected for the energy that was lost
 1478 in the process of reconstruction, using analytical functions of the energy and pseudorapidity. The
 1479 applied corrections can be as large as 25%, at low transverse momentum and at $|\eta| = 1.5$, where
 1480 the material density in the tracker is largest. The energy of the electron is then obtained from a
 1481 combination of the corrected energy and the momentum of the GSF track, while the direction of
 1482 the electron is taken from the GSF track. For photons, the corrected energy and the direction of
 1483 the supercluster are used.

4.3.3 Electron and photon identification

In general, the electron and photon candidates must satisfy identification criteria to be retained. In the case of electrons two methods for identification are available: a cut-based identification or a multivariate boosted decision tree (BDT) combining fourteen variables including the amount of energy radiated and the ratio between the energies gathered in HCAL and ECAL. In the monojet analysis described in Chapter 5, the former is used. In this method, four different working points are defined, denoted as “tight”, “medium”, “loose”, and “veto”, with varying signal efficiency and background rejection. For the electron veto the loose selection is used, while a tight identification is required on one electron to select the events in the dielectron and single electron control regions.

variable	loose		tight	
	barrel	endcaps	barrel	endcaps
full 5x5 $\sigma_{i\eta i\eta}$	< 0.0114	< 0.0352	< 0.0101	< 0.0279
$ \Delta\eta_{in} $	< 0.0152	< 0.0113	< 0.00926	< 0.00724
$ \Delta\phi_{in} $	< 0.216	< 0.237	< 0.0336	< 0.0918
H/E	< 0.181	< 0.116	< 0.0597	< 0.0615
relative isolation	< 0.126	< 0.144	< 0.0354	< 0.0646
$ 1/E - 1/p [\text{GeV}^{-1}]$	< 0.207	< 0.174	< 0.012	< 0.00999
$ d_{xy}(\text{vtx}) [\text{cm}]$	< 0.0564	< 0.222	< 0.0111	< 0.0351
$ d_z(\text{vtx}) [\text{cm}]$	< 0.472	< 0.921	< 0.0466	< 0.417
expected inner missing hits	≤ 2	≤ 3	≤ 2	≤ 1
pass conversion veto	yes	yes	yes	yes

Table 4.2: Loose and tight electron identification criteria. The isolation is computed in a cone of $\Delta R < 0.3$ around the electron.

Similarly, for the photons, both a cut-based identification and a multivariate analysis can be used. Both for the monojet and the SIMP analysis, described in Chapters 5 and 6, the cut-based identification is used. Three standard working points are provided, denoted as “loose”, “medium”, and “tight”, with an average efficiency of 70%, 80%, and 90%, respectively. In both analyses, the loose identification is used for the photon veto. In the SIMP analysis, the event is only rejected when the identified photon is within a cone of $\Delta R < 0.1$ of one of the two leading jets. Additionally, the photon veto is extended to reject events containing jets with a large photon energy fraction and unidentified photons. This happens for instance when there is a photon conversion in the tracker. The event is therefore rejected when the jet photon energy fraction is larger than 0.8, the photon is not identified by the loose criteria, and a conversion is matched to the photon within $\Delta R < 0.2$ and has $p_{T,\text{conv}}/p_{T,\gamma} > 0.3$. Lastly, the two jets are also required to have a neutral electromagnetic energy fraction lower than 0.9, corresponding to one of the standard tight jet identification requirements mentioned in Section 4.3.7. Finally, the monojet analysis uses a photon + jets control region as well. These events are selected by applying the tight photon identification.

4.3.4 Muon reconstruction

Muon tracking is performed using 2 complementary approaches. The first method starts from standalone muons, which are reconstructed from hits in the muon detectors only using pattern recognition. The standalone muons are then matched to tracks in the tracker, and the hits are combined to form a global muon track. This global muon fit improves the momentum resolution compared to the tracker-only fit at muon momenta larger than 200 GeV.

For momenta below 10 GeV, muons often fail the global muon conditions which require the muon to penetrate through more than one muon detector plane, due to the large multiple

variable	loose		tight
	barrel	endcaps	barrel
full 5x5 $\sigma_{inj\eta}$	< 0.0102	< 0.0274	< 0.0102
H/E	< 0.05	< 0.05	< 0.05
charged hadron isolation	< 3.32	< 1.97	< 1.37
neutral hadron isolation	$< 1.92 + 0.014 \times p_T$ $+ 1.9 \times 10^{-5} \times p_T^2$	$< 11.86 + 0.0139 \times p_T$ $+ 2.5 \times 10^{-5} \times p_T^2$	$< 1.06 + 0.014 \times p_T$ $+ 1.9 \times 10^{-5} \times p_T^2$
photon isolation conversion safe	$< 0.81 + 0.0053 \times p_T$	$< 0.83 + 0.0034 \times p_T$	$< 0.28 + 0.0053 \times p_T$
electron veto	yes	yes	yes

Table 4.3: Loose and tight photon identification criteria. The isolation is computed in a cone of $\Delta R < 0.3$ around the photon.

scattering in the return yoke. In this case, tracker-only muon reconstruction is more efficient since it only requires one muon segment. Each track in the tracker with a transverse momentum larger than 0.5 GeV and a total momentum larger than 2.5 GeV is therefore extrapolated to the muon system and if at least one matching track segment is found, it is retained as muon candidate.

Within the geometrical acceptance of the muon system about 99% of the muons are reconstructed, either as global muon or as tracker muon and frequently as both. Global and tracker muons that share the same track inside the tracker are merged into a single candidate. Muons that are only reconstructed as standalone muons have a worse momentum resolution compared to the global and tracker muons. These standalone muons are however only considered in the further reconstruction when the fit is of high quality and is associated with a large number of hits in the muon system.

Charged hadrons can be misreconstructed as muons if e.g. a part of the hadron shower reaches the muon system. In order to improve the muon identification, the PF muon identification algorithm described in Section 4.3.6 also matches energy deposits in the ECAL and HCAL with the muon track.

4.3.5 Muon identification

When using muons for physics analysis, some identification criteria are generally applied in order to ensure the quality of the muons. There are several standard levels of identification, denoted as “tight”, “medium”, and “loose”, which provide a trade-off between muon identification efficiency and misidentification. In general, the tight and loose identification are the most widely used identification criteria.

The loose identification only requires the muons to be either global or tracker-only muons, and to be identified by the PF algorithm as a muon. As a result, it is highly efficient for both prompt muons and muons from quark decays. In analyses with prompt muons, this identification is therefore often complemented by an impact parameter cut, associating the muon to the primary vertex.

For the tight identification, the muon is required to be a global muon and to be identified by the PF algorithm as a muon. The normalized χ^2 of the global muon track fit should be smaller than 10 to suppress hadronic punch through and muons from hadron decays in flight. To further suppress these contributions at least one muon chamber hit should be included in the global muon track fit and muon segments should be found in at least two muon stations. Cosmic muons and tracks from pileup are suppressed by requiring the tracker track to have $|d_{xy}| < 2$ mm and $|d_z| < 5$ mm, with d_{xy} the traverse impact parameter and d_z the longitudinal distance with respect to the primary vertex. Finally, at least one pixel hit is required, as well as hits in at least 5 tracker layers, in order to ensure a good p_T measurement.

1553 In the case of the monojet analysis described in Chapter 5, the loose muon identification is
 1554 used to select muons for the muon veto. An additional isolation cut of 0.2 is applied in order to
 1555 reject muons inside jets. The isolation value is computed as the sum of the transverse momenta
 1556 of all charged hadrons associated to the primary vertex, neutral hadrons, and photons in a cone
 1557 of $\Delta R < 0.4$ around the muon, relative to the p_T of the muon. The tight muon identification is
 1558 used as well, to select events in the dimuon and single muon control regions.

1559 4.3.6 Particle flow

1560 The particle flow (PF) algorithm [144] reconstructs so-called particle flow candidates by com-
 1561 bining information from all different CMS subdetectors, linking different elements, such as
 1562 tracks in the tracker, calorimeter clusters, and muon tracks. A global picture of the event is thus
 1563 formed, where each particle is uniquely identified. The obtained collection of particle candidates
 1564 is subsequently used to reconstruct jets and tau leptons, and to determine the missing transverse
 1565 momentum.

1566 In a first step, the PF algorithm identifies charged particle tracks, as defined in Section 4.3.1
 1567 for all tracks, and in Sections 4.3.2 and 4.3.4 for electron and muon tracks in particular. At
 1568 the same time, the calorimeter clusters are reconstructed with a clustering algorithm designed
 1569 specifically for the PF event reconstruction. In this algorithm, cluster seeds are first identified as
 1570 local energy maxima with respect to the four or eight closest cells, if the energy deposited in the
 1571 cell is above a given seed threshold. The clusters are then formed by accumulating neighbouring
 1572 cells with an energy above a given cell threshold, suppressing noise.

1573 The PF elements in the different subdetectors are then connected by a link algorithm which
 1574 avoids any double counting. The link algorithm produces blocks of associated elements, quan-
 1575 tifying the quality of the link by defining a geometrical distance between the elements. When
 1576 an element is linked to multiple other elements, only the link with the shortest distance is kept.
 1577 More precisely, a link between a track in the tracker and a calorimeter cluster is made by extrap-
 1578 olating it from the last hit in the tracker to the calorimeters. The distance between the position
 1579 of the extrapolated track and the cluster in the (η, ϕ) plane is then used to define the link dis-
 1580 tance. At the interaction points between the track and the tracker layers, tangents to the GSF
 1581 tracks are extrapolated to the ECAL in order to collect the energy of photons radiated by electron
 1582 bremsstrahlung. A dedicated conversion finder was also developed to identify bremsstrahlung
 1583 and prompt photon conversions into e^+e^- pairs. Links between calorimeter clusters are estab-
 1584 lished outside of the tracker acceptance, or between the preshower and ECAL clusters in the
 1585 preshower acceptance. In this case the link distance is also defined as the distance between the
 1586 position of the clusters. Charged particle tracks can also be linked by a common secondary ver-
 1587 tex. Finally, the PF muon identification algorithm associates the muon tracks to the muon energy
 1588 deposits in the ECAL and HCAL, to improve the muon identification performance.

1589 In a next step, the PF blocks obtained by linking the multiple PF elements, are classified
 1590 as muons, electrons, or isolated photons. The corresponding elements are then excluded from
 1591 further consideration. Once electrons, muons, and isolated photons have been identified, the
 1592 remaining elements are identified as charged hadrons, neutral hadrons, or photons produced in
 1593 jets. Within the tracker acceptance, the ECAL clusters not linked to any track are classified as
 1594 photons, while the clusters in the HCAL without a matched track are labelled as neutral hadrons.
 1595 Outside of the tracker acceptance, charged and neutral hadrons can not be distinguished. ECAL
 1596 clusters linked to an HCAL cluster are then assumed to arise from the same hadron shower, and
 1597 the estimated energy for these particles is the sum of the energy deposited in the ECAL and the
 1598 HCAL. The ECAL clusters that are not linked to an HCAL cluster are classified as photons.

1599 4.3.7 Jet reconstruction

1600 Jets are reconstructed with the anti- k_T algorithm [145], which clusters either the generated par-
 1601 ticles from event simulation, or the particles reconstructed by the PF algorithm (PF jets), or the

1602 energy deposits in the calorimeters (Calo jets). This procedure takes into account the transverse
 1603 momentum p_T , also called k_T , of the particles and the distance between particles, defined as

$$\Delta R_{ij} = \sqrt{(\eta_i - \eta_j)^2 + (\phi_i - \phi_j)^2}. \quad (4.1)$$

1604 The strategy consists of the following steps:

1605 1. For every pair of particles i and j , a distance d_{ij} defined as

$$d_{ij} = \min \left(\frac{1}{p_{Ti}^2}, \frac{1}{p_{Tj}^2} \right) \frac{\Delta R_{ij}^2}{R^2} \quad (4.2)$$

1606 is calculated.

1607 2. For every particle i , a distance d_{iB} to the beam pipe is calculated with

$$d_{iB} = 1/p_{Ti}^2. \quad (4.3)$$

1608 3. The minimum of d_{ij} and d_{iB} is then determined.

1609 4. If it is d_{ij} , particles i and j are recombined into a new particle by adding the four-momenta
 1610 of the particles. If it is d_{iB} , particle i is declared to be a jet and it is removed from the list
 1611 of particles.

1612 5. This is repeated until no particles remain.

1613 In this clustering algorithm, the parameter R determines what is called a jet. If a particle
 1614 i has no other particles within a distance R , d_{iB} will be smaller than d_{ij} and the particle will
 1615 become a jet. A consequence of this is that an arbitrarily soft particle can become a jet, and
 1616 therefore a minimum transverse momentum for a jet to be of interest is defined.

1617 The anti- k_T algorithm favours clustering around hard particles, and the jets then grow out-
 1618 ward from this seed. This gives rise to circular jets, with a cone size that is proportional to
 1619 R . Since it still involves a combination of energy and angle in the distance measure, this is a
 1620 collinear-safe growth, meaning that the jet will not change when one of the particles of the jet is
 1621 split collinearly. This algorithm is also infrared-safe, i.e. the same set of jets is obtained when
 1622 soft particles are emitted.

1623 A reliable determination of the jet energy is not straightforward, since many effects can
 1624 distort the energy estimation, such as the calorimeter response, the limited particle reconstruction
 1625 efficiency, the underlying event, the pileup, and the charged particles bending out of the jet
 1626 cone due to the strong magnetic field. The pileup is mitigated by applying charged hadron
 1627 subtraction (CHS), which consists of removing charged hadrons associated with vertices other
 1628 than the primary vertex from the list of PF candidates. Additionally, the jet energy is corrected
 1629 using a factorised approach, as illustrated in Figure 4.5, with the following steps:

- 1630 • **Pileup correction (L1).** The first level of jet energy corrections is applied event-by-event
 1631 and jet-by-jet, and is determined from simulation. It is dependent on the pseudorapidity
 1632 and transverse momentum of the jet, the average p_T density in the event, and the effective
 1633 jet area. This effective area is determined by injecting a large number of very soft particles
 1634 in the event before the jet clustering. The spread of the soft particles in each jet then
 1635 defines the jet area. When these corrections are applied on data, residual corrections are
 1636 also applied to take into account the difference between the simulated events and the data.

- 1637 • **Relative η and absolute p_T corrections (L2L3).** These corrections are also obtained
 1638 from simulations and correct for the non-uniform response of the calorimeters in η and
 1639 p_T . They are determined by comparing the reconstructed p_T to the one obtained from the
 1640 jets built from the generated particles. These corrections have the largest impact on the jet
 1641 energy.

- 1642 • **Residual η and p_T corrections (L2L3Residual).** Since the L2L3 correction is derived
 1643 from simulation, additional residual corrections are needed in order to correct for the
 1644 remaining small differences between the jet response in data and simulation. These cor-
 1645 rections are typically of the order of a few percent.

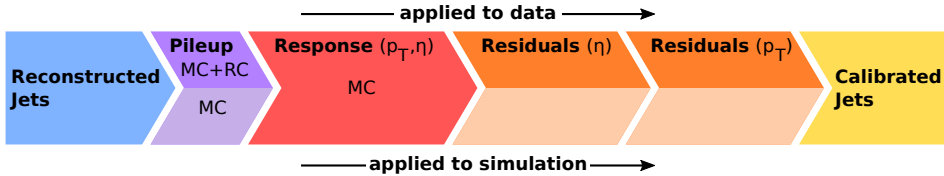


Figure 4.5: Graphical overview of the factorised approach used at CMS to apply jet energy corrections.

1646 Optionally, a set of identification criteria are applied on the PF jets. A jet is required to
 1647 consist of at least two particles. For jets in the region $|\eta| < 2.7$, the fraction of energy coming
 1648 from ether neutral hadrons or photons should not exceed 99%. Additionally, for jets restricted to
 1649 the tracker acceptance ($|\eta| < 2.4$), there should at least be some energy deposited in the HCAL,
 1650 the jet should contain 1 or more charged constituent, and the fraction of energy corresponding
 1651 to electrons or photons should not exceed 99%.

1652 Moreover, jets from pileup can be identified as well. This pileup jet identification relies
 1653 on the topology of the jet shape which is used to disentangle jets coming from the overlap
 1654 of multiple interaction and real hard jets, the object multiplicity, and the compatibility of the
 1655 tracks in the jets with the primary vertex. This last property of pileup jets can evidently only be
 1656 exploited for jets within the tracker acceptance.

1657 Both jet and pileup jet identification are used in the monojet analysis described in Chapter 5.
 1658 In the trackless jets analysis described in Chapter 6 however, the full jet ID is not applied, since
 1659 the requirements on e.g. the neutral hadronic energy fraction and the charged multiplicity would
 1660 reject the signal events. Instead, only the requirement on the jet neutral electromagnetic energy
 1661 fraction is applied, in order to reject photons.

1662 4.3.8 Identification of b-jets

1663 For the identification of jets originating from b quarks, the long lifetime of the B hadrons arising
 1664 from the hadronisation of b quarks is exploited. The B hadrons will therefore decay at a
 1665 position that is displaced with respect to the primary interaction vertex. The b -jets can then be
 1666 identified by looking for the presence of displaced tracks from which a secondary vertex may
 1667 be reconstructed. Additionally, the B hadrons have a probability of 20% to decay into muons
 1668 or electrons. Consequently, the presence of these charged leptons can be used as well for b -jet
 1669 identification techniques.

1670 Within the CMS collaboration, two different algorithms are being used during Run 2, namely
 1671 the Jet Probability and the Combined Secondary Vertex taggers [146]. In this thesis, the latter is
 1672 used to identify b -jets, combining the information from displaced tracks and secondary vertices
 1673 in a multivariate technique. Jets are then identified or “tagged” as b -jets by applying a cut
 1674 on the discriminator output. Three standard operating points are defined, denoted as “loose”,
 1675 “medium”, and “tight”, corresponding to a misidentification probability of 10%, 1%, and 0.1%
 1676 for light jets with $p_T > 30$ GeV, respectively. In the monojet analysis described in Chapter 5,
 1677 the loose working point is used to veto b -jets.

1678 4.3.9 Reconstruction of tau leptons

1679 Tau leptons can decay into either a charged lepton and two neutrinos, or a few hadrons and one
 1680 neutrino. The hadronic decays of the tau lepton can be separated from quark or gluon jets by

1681 analysing the decay products. With the PF algorithm, it is possible to resolve the particles originating
 1682 from the tau decay and to determine its isolation. Hadronic tau decays are reconstructed
 1683 using the hadrons-plus-strips (HPS) algorithm [147] by using those particles as input. The jet
 1684 constituent particles are combined into candidates compatible with one of the main hadronic
 1685 tau decay modes, $\tau^- \rightarrow h^-\nu_\tau$, $\tau^- \rightarrow h^-\pi^0\nu_\tau$, $\tau^- \rightarrow h^-\pi^0\pi^0\nu_\tau$, and $\tau^- \rightarrow h^-h^+h^-\nu_\tau$,
 1686 where h represents a charged hadron. This PF reconstruction of the tau decay products has
 1687 significantly improved the reconstruction and identification of the tau leptons compared to the
 1688 previous method which only took the energy deposits in the calorimeters into account.

1689 **4.3.10 Missing transverse momentum reconstruction**

1690 While most particles produced in the collisions can be reconstructed from the hits and energy
 1691 deposits in the detector, some collision products might not leave energy deposits in tracker,
 1692 calorimeters or muon system. This makes an accurate reconstruction of this type of particles
 1693 impossible, and an alternative method is used, based on indirect observations. As the detector
 1694 is hermetically closed such that all other particles in the event can be detected, the missing
 1695 transverse momentum can be determined. This momentum then corresponds to all undetected
 1696 particles in the event, and can be calculated from the vectorial sum of the transverse momenta
 1697 of all the observed final state particles:

$$\vec{E}_T^{miss} = - \sum \vec{p}_T, \quad (4.4)$$

1698 where the sum runs over all reconstructed PF particles. The variable that is generally used in
 1699 particle physics analyses is the norm of the missing transverse momentum:

$$E_T^{miss} = |\vec{E}_T^{miss}|. \quad (4.5)$$

1700 A notable example of particles leaving no hits or energy deposits behind are neutrinos, as
 1701 they are neutral and weakly interacting and will therefore traverse the entire detector unhindered.
 1702 Other hypothetical neutral weakly interacting particles, which are being searched for in many
 1703 physics analyses, would escape the detector without producing hits as well.

1704 **4.4 Simulation and reconstruction of the SIMP signal**

1705 The SIMP events generated as described in Section 4.1.2 are then simulated in the CMS detector
 1706 using GEANT. However, the SIMPs are not included in the simulation, as these new particles
 1707 are unknown in GEANT and their interaction with matter has not been implemented yet. In
 1708 order to simulate the new dark matter candidates in the CMS detector two new approaches were
 1709 implemented.

1710 In the first approach, the SIMPs were incorporated by adding an additional step to the standard
 1711 reconstruction described in Section 4.3. In this additional step the SIMPs are directly
 1712 converted to neutral PF candidates and merged with the rest of the PF candidates. Additionally,
 1713 the new PF candidates are smeared with jet energy resolution (JER) distributions obtained from
 1714 a sample produced using neutrons instead of SIMPs. Neutrons were chosen because of their
 1715 resemblance to the SIMPs as single neutral particles generating a hadronic shower.

1716 In order to produce this neutron sample used to derive the JER, the same additional custom
 1717 step is applied, but in this case the neutrons will also be correctly reconstructed by the standard
 1718 reconstruction. As a result, the neutrons will be present in the standard reconstruction and will
 1719 be added a second time converting them into neutral PF candidates. The standard reconstructed
 1720 PF candidates that are matched to the generated neutrons are therefore removed before injecting
 1721 the converted generated neutrons to the collection of PF candidates. The JER distributions are
 1722 then derived by comparing the resulting uncorrected PF jets with the corresponding neutrons
 1723 in sample produced with the standard reconstruction using the full GEANT simulation. The

resolution is computed in bins of η and p_T , and an example is shown in Figure 4.6 for central neutrons with low and high transverse momentum.

After applying this smearing, the jets are processed with the standard sequence of CHS, jet clustering, L1FastJet, and L2/L3 corrections described in Section 4.3.7.

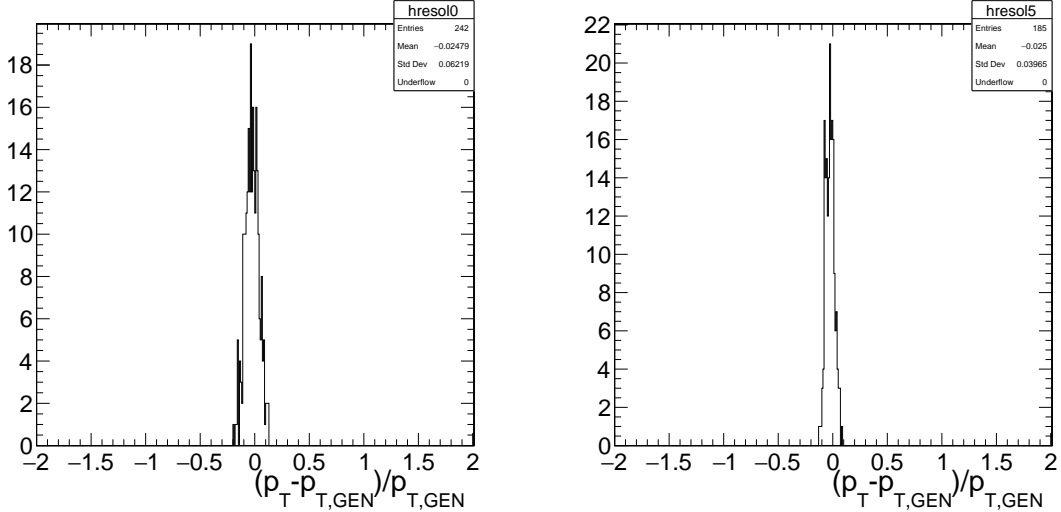


Figure 4.6: The jet energy resolution of neutrons with $0 < |\eta| < 0.5$ and $200 \text{ GeV} < p_T < 300 \text{ GeV}$ (left) or $700 \text{ GeV} < p_T < 800 \text{ GeV}$ (right).

In order to validate this method, the custom and standard neutron samples are used to compare the two leading generator-level jets to the new jets from the custom sample, denoted as P2PF jets, and the PF jets from the standard sample. This is illustrated in Figure 4.7, where the p_T of the generated neutrons is shown on the horizontal axis, and the p_T of the reconstructed jet is shown on the vertical axis. The left plot shows the standard neutron sample produced with the full GEANT simulation, while the right plot shows the custom neutron sample where the neutron was directly converted into a neutral PF candidate. The JER distributions are also compared in Figure 4.8 and fitted with a Crystal Ball function, showing compatible parameters.

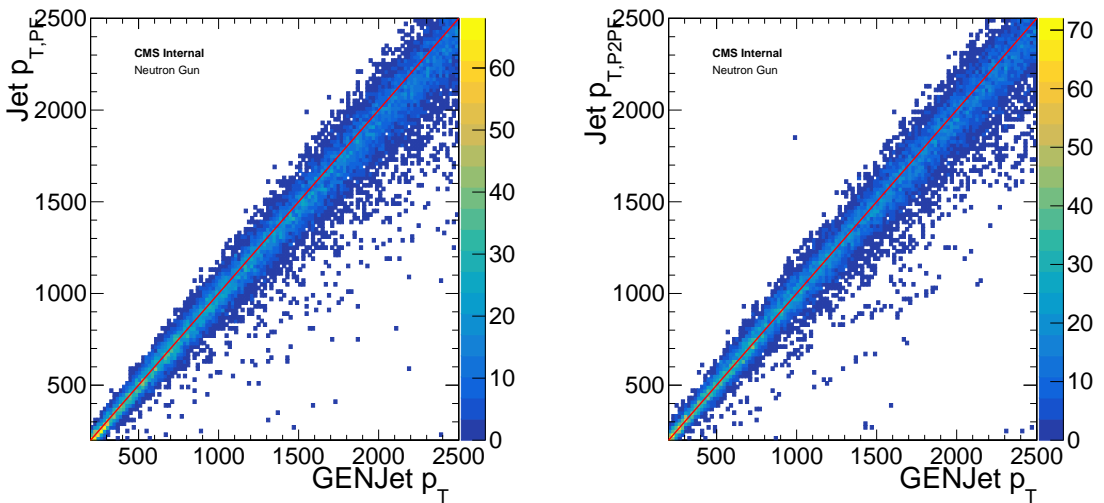


Figure 4.7: Comparison of the transverse momentum of the generator-level jets to the PF jets (left) and P2PF jets (right) in the region $0 < |\eta| < 0.5$ with jet energy resolution smearing, using a neutron sample.

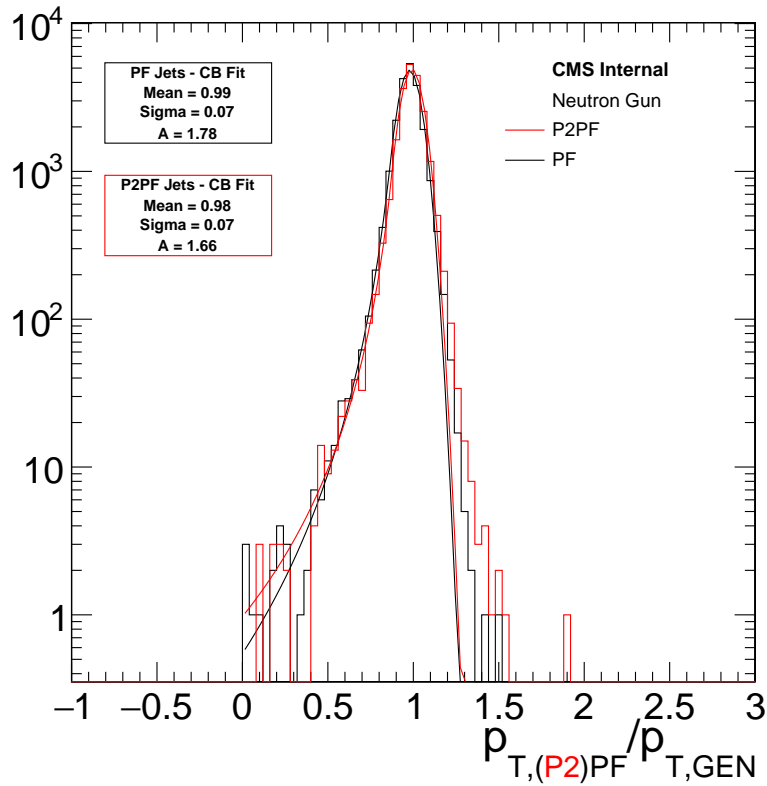


Figure 4.8: The jet energy resolution of the corrected P2PF jets (red) and PF jets (black), fitted with a Crystal Ball function.

This demonstrates that the procedure, where the JER distributions derived from a neutron sample are used to smear the PF candidates from generator-level SIMPs, can sufficiently accurately simulate SIMPs in a realistic detector, assuming SIMPs are neutron-like. However, since this procedure directly converts the generated SIMPs into PF candidates, the SIMPs do not interact in the Tracker and the resulting jets have a very steeply falling charged hadron energy fraction (CHF) distribution. This gives an optimistic image, which translates in a maximal signal efficiency.

The SIMP signal simulation and reconstruction was therefore further improved by moving to the second approach. In this method, the generated SIMP particles are not converted into neutral PF candidates, but they are instead replaced by neutrons, keeping the SIMP kinematics. The standard reconstruction and full GEANT simulation can then be applied, since the neutrons are correctly recognized and simulated. In this case, interactions will happen inside the Tracker as well and the resulting jets will contain a larger CHF, as is shown in Figure 4.9. Eventually, this second method will be used in the trackless jets analysis described in Chapter 6.

This method gives a good approximation of a SIMP signal, since the shower generated by the SIMP is in principle contained inside the calorimeters, as the model described in Section 2.3 is constructed so that for a specific choice of couplings the SIMPs may be detected as regular hadrons. Although the considered SIMP-nucleon interaction is repulsive, this does not differ considerably from known attractive interactions at the probed high energies. The incoming SIMP hits a nucleon at rest in the calorimeter, breaking it up, and because of the large incoming momentum, there is a boost forward into the calorimeter and the shower starts. The cross section would therefore be identical for a repulsive or attractive interaction and the effect on the shower is negligible since the scattering angle is very small due to the momentum boost. Furthermore, the higher the momentum of the SIMP, the shorter the distance it travels to deposit its characteristic momentum. With the considered couplings, the depth containing a SIMP with 500 GeV

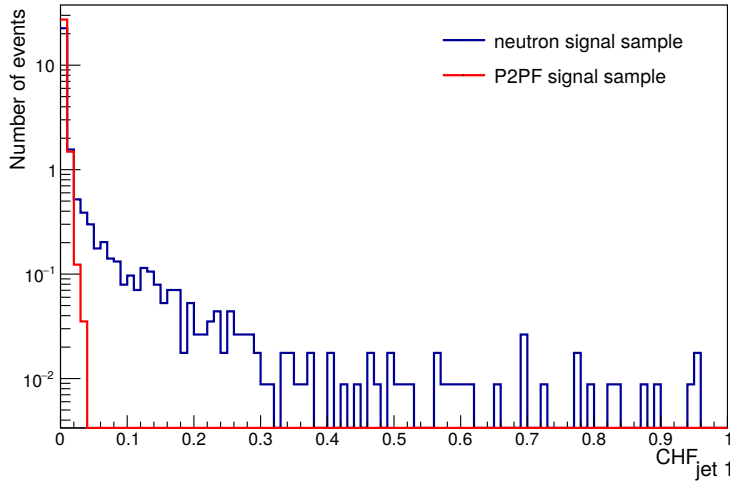


Figure 4.9: CHF distribution of the leading jet, for a signal sample produced with the first approach (red) and the corresponding sample produced using the second method (blue).

1761 momentum is below 1 m, within the calorimeter [148]. Most of the energy will therefore be
 1762 deposited in the first interaction with the material. Given the expected forward energy flow in
 1763 the calorimeter shower, and the shower containment achieved by the choice of couplings in the
 1764 simplified model, the shower induced by the SIMP interaction can to first order be modelled by
 1765 the interaction of a high-momentum neutral hadron, like a neutron.

5

1766

1767

The Monojet Analysis

1768 As has been described in Chapter 2, there are many searches for dark matter both at particle
1769 accelerators and elsewhere. At the LHC, one very promising channel is the so-called monojet
1770 search, where the detection of dark matter is done by looking for missing momentum in associa-
1771 tion with one or more jets. The dark matter particles are expected to pass through the detector
1772 without leaving any signal since they are neutral and only interact very weakly. They can how-
1773 ever be detected indirectly as missing momentum when they recoil off one or more jets coming
1774 from initial state radiation. While the Run 2 analysis is described here, this analysis was already
1775 performed using the data collected during Run 1 [149] as well.

1776 First, the used physics objects are described in Section 5.1. Next, the selection of the events
1777 using the trigger is described in Section 5.2, and the subsequent event selection performed with
1778 fully reconstructed events is detailed in Section 5.3. The estimation of the background and the
1779 included systematic uncertainties are described Section 5.4 and 5.5, respectively. In Section 5.6,
1780 the obtained results are shown. The improvements achieved by going from the analysis strategy
1781 used in 2015 to the 2016 version are detailed in Section 5.7. Finally, the results are interpreted
1782 in terms of the considered dark matter models in Section 5.9.

1783 5.1 Physics object reconstruction

1784 While jets and missing transverse momentum are evidently important objects in this analysis,
1785 other physics objects are used as well. Leptons and photons are for example vetoed in order to
1786 reject backgrounds, and are used to define the many control regions used for the background
1787 prediction.

1788 5.1.1 Jets

1789 The method described in Section 4.3.7 is used to reconstruct the used PF jets, and the jet energy
1790 corrections are applied as well. Furthermore, the jets are required to have $p_T > 30 \text{ GeV}$, and to
1791 pass the loose jet identification and pileup jet identification described in Section 4.3.7. Addition-
1792 ally, a jet cleaning is applied by requiring a jet charged hadron energy fraction CHF > 0.1 and
1793 a jet neutral hadron energy fraction NHF < 0.8 . The b- jets are tagged as using the Combined
1794 Secondary Vertex algorithm described in Section 4.3.8, with the loose working point.

5.1.2 Missing transverse momentum and hadronic recoil

The missing transverse momentum E_T^{miss} is reconstructed as detailed in Section 4.3.10. For the control regions, the E_T^{miss} is redefined in order to imitate the E_T^{miss} shape in the signal region. This hadronic recoil U is obtained by removing the leptons or the photon present in the event from the E_T^{miss} computation.

5.1.3 Leptons

Loose identification criteria, described in Section 4.3.3, are used to veto electrons. Additionally, the electrons are required to have $p_T > 10 \text{ GeV}$ and $|\eta| < 2.5$. Similarly, muons are required to pass the loose muon identification described in Section 4.3.5 and to have $p_T > 10 \text{ GeV}$ and $|\eta| < 2.4$. In the case of tau leptons, they are required to have $p_T > 15 \text{ GeV}$ and $|\eta| < 2.3$. They should also pass the tau identification criteria, which require a jet with an identified subset of particles with a mass consistent with the decay products of a hadronic tau and which are isolated with a pileup corrected isolation cut requiring less than 5 GeV of energy deposits within a radial cone of $\Delta R < 0.3$.

The selection of electrons and muons for the control regions is however stricter: they are required to pass the tight identification.

5.1.4 Photons

Photons are required to have $p_T > 15 \text{ GeV}$, $|\eta| < 2.5$, and to pass the loose identification criteria described in Section 4.3.3, in order to be considered for the photon veto. For the photon + jets control region, photons are required to pass the tight photon identification in order to be considered.

5.2 Trigger selection

In order to select events that have the monojet signature displayed in Figure 5.1, the trigger requires either $E_T^{miss} > 90 \text{ GeV}$, where E_T^{miss} is the magnitude of the negative vectorial sum of the p_T of all particles at trigger level, or $H_T^{miss} > 90 \text{ GeV}$, where H_T^{miss} is calculated as the magnitude of the negative vectorial sum of the momenta of all jets with $p_T > 20 \text{ GeV}$. In order to avoid collecting events that contain noise signals coming from the detector, tight requirements are placed on the jets used in the H_T^{miss} computation. Jet energy corrections are already applied at the HLT-level and the jet NHF is required to be smaller than 0.9. Muons are not taken into account to compute E_T^{miss} and H_T^{miss} , so that the same trigger can be used to select the events for the muon control regions used for the background prediction.

This trigger is studied using events passing the single electron trigger with a threshold of $p_T > 23 \text{ GeV}$, and applying an extra offline selection requiring an electron with $p_T > 40 \text{ GeV}$ passing the tight identification and a jet with $p_T > 100 \text{ GeV}$ and $|\eta| < 2.5$. The trigger efficiency is computed by determining the fraction of events which additionally pass the signal triggers, as a function of the hadronic recoil. The efficiency is above 98% for events passing the analysis selection described in Section 5.3, as shown in Figure 5.2.

To select events in the electron control regions, a single electron trigger was used with a threshold at $p_T > 27 \text{ GeV}$. The efficiency of this trigger is determined as a function of p_T and η . This is done by “tagging” one electron with $p_T > 40 \text{ GeV}$ and $|\eta| < 2.1$ which passes the tight selection requirements. A second electron with $p_T > 10 \text{ GeV}$ and $|\eta| < 2.5$ is then selected, while the invariant mass of this pair is required to be between 60 and 120 GeV, to correspond to the Z boson mass. This tag-and-probe method ensures that backgrounds are removed and allows to measure the efficiency by simply taking the fraction of probes that passes the single electron trigger. The obtained trigger efficiency turn-on curves as a function of the electron

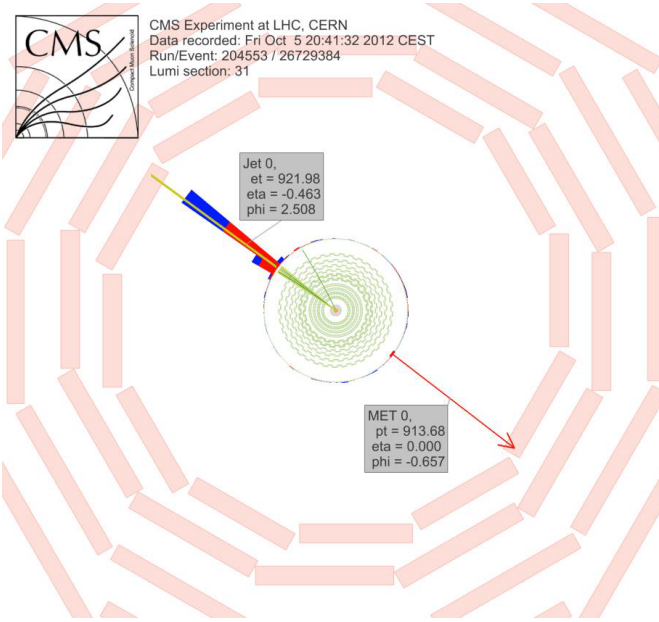


Figure 5.1: Event display showing the monojet final state.

1840 transverse momentum are shown in Figure 5.3 for two η bins, covering the ECAL barrel and
 1841 endcaps separately and leaving out the poorly instrumented region in between.

1842 Finally, the events in the photon control region are selected with a single photon trigger
 1843 requiring an isolated photon with $p_T > 175$ GeV. The performance of this trigger is measured
 1844 in data selected using a single photon trigger with a lower p_T threshold, and the turn-on is shown
 1845 in Figure 5.4.

1846 5.3 Event selection

1847 Once the events have been fully reconstructed and the jets in the event have been corrected as
 1848 described in Section 4.3.7, an event selection is applied in order to efficiently select signal events
 1849 and reduce the contribution from backgrounds, such as the production of a leptonically decaying
 1850 W boson in association with jets, semileptonic diboson decays, QCD multijets, and top quark
 1851 production. The background contribution coming from events with a Z boson produced together
 1852 with a number of jets, where the Z boson decays to two neutrinos, is irreducible as it produces
 1853 exactly the same signature as the expected signal. The missing transverse momentum E_T^{miss} is
 1854 required to be larger than 200 GeV in order to be safely above the trigger turn-on. Additionally,
 1855 the leading jet is required to have $p_T > 100$ GeV in order to balance the missing transverse
 1856 momentum, and $|\eta| < 2.5$. A cut on the difference in azimuthal angle between the E_T^{miss} and
 1857 the first four leading jets of $\Delta\phi(jet, E_T^{miss}) > 0.5$ is also applied. This is done to suppress
 1858 the QCD background from mismeasurements of jet momentum or detector noise, which could
 1859 introduce missing transverse momentum in the event, in the same direction as the mismeasured
 1860 jet. The events are further cleaned by applying quality filters to remove events coming from
 1861 beam or instrumental backgrounds. Finally, events containing a lepton, a photon, or a b-jet are
 1862 vetoed as well. Figure 5.5 shows the E_T^{miss} distribution for data and MC, after applying the
 1863 described selection.

1864 Events containing a lepton are vetoed to suppress the electroweak backgrounds, such as
 1865 $W(l\nu) + \text{jets}$ and semileptonic diboson decays, while the photon veto is added to suppress the
 1866 $Z(\nu\nu) + \text{photon} + \text{jets}$ and $W(l\nu) + \text{photon} + \text{jets}$ background processes, and to ensure there
 1867 is no overlap with a similar dark matter search which investigates the final state consisting of
 1868 missing momentum and a photon. This rejects less than 1% of the signal. Finally, the b-jet veto

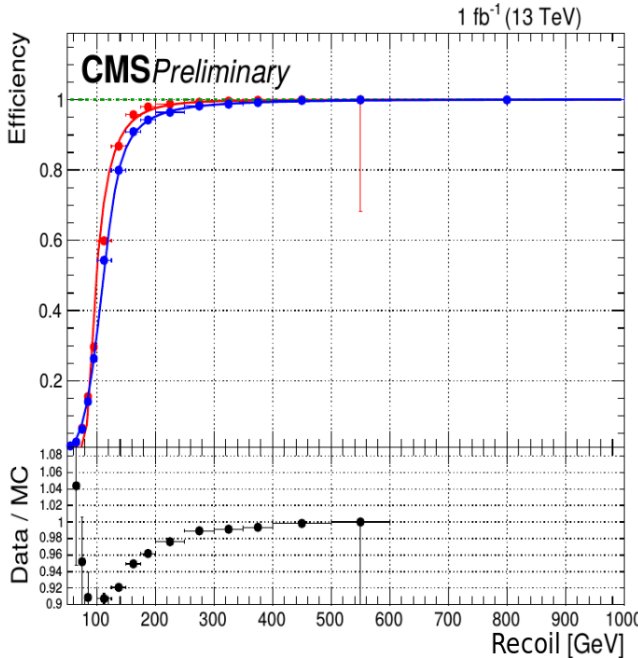


Figure 5.2: The efficiency of the used signal triggers as a function of the hadronic recoil, in MC (red) and data (blue).

1869 reduces the background from events with a single top quark or top quark pairs by a factor 3
 1870 and only reduces the signal by 5 to 10%, depending on the type and mass of the mediator. No
 1871 additional veto on the number of jets is applied.

1872 **5.4 Background estimation**

1873 The dominant background comes from events with a Z boson produced together with a number
 1874 of jets, where the Z boson decays to two neutrinos. This produces the same signature of jets with
 1875 missing momentum as the signal, and results in an irreducible background. The second largest
 1876 background consists of $W +$ jets events with a leptonically decaying W boson. This background
 1877 is already suppressed by the lepton veto, but a fraction of these events remain when the lepton
 1878 is either not identified or outside of the detector acceptance. The remaining background events
 1879 come from top quark decays, which are suppressed by the b-jet veto, semileptonic diboson
 1880 (WW , WZ , and ZZ) decays, and QCD multijet events. The two main background contribu-
 1881 tions are estimated from five control regions in data consisting of dimuon, dielectron, single
 1882 muon, single electron, and photon + jets events. The contributions from top quark decays and
 1883 semileptonic diboson decays are estimated using simulated samples, while the QCD multijet
 1884 background is estimated using a data-driven approach.

1885 **5.4.1 The Z and W background estimation**

1886 The traditional control region for the Z boson background is the dimuon control region. This
 1887 region is dominated by $Z \rightarrow \mu\mu$ events, which are very similar to the $Z(\nu\nu) +$ jets background
 1888 events, the only difference being the decay mode. The production mode and kinematics in the
 1889 control region are very similar, as well as the acceptance. However, the branching ratio of the Z
 1890 boson into two muons is 6 times smaller than the branching ratio to two neutrinos. As a result
 1891 of this, and due to the muon selection efficiency, the dimuon control region contains about 10
 1892 times less Z boson events than the signal region. In order to improve this statistical limitation,

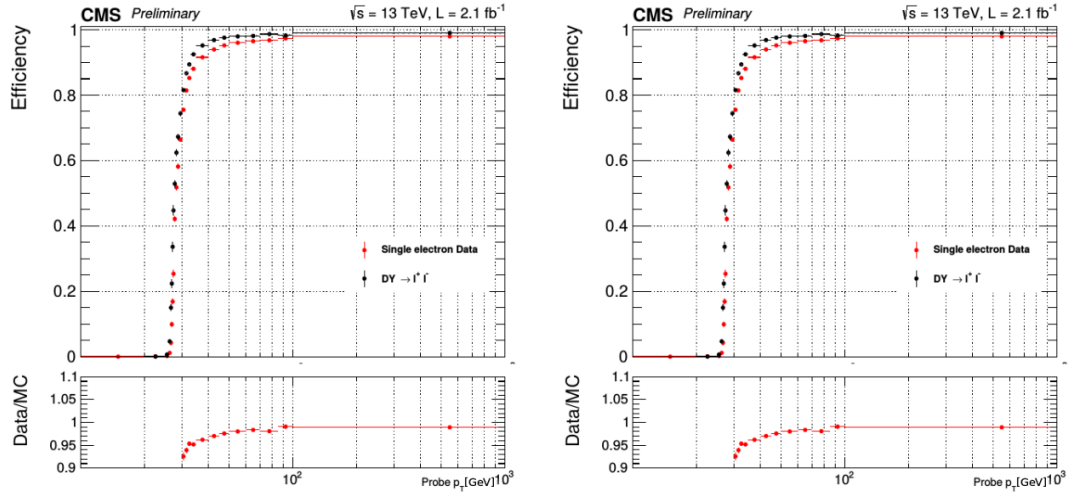


Figure 5.3: The efficiency of the single electron trigger in data (red) and MC (black) for $|\eta| < 1.4442$ (left) and $1.566 < |\eta| < 2.5$ (right).

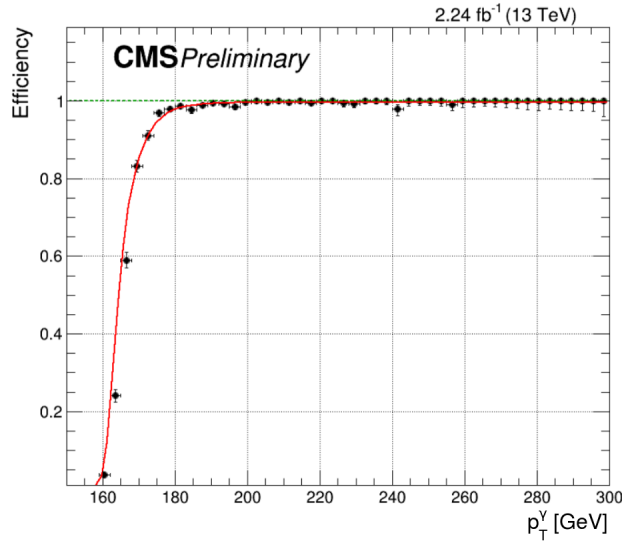


Figure 5.4: The efficiency of the single photon trigger measured in data.

1893 other control regions have been added as well.

1894 The yield of $Z(\nu\nu)$ and $W(l\nu) + \text{jets}$ events in the signal region is therefore estimated from
 1895 five control regions by using the ratio between data and MC in the control region, per bin of
 1896 the hadronic recoil distribution. As illustrated in Figure 5.6, the $W(l\nu) + \text{jets}$ background is
 1897 estimated from the single lepton control regions, and the $Z(\nu\nu) + \text{jets}$ background is predicted
 1898 from the dilepton and photon + jets control regions. Five transfer factors are therefore needed to
 1899 connect the control regions to the signal region. An additional transfer factor is used between the
 1900 $Z(\nu\nu) + \text{jets}$ and $W(l\nu) + \text{jets}$ backgrounds to factor in the experimental as well as theoretical
 1901 correlations between these two backgrounds.

For the prediction using $Z \rightarrow \mu\mu$ events in the dimuon control region for example, the

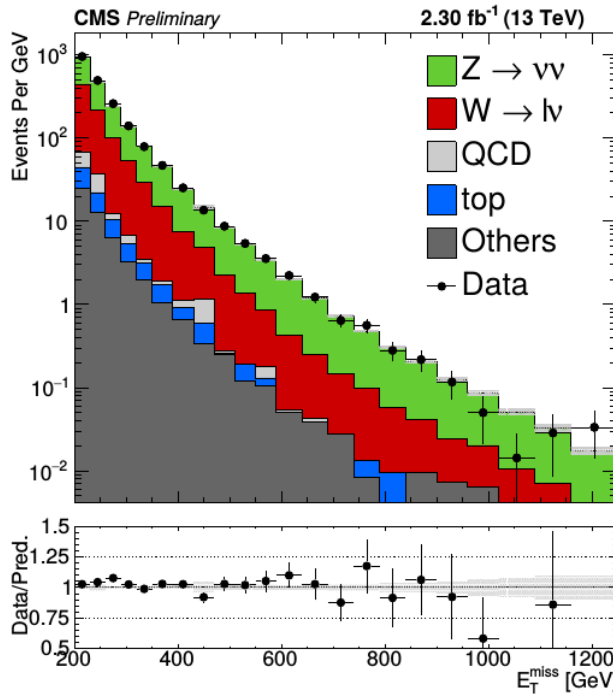


Figure 5.5: The missing transverse momentum distribution after applying the described event selection, for data and MC.

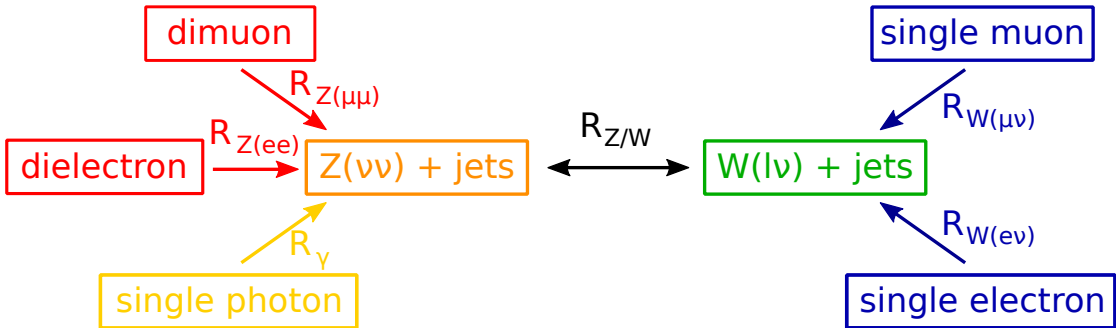


Figure 5.6: Schematic overview of the five control regions used to estimate the $Z(\nu\nu)$ and $W(l\nu) + \text{jets}$ backgrounds with the transfer factors.

predicted yield of $Z \rightarrow \nu\nu$ events is given by

$$N_{Z(\nu\nu)} = \frac{N_{Z(\mu\mu)}^{\text{data}}}{N_{Z(\mu\mu)}^{\text{MC}}} N_{Z(\nu\nu)}^{\text{MC}} \quad (5.1)$$

$$= \frac{N_{\mu\mu}^{\text{data}} - N_{\text{Bkgd}}}{N_{Z(\mu\mu)}^{\text{MC}}} N_{Z(\nu\nu)}^{\text{MC}} \quad (5.2)$$

$$= \left(N_{\mu\mu}^{\text{data}} - N_{\text{Bkgd}} \right) R_{Z(\mu\mu)}, \quad (5.3)$$

1902 where the number of $Z(\mu\mu) + \text{jets}$ events in data $N_{Z(\mu\mu)}^{\text{data}}$ is given by the number events in
 1903 the dimuon sample, removing the number of background events, and $N_{Z(\mu\mu/\nu\nu)}^{\text{MC}}$ represent the
 1904 number of $Z(\mu\mu/\nu\nu) + \text{jets}$ events in MC. The five transfer factors, denoted by R , are derived

1905 from simulation and take into account the impact of lepton acceptance and efficiency, as well
 1906 as the additional E_T^{miss} requirement for the single electron control region. They also include
 1907 the difference in branching ratio and the relation between the differential cross sections of the
 1908 photon, W , and Z boson production as a function of the boson p_T . The transfer factors are
 1909 computed as a function of the hadronic recoil, and are shown in Figure 5.7. Furthermore, the
 1910 Z/W ratio shown in the bottom right plot of Figure 5.7 provides an additional constraint between
 1911 the $Z(\nu\nu) + \text{jets}$ and $W(l\nu) + \text{jets}$ backgrounds.

1912 The simulated samples used for the background estimation are generated at leading order
 1913 (LO) using the MADGRAPH generator, and corrected to next-to-leading order (NLO). These
 1914 corrections are crucial in order correctly represent the data since inclusively, the simulation is
 1915 approximately 40% higher than the data when using only LO calculations. The NLO QCD k-
 1916 factors are derived from samples generated at NLO with MADGRAPH5_aMC@NLO, while the
 1917 NLO electroweak k-factors are obtained from theoretical calculations [150–153]. The differ-
 1918 ential cross section as a function of the boson p_T is shown in Figure 5.8 for photon, W , and
 1919 Z production, and the obtained k-factors are displayed in the ratio plots. More details on the
 1920 different control regions are given in the following.

1921 **Dimuon control region**

1922 In the dimuon control region the events are selected using the monojet triggers and ap-
 1923 plying the same requirements as described in Section 5.3 for the signal region, using the
 1924 hadronic recoil instead of the missing transverse momentum, except for the muon veto.
 1925 Additionally, exactly two muons with opposite charge should be identified using the loose
 1926 identification, and at least one should also pass the tight selection requirements. The lead-
 1927 ing muon should have a transverse momentum larger than 20 GeV, and the second one
 1928 should have $p_T > 10$ GeV. Finally, the dimuon mass should be between 60 and 120 GeV,
 1929 corresponding to the Z boson mass.

1930 **Single muon control region**

1931 In order to model the second largest background, coming from $W(l\nu) + \text{jets}$ events, a
 1932 single muon control region is used. This control region is in addition also used to constrain
 1933 the $Z(\nu\nu) + \text{jets}$ background. The events in the single muon control region are required to
 1934 pass the monojet triggers and event selection replacing the E_T^{miss} by the hadronic recoil
 1935 obtained by removing the muon, except for the muon veto. One muon should then pass
 1936 the tight selection requirements and have $p_T > 20$ GeV.

1937 **Dielectron control region**

1938 The dielectron control region is also used to constrain the $Z \rightarrow \nu\nu$ background. The
 1939 events are selected by the single electron triggers. Similarly to the dimuon control region,
 1940 the events are required to pass the monojet selection, except for the electron veto. Instead,
 1941 exactly two electrons with $p_T > 10$ GeV are required to pass the loose identification
 1942 described in Section 4.3.3. In addition, at least one electron should pass the tight selection
 1943 requirements, and the leading electron is required to have $p_T > 40$ GeV in order to have
 1944 a high probability to have passed the single electron trigger. Finally, the dielectron mass
 1945 should be between 60 and 120 GeV, in order to be consistent with a Z boson decay. The
 1946 jump that can be observed in the last bin of the resulting transfer factor in the middle left
 1947 plot of Figure 5.7 is due to the isolation requirement of the single electron trigger. This
 1948 was verified by removing the trigger selection in MC, yielding a flat transfer factor.

1949 **Single electron control region**

1950 The single electron control region is used to constrain the $W(l\nu) + \text{jets}$ background. In
 1951 the single electron control region, the events are required to have one electron with $p_T >$
 1952 40 GeV passing the tight selection requirements, analogous to the single muon control
 1953 region. In this region, a large amount of QCD background is however present due to
 1954 jets being wrongly reconstructed as electrons. In order to reject most of those events, an

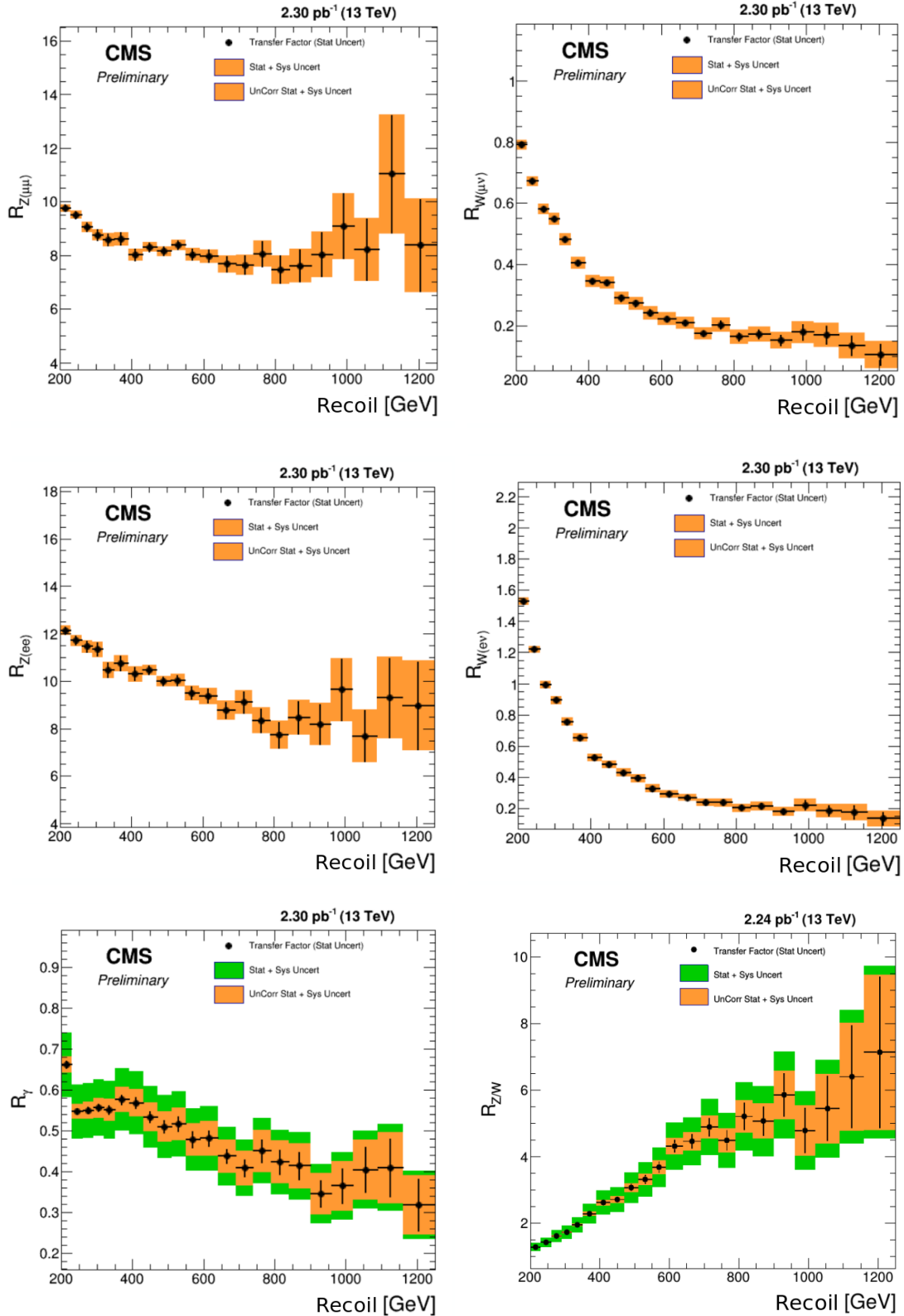


Figure 5.7: Transfer factors for the dimuon (top left), single muon (top right), dielectron (middle left), single electron (middle right), and photon + jets (bottom left) control regions. The ratio of the Z and W transfer factors is shown in the bottom right plot.

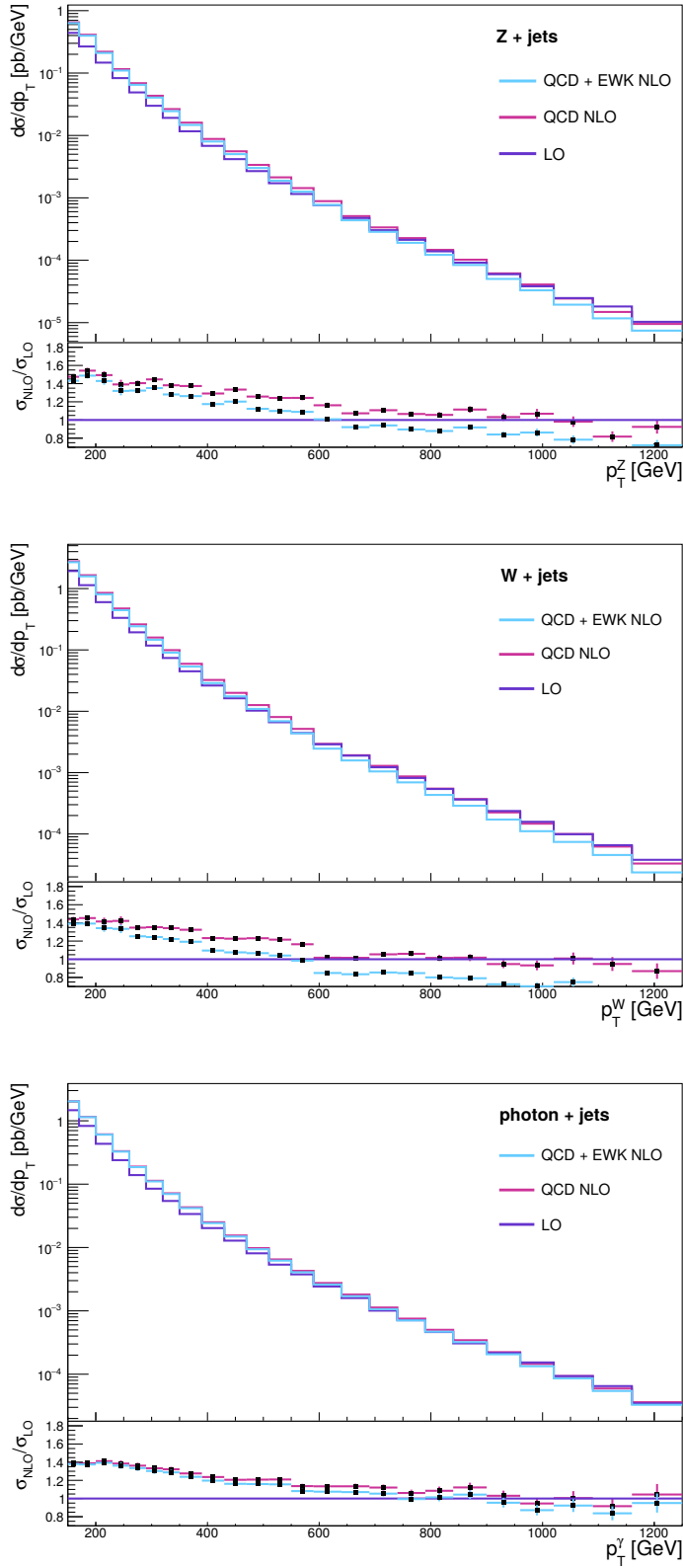


Figure 5.8: The differential cross section as a function of the boson p_T for photon, W , and Z production, using boson p_T -binned NLO samples. The resulting k-factors are shown in the ratio plots.

additional cut on the E_T^{miss} , which includes the single electron, is added at 50 GeV. This reduces the QCD background by an order of magnitude.

Photon + jets control region

Due to its large yield, the photon + jets control region provides the dominant constraint on the high- p_T part of the $Z(\nu\nu) + \text{jets}$ background. The selection of these events is done using the single photon triggers and applying the monojet selection, except for the photon veto. One photon is then required to pass the tight identification and to have $p_T > 175$ GeV. Additionally, it should be reconstructed inside the ECAL barrel ($|\eta| < 1.4442$) in order to achieve a high purity of at least 95%. Events with more than one photon passing the loose identification requirements described in Section 4.3.3 are rejected.

5.4.2 The QCD background estimation

While QCD multijet background events are generally well balanced in the transverse plane, missing transverse momentum can arise in the event due to jet energy mismeasurements, punch-through¹, uninstrumented or defective regions in the detector, hot spots, or neutrinos from decays of heavy-flavour mesons. Although these effects will very rarely yield a large missing transverse momentum, the QCD production cross section is very large compared to other processes, and some events can be selected at high missing transverse momentum. The event selection detailed in Section 5.3 was designed to suppress contributions from the QCD multijet background, reducing it to the percent level. However, this background is not well reproduced in the simulation, and thus requires a background estimation using a data control region.

The yield is predicted using the $\Delta\phi$ extrapolation method, the QCD background is estimated in data selected using the signal triggers and applying the events selection, but inverting the $\Delta\phi$ selection cut and instead requiring $\min \Delta\phi(\text{jet}, E_T^{miss}) < 0.5$. An extrapolation is then made to the signal region using transfer factors derived from simulated events generated at LO with MADGRAPH in several bins of H_T . The obtained estimation using this method yields a contribution that is a factor 2 larger than the prediction from simulation, as can be seen in Figure 5.9.

5.4.3 Simulation-based background estimation

Contributions are also expected from diboson production, from top quark decays, both from $t\bar{t}$ and single top production, and from $Z(l\bar{l}) + \text{jets}$ events where the leptons are not detected. These backgrounds are estimated from MC simulations.

Top quarks typically decay into a W boson and a b quark. When the W boson decays leptonically, a neutrino is produced, generating genuine missing transverse momentum. If the event is not removed by the b -jet veto and the lepton is not identified, this type of events contributes to the background in the signal region. However, due to the small production cross section and the applied event selection, only a small fraction of these events are selected. In order to estimate the contribution of this background, a $t\bar{t}$ sample has been produced at LO with MADGRAPH, and single top events were generated with POWHEG at NLO.

When one of the weak bosons produced in diboson events decays leptonically, generating one or more neutrinos, and the other one decays hadronically, jets and missing transverse momentum are produced. The samples used to estimate this background have been produced using PYTHIA.

Finally, when the leptons in $Z(l\bar{l}) + \text{jets}$ events are lost or out of the detector acceptance, these events can mimic the monojet signature as well. MC samples have been generated at LO using MADGRAPH in several bins of H_T in order to estimate the contribution from this sub-dominant background.

¹It can happen that a jet is not fully contained inside the calorimeters, and leaks into the muon system. In that case, part of the energy of the jet is lost, leading to missing transverse momentum.

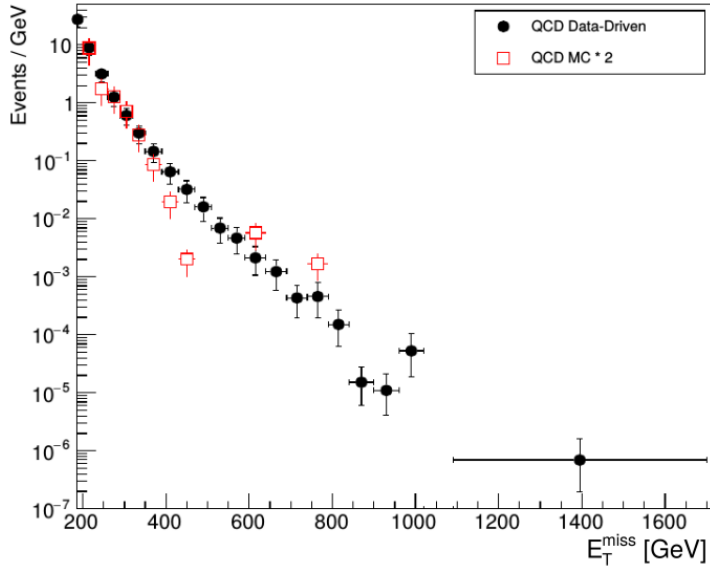


Figure 5.9: Predicted E_T^{miss} distribution of the QCD multijet background obtained using the $\Delta\phi$ extrapolation method, using data (black) and MC simulations (red). The simulation is scaled by a factor 2.

5.5 Systematic uncertainties

For the main backgrounds, multiple systematic uncertainties on the transfer factors are taken into account. Systematic uncertainties are added for the selection efficiency of muons, electrons, tau leptons, and photons, and for the photon purity in the photon + jets sample. Additionally, systematic uncertainties are added to take into account the electron and photon triggers. These uncertainties are fully correlated across the bins in recoil. The uncertainty on the modelling of the E_T^{miss} is dominated by the jet energy scale uncertainty, varying between 3 and 5%.

Uncertainties are also added from theory, to take into account variations of the factorisation and renormalisation scales, PDF uncertainties, and the NLO electroweak corrections [150–153]. The former 3 uncertainties are shown in Figure 5.10 for the $Z + \text{jets}$, $W + \text{jets}$, and photon + jets samples. The uncertainties are then propagated to the transfer factors, and are displayed in Figure 5.11. To evaluate the PDF uncertainty, the samples are reweighted with event-by-event scale factors representing the shift in the kinematic distributions from variations in the PDF. The transfer factors are then produced for each variation, and the RMS of the variation is taken as PDF uncertainty. Similarly, the renormalisation and factorisation scales are varied up and down by a factor 2, and the uncertainties are derived from the resulting transfer factors. For the electroweak corrections, the full correction is taken as an uncertainty.

The overall uncertainty on the QCD background varies between 50% and 150% depending on the E_T^{miss} region, and includes variations in the jet response and the statistical uncertainty on the transfer factors. The remaining subdominant top quark and diboson backgrounds are obtained directly from simulation. A systematic uncertainties of 20% is taken into account for the uncertainty on the production cross section of these processes. Additionally, a systematic uncertainty is added due to the uncertainty on the b-tagging applied for the b-jet veto, which amounts to 6% for the top quark background and 2% for the diboson background. The uncertainty on the modelling of the E_T^{miss} in simulation varies between 2% and 5%, depending on the E_T^{miss} . Finally, a systematic uncertainty of 2.7% [154] is added for all backgrounds derived from MC simulations, to take into account the uncertainty on the luminosity measurement.

Lastly, for the signal models described in Section 2.2.4 and simulated as summarised in Section 4.1.1, systematic uncertainties are included for the luminosity measurement (2.7%), the b-jet veto (2%), and the modelling of the E_T^{miss} distribution in simulation (2% to 5%). The

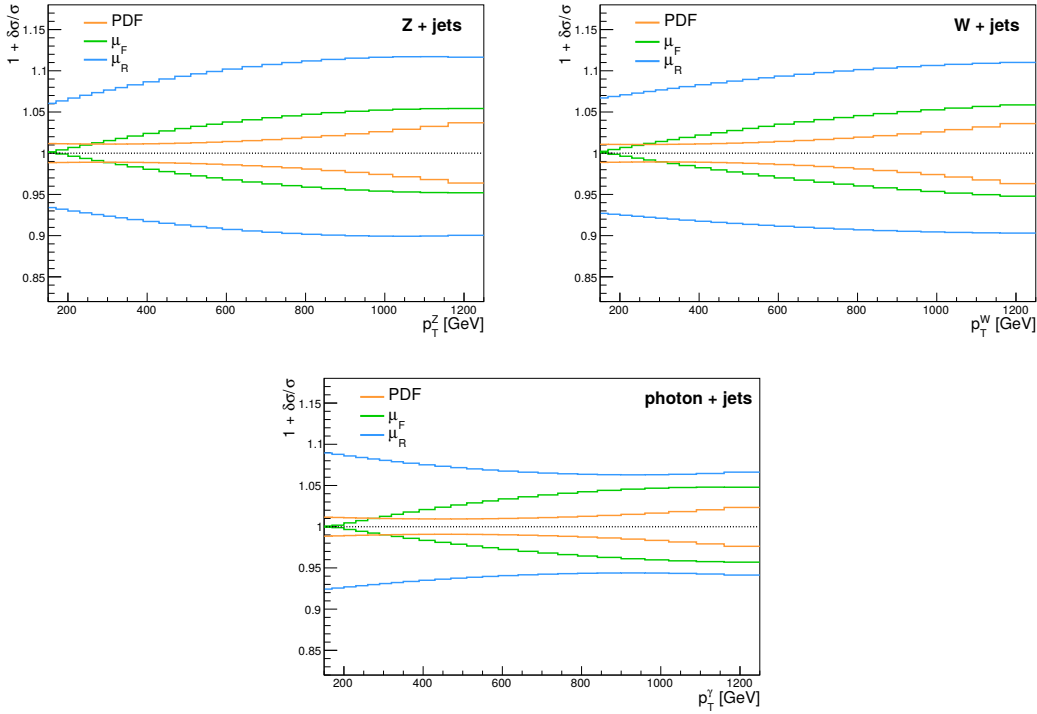


Figure 5.10: The PDF, renormalisation, and factorisation scale uncertainties for the $Z + \text{jets}$ (top left), $W + \text{jets}$ (top right), and photon + jets (bottom) samples. The uncertainties from the renormalisation and factorisation scales are obtained by separately varying them up and down by a factor 2.

2031 systematic uncertainties coming from variations of the factorisation and renormalisation scales
 2032 and PDF uncertainties amount to 20% for the vector and axial-vector signal samples and 30%
 2033 for the scalar and pseudoscalar signals.

2034 5.6 Results

2035 The results are extracted by performing a binned fit to the missing momentum spectrum, fitting
 2036 simultaneously over the five control regions and the signal region, under a given signal hypothesis.
 2037 This is done using the CL_S criterion [155, 156] in the asymptotic approximation, described
 2038 in Section 5.8, using the RooStat-based [157] Combine tool [158]. The systematic uncertainties
 2039 described in Section 5.5 are modelled as nuisance parameters and their uncertainties are propa-
 2040 gated as shape and normalization variations of the $Z(\nu\nu) + \text{jets}$ and $W(l\nu) + \text{jets}$ background.
 2041 In Figure 5.12, the nuisance parameters and their normalised uncertainties are shown before and
 2042 after the fit to the data in the control regions. Before the fit they are all centred at 0 and have
 2043 an uncertainty of 1. After the fit, the two largest deviations originate from the statistical uncer-
 2044 tainty on the Z/W transfer factor and the uncertainty on the muon scale factor, but no significant
 2045 tension is present in the fit and most nuisance parameters are not biased or constrained by the
 2046 fit. The photon + jets control region, which has the largest yields, drives the fit and the post-fit
 2047 prediction therefore corresponds well to the data. A good agreement is obtained in all control
 2048 regions, and the overall change in the transfer factors is less than 10%.

2049 Table 5.1 gives the background prediction for the various background processes in bins of
 2050 hadronic recoil, using a background-only fit. Correspondingly, the fit under the background-only
 2051 hypothesis is shown in Figure 5.13 and a good agreement is observed between the data and the
 2052 prediction. The uncertainty on the hadronic recoil is below 10% for all bins.

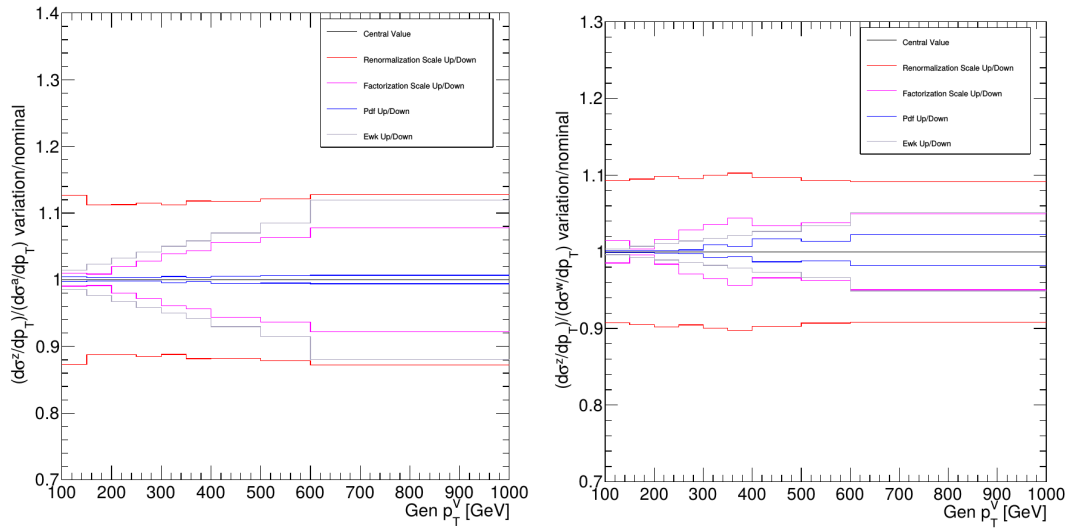


Figure 5.11: The theoretical uncertainties on the Z/γ (left) and Z/W (right) transfer factors.

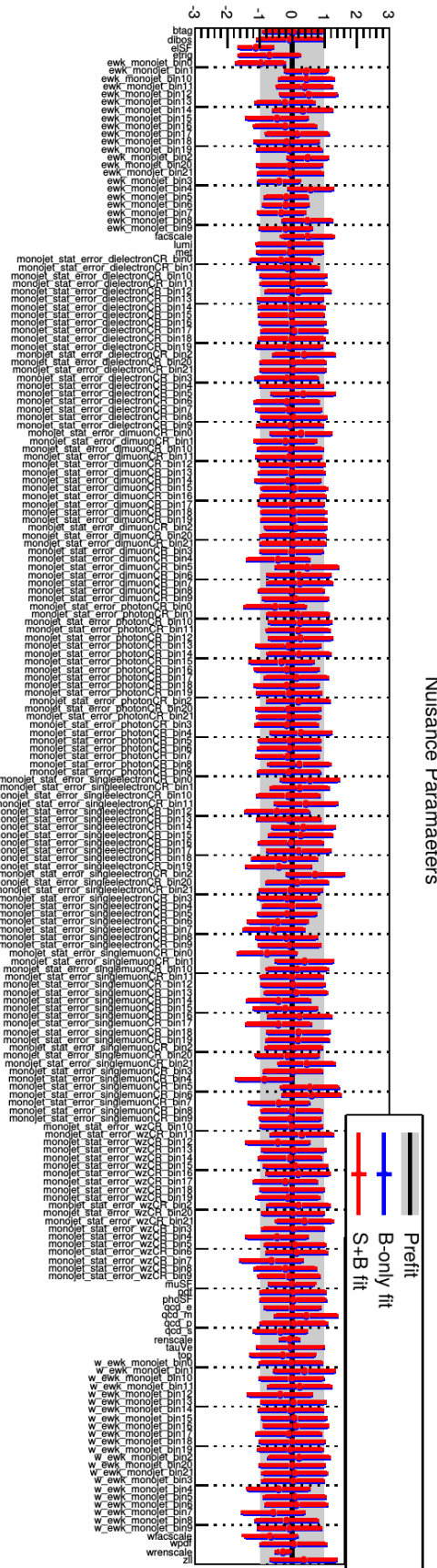


Figure 5.12: The post-fit nuisance parameters and their uncertainties, compared to the pre-fit values.

process	E_T^{miss} [200 - 230] GeV	E_T^{miss} [230 - 260] GeV	E_T^{miss} [260 - 290] GeV	E_T^{miss} [290 - 320] GeV	E_T^{miss} [320 - 350] GeV	E_T^{miss} [350 - 390] GeV	E_T^{miss} [390 - 430] GeV	E_T^{miss} [430 - 470] GeV	E_T^{miss} [470 - 510] GeV	E_T^{miss} [510 - 550] GeV	E_T^{miss} [550 - 590] GeV	E_T^{miss} [590 - 640] GeV
$Z(\nu\nu) + \text{jets}$	497	266	149	83.9	49.9	30.1	17.1	9.54	6.19	4.00	2.49	1.55
$W(l\nu) + \text{jets}$	399	193	95.6	50.7	27.3	13.9	6.87	3.86	2.18	1.30	0.73	0.38
$Z(ll) + \text{jets}$	6.88	3.10	1.26	0.61	0.33	0.10	0.05	0.02	0.01	0.01	0	0
top	18.8	8.92	3.85	1.89	1.12	0.61	0.24	0.23	0.01	0.07	0.02	0
QCD	16.9	10.3	1.28	0.99	0.17	0.10	0.13	0.41	0.01	0	0.03	0
dibosons	8.36	5.23	2.58	1.43	0.85	0.55	0.35	0.17	0.13	0.05	0.05	0.03
photon + jets	7.67	3.36	2.12	0.99	0.66	0.32	0.21	0.12	0.09	0.05	0.05	0.01
total post-fit	955 ± 6	489 ± 3	256 ± 2	141 ± 2	80.3 ± 1.2	45.7 ± 0.8	25.0 ± 0.6	14.4 ± 0.4	8.62 ± 0.32	5.49 ± 0.24	3.37 ± 0.17	1.97 ± 0.11
total pre-fit	925	470	240	136	79.5	45.4	24.5	14.7	8.45	5.30	3.37	2.02
observed	953	492	259	140	78.8	46.9	25.2	13.6	8.73	5.40	3.55	2.22

process	E_T^{miss} [640 - 690] GeV	E_T^{miss} [690 - 740] GeV	E_T^{miss} [740 - 790] GeV	E_T^{miss} [790 - 840] GeV	E_T^{miss} [840 - 900] GeV	E_T^{miss} [900 - 960] GeV	E_T^{miss} [960 - 1020] GeV	E_T^{miss} [1020 - 1090] GeV	E_T^{miss} [1090 - 1160] GeV	E_T^{miss} > 1160 GeV
$Z(\nu\nu) + \text{jets}$	0.90	0.56	0.44	0.27	0.16	0.09	0.06	0.04	0.02	0.02
$W(l\nu) + \text{jets}$	0.22	0.12	0.11	0.06	0.03	0.02	0.01	0.01	0	0
$Z(ll) + \text{jets}$	0	0	0	0	0	0	0	0	0	0
top	0	0	0	0.01	0	0	0	0	0	0
QCD	0.01	0	0	0	0	0	0	0	0	0
dibosons	0.03	0.01	0	0	0	0.01	0	0	0	0
photon + jets	0	0.01	0.01	0	0	0	0	0	0	0
total post-fit	1.16 ± 0.08	0.70 ± 0.05	0.55 ± 0.05	0.34 ± 0.04	0.20 ± 0.02	0.11 ± 0.02	0.07 ± 0.02	0.05 ± 0.01	0.03 ± 0.01	0.02 ± 0.01
total pre-fit	1.19	0.73	0.48	0.31	0.20	0.13	0.09	0.05	0.03	0.02
observed	1.22	0.64	0.56	0.28	0.22	0.12	0.05	0.01	0.03	0.03

Table 5.1: Pre-fit and post-fit background predictions in the signal region and observed yield given as number of events divided by the bin width, per E_T^{miss} bin. The predictions and uncertainties are obtained from the background-only simultaneous fit in the signal and control regions.

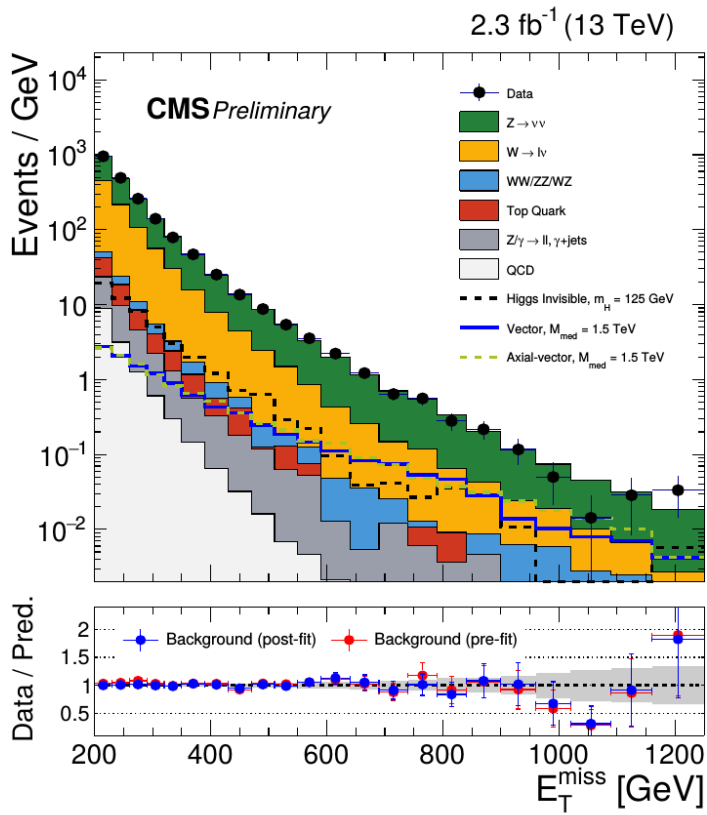


Figure 5.13: Post-fit missing transverse momentum distribution for the expected backgrounds and the observed data in the signal region. The grey band indicates the post-fit uncertainty obtained from the background-only simultaneous fit in the signal and control regions.

5.7 Improvements going from the 2015 to 2016 analysis

Several iterations of the monojet analysis were performed during Run 2 in 2015 and 2016, improving the achieved sensitivity with the increase in available data and additional developments to the analysis strategy, and adding new interpretations. In 2015, a first analysis with data at a centre-of-mass energy of 13 TeV was carried out [159], using data corresponding to an integrated luminosity of 2.1 fb^{-1} . In this first iteration of the search, the NLO k-factors applied to correct the LO samples used for the estimation of the background from Z and W bosons are derived from inclusive NLO samples, which are not binned in boson p_T . These k-factors are shown in Figure 5.14, and can be compared to the k-factors obtained from p_T -binned samples used in the following iterations of the analysis and shown in Figure 5.8.

In 2016, the analysis was extended to the mono-V channel [160], which can give rise to a monojet-like signature. At high p_T , the production of a W or Z boson which decays hadronically, can be effectively reconstructed as a single jet of large cone radius. However, in this chapter the focus is on the monojet channel and the added improvements during 2016. For this analysis, data collected in 2015 was used, corresponding to 2.3 fb^{-1} . This is the analysis reported in this chapter. The used NLO k-factors were derived using the p_T -binned samples, as described in Section 5.4.1. This contribution was a first step in the improvements I added to the analysis. I performed extensive validations, comparing the obtained k-factors to the previous results.

A substantial difference in the next iteration of the 2016 analysis [79] is the increase in collected data, which allowed to reduce the statistical uncertainties and set stronger limits on the

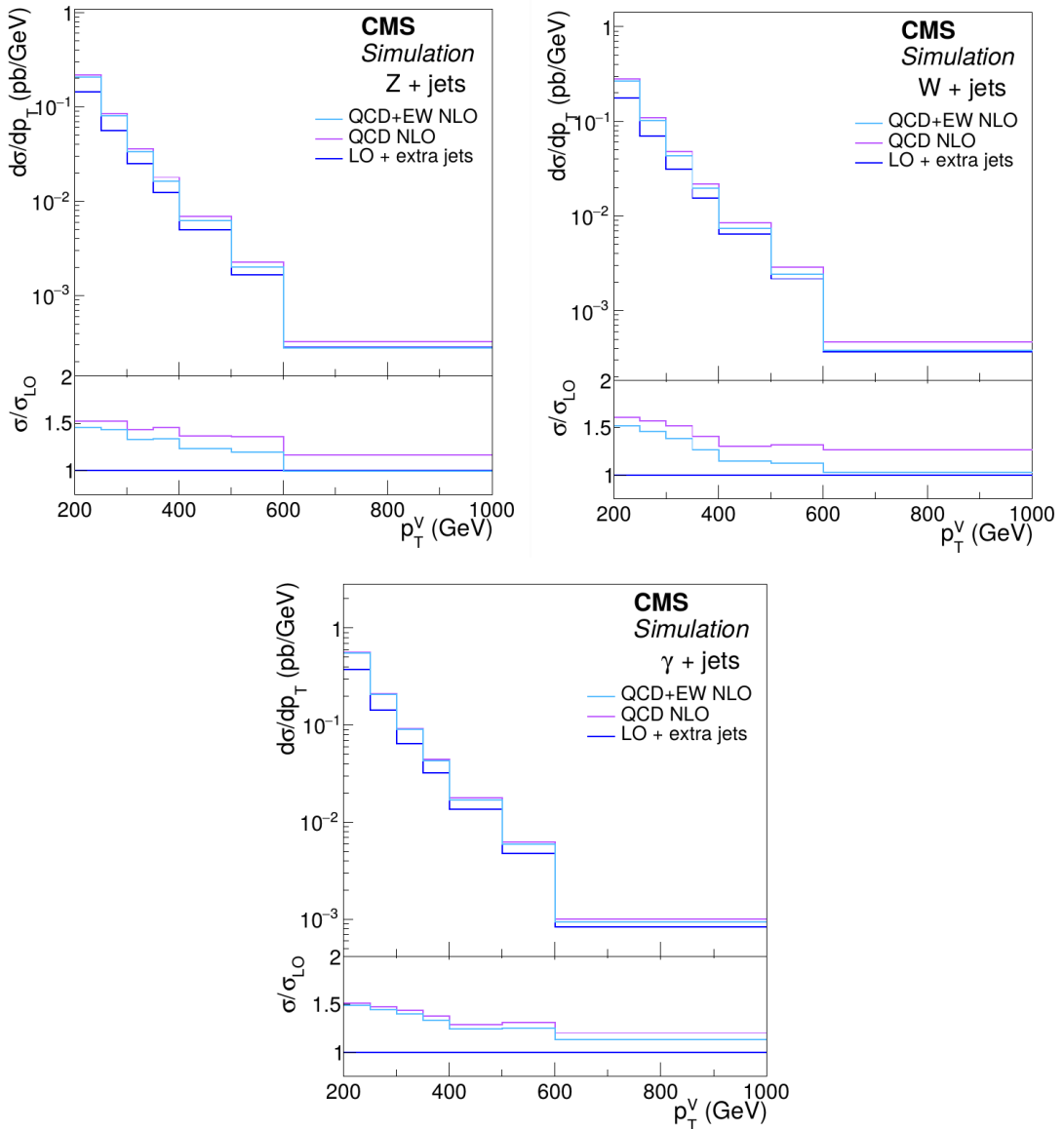


Figure 5.14: The differential cross section as a function of the boson p_T for photon, W , and Z production, using inclusive NLO samples. The resulting k-factors are shown in the ratio plots.

2074 considered models. For these results, data collected in the first half of 2016 and corresponding to
 2075 an integrated luminosity of 12.9 fb^{-1} were available. One of the improvements that were added
 2076 is the direct use of MC samples generated at next-to-leading order for the estimation of the
 2077 main backgrounds. This was possible by generating larger samples that are binned in W boson
 2078 p_T , and are now used more widely in other analyses. As a result of my second contribution to
 2079 the improvement of the background prediction, no k-factors need to be applied to the $W + \text{jets}$
 2080 sample and no additional systematic uncertainties are to be introduced for this. Figures 5.15
 2081 and 5.16 show the obtained reduction in the overall post-fit uncertainty on the predictions in the
 2082 5 control regions, which is clearly visible at high missing transverse momentum. The largest
 2083 uncertainties of about 50% in the high E_T^{miss} region are reduced to 20% or less, which is driving
 2084 the analysis sensitivity at the highest mediator masses.

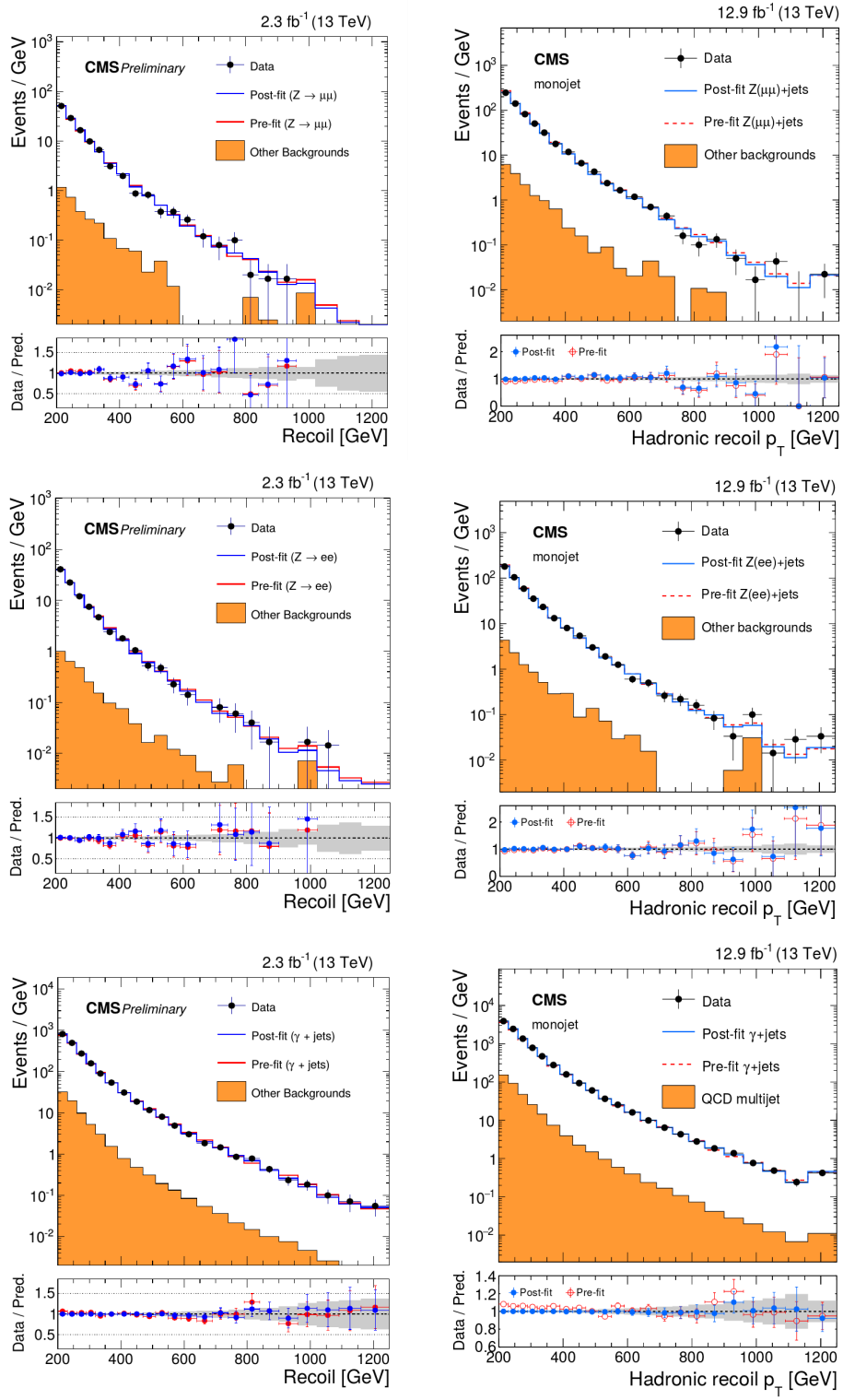


Figure 5.15: Comparison of the hadronic recoil p_T distribution between the data and MC simulation in the dimuon (top), dielectron (middle), and photon + jets (bottom) control regions, showing the reduction in overall post-fit uncertainty (grey band) going from the early 2016 analysis (left) to the analysis using data from the first half of 2016 (right). The fit was performed simultaneously over all the control and signal regions, assuming the absence of any signal. The last bin includes all events with hadronic recoil $p_T > 1160 \text{ GeV}$. Figures taken from [160] and [79].

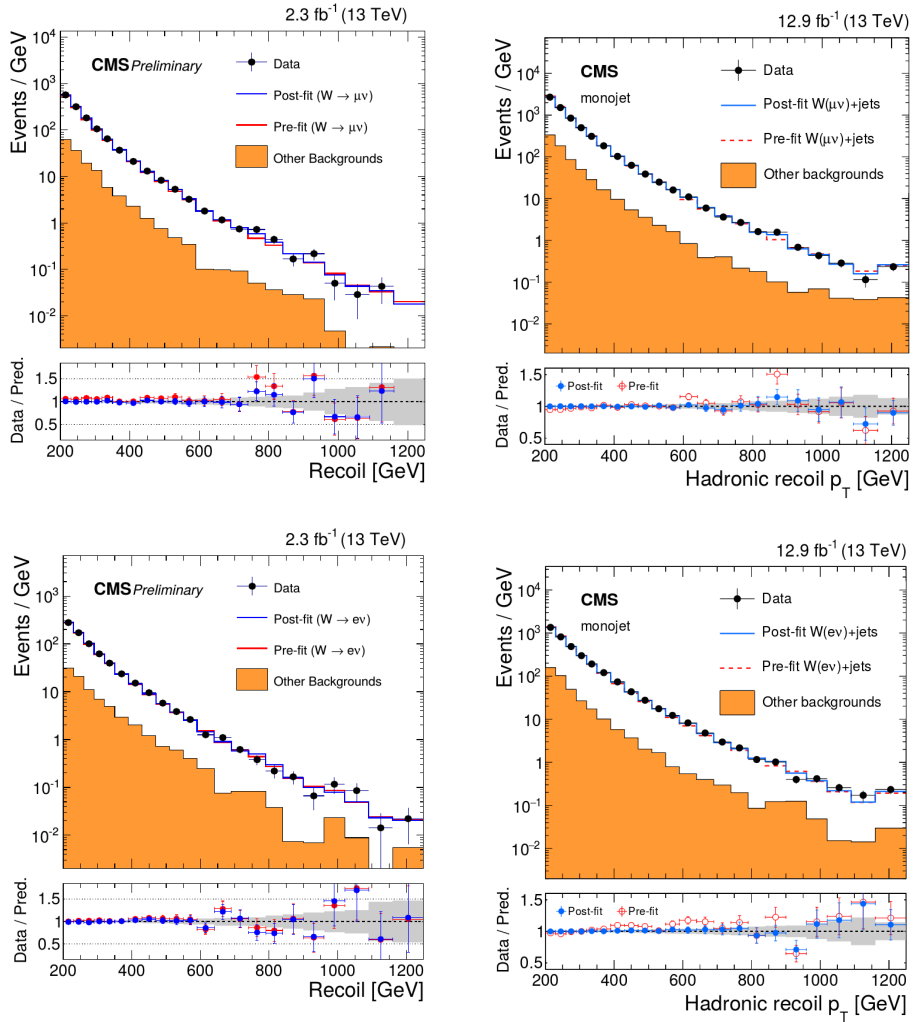


Figure 5.16: Comparison of the hadronic recoil p_T distribution between the data and MC simulation in the single muon (top) and single electron (bottom) control regions, showing the reduction in overall post-fit uncertainty (grey band) going from the early 2016 analysis (left) to the analysis using data from the first half of 2016 (right). The fit was performed simultaneously over all the control and signal regions, assuming the absence of any signal. The last bin includes all events with hadronic recoil $p_T > 1160$ GeV. Figures taken from [160] and [79].

2085 **5.8 Limit setting**

2086 As no significant excess was observed, upper limits are placed on the ratio of the signal cross
 2087 section to the predicted cross section. This limit setting on new physics models is done with re-
 2088 spect to the signal plus background hypothesis, comparing it to the background only hypothesis
 2089 in which no new physics is present. Typically, a specific variable, for which different outcomes
 2090 are predicted in the different hypotheses, is used to build a test statistic. The distribution of the
 2091 test statistic is constructed by generating pseudo-experiments for each hypothesis. In case the
 2092 expected number of events is large, the asymptotic approximation [161] is used to reduce the
 2093 large computing time, replacing the pseudo-experiments by a single so-called Asimov data set.

2094 The CL_S method [155, 156] is then used to determine the compatibility of the signal hy-
 2095 pothesis with the observed data and to derive the upper limits at a certain confidence level (CL).
 2096 In this thesis, the LHC style test statistic [162] is used, given by

$$q_\mu = -2 \ln \frac{\mathcal{L}(\text{data}|\mu, \hat{\theta}_\mu)}{\mathcal{L}(\text{data}|\hat{\mu}, \hat{\theta})} \quad (0 \leq \hat{\mu} \leq \mu), \quad (5.4)$$

2097 where μ is the signal strength, θ_μ are the nuisance parameters for a given μ , $\hat{\mu}$ is the maximum
 2098 likelihood value of μ , and $\hat{\theta}_\mu$ are the corresponding nuisance parameters. The signal strength
 2099 represents the fraction of the theoretical cross section corresponding to the considered hypoth-
 2100 esis. When constructing the distribution of the used variable, the expected number of events in
 2101 the i -th bin is then $\mu s_i + b_i$, with s_i and b_i the number of predicted signal and background events
 2102 in that bin. $\mu = 0$ thus corresponds to the background only hypothesis, and $\mu = 1$ corresponds
 2103 to the signal plus background hypothesis using the nominal theoretical cross section.

2104 Adding a given observation of the test statistic, $q_{\mu, \text{obs}}$, from a measurement in data, the
 2105 probability to find a data set with value of the test statistic equal or larger under the signal plus
 2106 background hypothesis can be written as

$$p_{s+b} = \int_{q_{\mu, \text{obs}}}^{\infty} f_{s+b}(q_\mu | \mu) dq_\mu, \quad (5.5)$$

2107 where $f_{s+b}(q_\mu | \mu)$ is the probability density function of the signal plus background hypothesis
 2108 constructed from the pseudo-experiments. Similarly, the probability to find a data set equally or
 2109 more incompatible with the background only hypothesis is given by

$$1 - p_b = \int_{-\infty}^{q_{\mu, \text{obs}}} f_b(q_\mu | 0) dq_\mu. \quad (5.6)$$

2110 In these equations, p_{s+b} and p_b are the p-values associated to the two hypotheses. The CL_S
 2111 value, which represents the compatibility of the signal hypothesis with the observed data, is
 2112 defined as the ratio of these two probabilities:

$$CL_S = \frac{p_{s+b}}{1 - p_b} \quad (5.7)$$

2113 Models can then be considered to be excluded at 95% CL when $CL_S \leq 0.05$.

2114 **5.9 Interpretation**

2115 The results of the second iteration of this search, using the mono-V final state as well, are
 2116 interpreted in terms of simplified dark matter models assuming a vector, axial-vector, scalar,
 2117 or pseudoscalar mediator decaying to a pair of fermionic dark matter particles, as described in
 2118 Section 2.2.4. As no significant excess was observed, upper limits are placed at 95% confidence

level (CL) on the ratio of the signal cross section to the predicted cross section, $\mu = \sigma/\sigma_{th}$, following the method described in Section 5.8. These limits are shown as a function of the mediator mass (m_{med}) and the dark matter mass (m_{DM}) in Figures 5.17 and 5.18, for the four types of mediators. The regions where the 95% CL upper limits on μ are less than one are considered to be excluded.

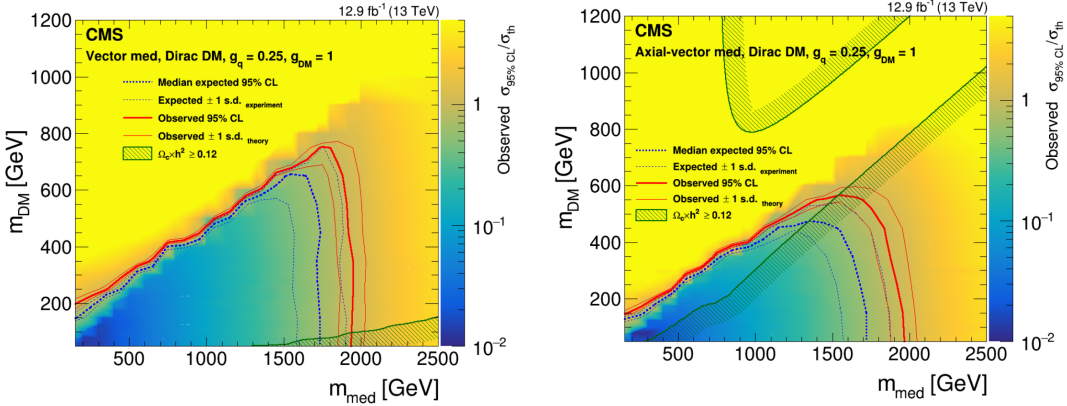


Figure 5.17: The 95% CL upper limits on the $\mu = \sigma/\sigma_{th}$ in the $m_{\text{med}} - m_{\text{DM}}$ plane, for a vector (left) or axial-vector (right) mediator. The cosmological constraints from the WMAP and Planck measurements of the CMB are shown as well. Figures taken from [79].

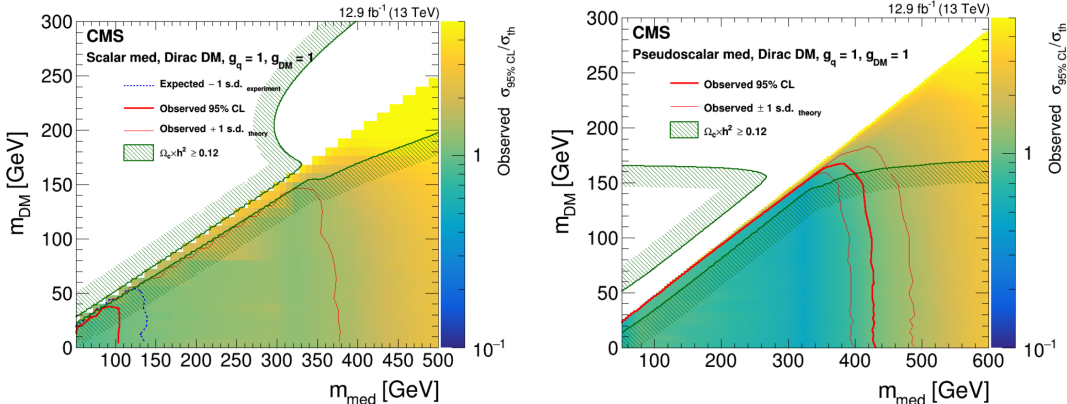


Figure 5.18: The 95% CL upper limits on the $\mu = \sigma/\sigma_{th}$ in the $m_{\text{med}} - m_{\text{DM}}$ plane, for a scalar (left) or pseudoscalar (right) mediator. The cosmological constraints from the WMAP and Planck measurements of the CMB are shown as well. Figures taken from [79].

For the vector and axial-vector models, mediator masses up to 1.95 TeV are excluded, while mediator masses up to 100 GeV and 430 GeV can be excluded for the scalar and pseudoscalar models, respectively. Figures 5.17 and 5.18 also show the constraint from the observed cosmological relic density of dark matter, which was determined from the WMAP and Planck CMB measurements. The expected dark matter abundance is estimated using a thermal freeze-out mechanism and compared to the observed cold dark matter density, assuming that the considered dark matter candidate is the dominant component of the observed dark matter.

The obtained limits can also be translated into 90% CL upper limits on the dark matter-nucleon scattering cross section $\sigma_{\text{SI/SD}}$, in order to compare them to results from direct detection experiments. The exclusion contours in the $m_{\text{DM}} - \sigma_{\text{SI/SD}}$ plane are obtained following the approaches outlined in [163–165], where σ_{SI} stands for spin-independent and σ_{SD} for spin-

dependent dark matter-nucleon cross section. The resulting limits are shown in Figures 5.19 and 5.20.

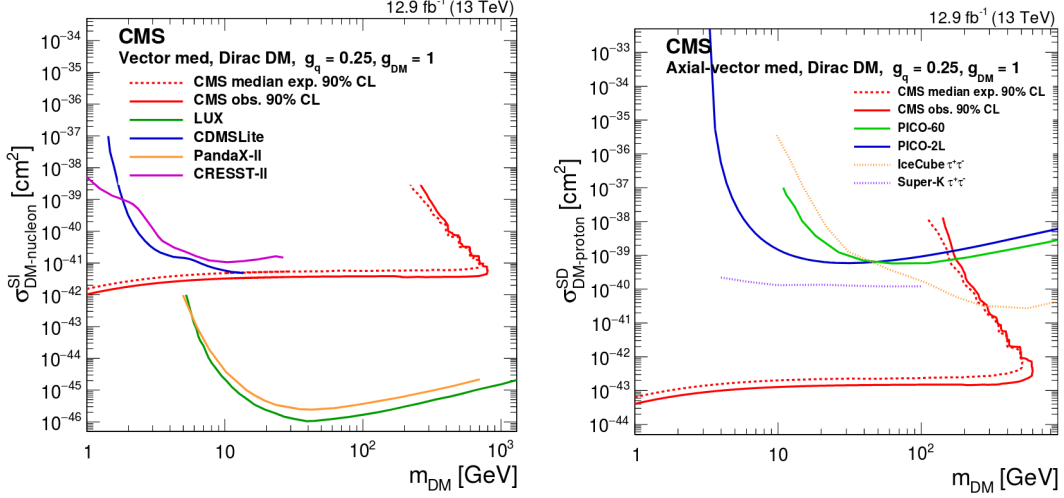


Figure 5.19: The 90% CL upper limits in the $m_{\text{DM}} - \sigma_{\text{SI/SD}}$ plane, for a vector (left) or axial-vector (right) mediator. Figures taken from [79].

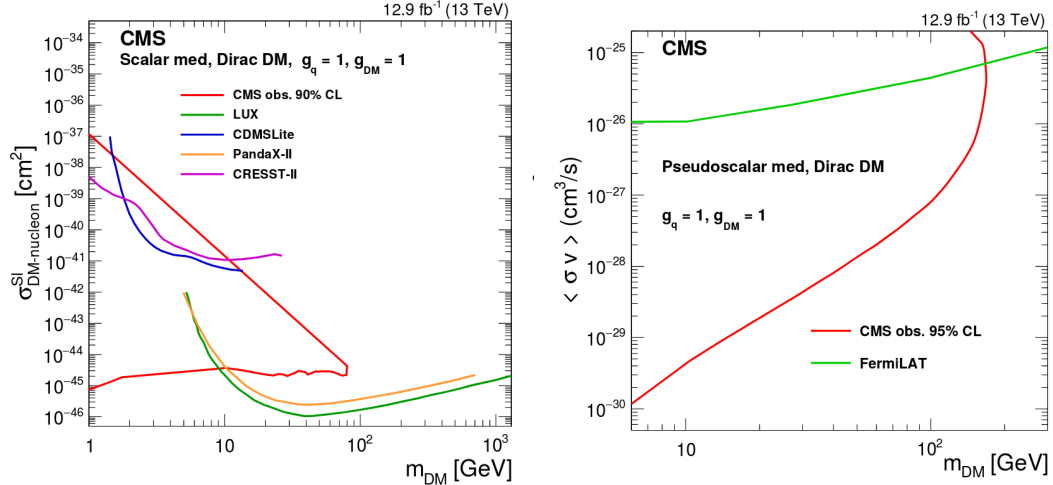


Figure 5.20: The 90% CL upper limits in the $m_{\text{DM}} - \sigma_{\text{SI/SD}}$ plane, for a scalar (left) or pseudoscalar (right) mediator. Figures taken from [79].

For the vector and scalar mediator cases, the derived 90% CL upper limits on the spin-independent cross section are compared to the results from the CDMSLite [166], LUX [167], CRESST-II [168], and PandaX-II [169] experiments. This shows that the monojet limits are complementary to the results from the direct detection experiments at low dark matter masses. The 90% CL upper limits on the spin-dependent cross section for the axial-vector mediator are compared to the PICO-2L [170], PICO-60 [171], IceCube [172], and Super Kamiokande experiments [173]. In the case of the pseudoscalar mediator, the obtained limits are compared to the indirect detection results from the Fermi-LAT experiment [174, 175]. In the considered scenario the dark matter annihilates into b quark pairs in the centre of the galaxy, producing gamma rays.

6

2147

2148

Search for SIMPs using Trackless Jets

2149 The monojet dark matter search detailed in Chapter 5 can be complemented at high interaction
2150 cross sections by a different search which does not look for dark matter in the form of missing
2151 transverse momentum. Indeed, if the dark matter particles have an interaction cross section of
2152 the order of the strong interaction, they will interact in the detector, mainly in the calorimeters.
2153 The analysis described in this chapter is based on this scenario, and the considered simplified
2154 model is specified in Section 2.3.1. In this model, the dark matter particles are produced in pairs
2155 through a new strongly interacting mediator, and give rise to a pair of trackless jets as signature.
2156 Since the produced strongly interacting massive particles (SIMPs) are neutral, the resulting jets
2157 can be distinguished from QCD jets using the jet charged energy fraction (ChF). The signal
2158 region where the SIMPs are being looked for is therefore defined by requiring the two leading
2159 jets to have a low ChF. In the control region, which is used to predict and validate the expected
2160 background, one or both jets are required to have a large ChF.

2161 Firstly, the applied jet and photon reconstruction and identification are described, as well
2162 as the specific treatment applied for the primary vertex selection. The triggers that were de-
2163 signed specifically for this search, exploiting the ChF, are outlined in Section 6.2. However,
2164 these triggers were found to be problematic and eventually a generic single jet trigger was used
2165 instead. Next, the event selection is detailed in Section 6.3 for both the signal and control re-
2166 gions. The strategy for the background estimation and the systematic uncertainties are discussed
2167 in Sections 6.4 and 6.5, respectively. Finally, in Sections 6.6 and 6.7, the results are shown and
2168 interpreted in terms of the SIMP simplified model described in Section 2.3.

2169 6.1 Physics object reconstruction

2170 In this analysis, jets with a very small charged energy fraction (ChF) are being searched for.
2171 Since these are rather peculiar jets containing no or very few tracks, a good primary vertex
2172 selection and photon identification play an important role in suppressing the main physics and
2173 reconstruction backgrounds.

2174 6.1.1 Jets

2175 For the jet reconstruction, the standard method described in Section 4.3.7 is used. Although
2176 the jets in the signal samples are expected to be neutral, it is beneficial to use PF jets because
2177 they directly provide an unambiguous association of tracks to jets. The standard jet energy

2178 corrections are applied as well, while the standard jet identification criteria are not used, since
 2179 several of the quality criteria would actually remove the neutral SIMP jets.

2180 6.1.2 Photons

2181 Since photons might be reconstructed as neutral jets, photon + jets events are an important
 2182 background for the control as well as the signal region. The photons therefore need to be iden-
 2183 tified and rejected, which is done using the standard photon loose identification described in
 2184 Section 4.3.3. Further photon rejection is achieved by analysis-specific selections on photon
 2185 conversions and on the jet neutral electromagnetic energy fraction (NEMF), as described in Sec-
 2186 tion 6.3.

2187 6.1.3 Primary vertex

2188 The standard primary vertex reconstruction described in Section 4.3.1 sometimes provides a
 2189 wrong primary vertex, which arises from a pileup interaction. The choice of a wrong vertex
 2190 is not a problem in the case of signal events, which will pass in particular the ChF cuts in the
 2191 event selection detailed in Section 6.3 just as easily. However, a wrongly chosen vertex in a
 2192 QCD background event leads to the jets having an artificially very low ChF, both in simulation
 2193 and data, as the standard charged hadron subtraction (CHS) procedure will remove the tracks
 2194 from the vertex of the true hard interaction. This makes such events appear signal-like. For the
 2195 lowest jet charged energy fractions considered in this analysis, this background of events with
 2196 a misidentified primary vertex becomes dominant with respect to the background from QCD
 2197 events with a very rare jet fragmentation into predominantly neutral hadrons and photons. In
 2198 Figure 6.1 an event display is shown that demonstrates such a wrong choice of vertex.

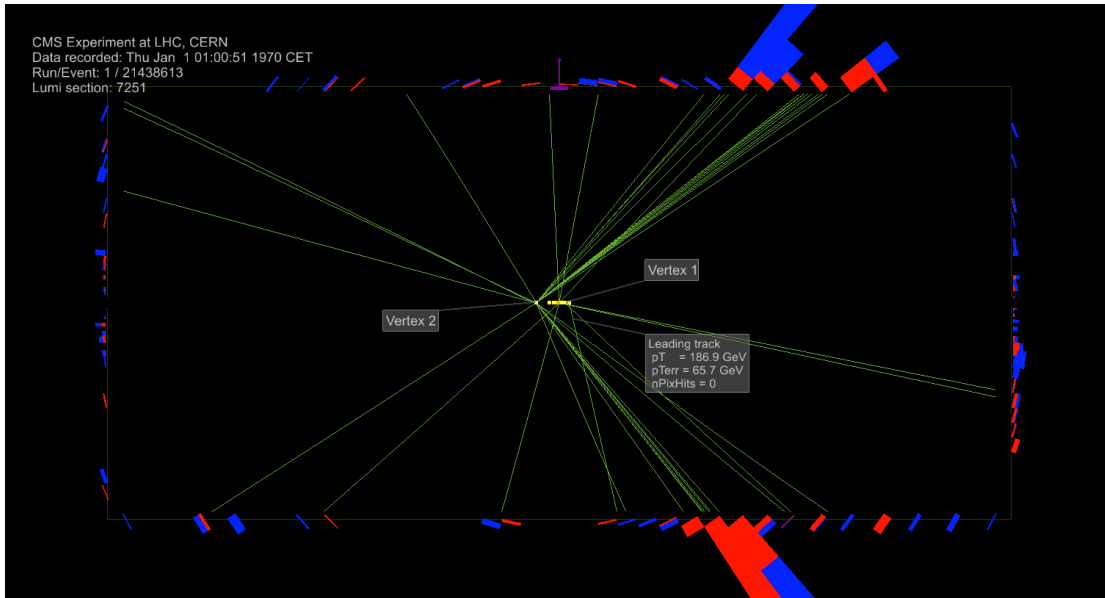


Figure 6.1: Event display showing an example of a wrong primary vertex selection in a MC simulated QCD event. Although "Vertex 2" is the real vertex of the hard collision, "Vertex 1" is selected because of the presence of a single high- p_T track with poor momentum resolution and no pixel hits attached. As a result, the two visible high- p_T jets (above 200 GeV), clearly with many tracks attached, are reconstructed with only 3% and 4% of charged energy fraction.

2199 Investigating this problem, many events with a wrong vertex assignment were observed to
 2200 have the highest- p_T track being of poor quality, with a high momentum with large uncertainty,
 2201 and no pixel hits. This alone, though, does not provide a sufficient handle to suppress this

background, and a plain cut on number of pixel hits was verified to remove a lot of signal events as well. Studying the simulated QCD multijet events with a very low ChF coming from primary vertex misidentification by analysing event displays also showed that the true vertex is reconstructed as the second vertex in the list for the far majority of the cases. A second jet reconstruction was therefore produced, based on selecting the second entry in the list of primary vertices to be the event’s collision vertex, and rerunning the CHS as well. If this second vertex was the correct one, the jets will now have a large ChF in most of the cases, while the first event reconstruction yields low-ChF jets. In the event selection discussed in Section 6.3, it is then sufficient to ask both event reconstructions to pass the cut of low jet ChF, effectively suppressing this background induced from wrong primary vertex selection.

6.2 Trigger selection

Several triggers have been designed specifically for this analysis, as shown in Table 6.1. Four triggers were available to select signal events, denoted as “signal” in the table and providing a trade-off between a high ChF and a low jet p_T . The ChF cut is always applied on both jets. Two additional triggers, indicated with the “control” type, were used to determine the trigger efficiencies. These triggers were prescaled, meaning that only a fraction of the events are kept due to the otherwise very high rate of the trigger.

Trigger name	Type	Int. Lumi.
HLT_DiCentralPFJet170_CFMMax0p1_v*	Signal	33.1 fb^{-1}
HLT_DiCentralPFJet220_CFMMax0p3_v* ¹	Signal	5.91 fb^{-1}
HLT_DiCentralPFJet330_CFMMax0p5_v*	Signal	33.1 fb^{-1}
HLT_DiCentralPFJet430_v*	Signal	33.1 fb^{-1}
HLT_DiCentralPFJet170_v*	Control	0.101 fb^{-1}
HLT_SingleCentralPFJet170_CFMMax0p1_v*	Control	0.375 fb^{-1}

Table 6.1: Summary of the triggers designed for this analysis, with the corresponding integrated luminosity collected for each trigger.

These triggers were designed to select events containing jets with a low ChF, but keeping the jet p_T threshold as low as possible, while taking the limited trigger rate into account. Their performance was tested using simulated QCD events before using them in data taking. The trigger efficiency of HLT_DiCentralPFJet330_CFMMax0p5 as a function of p_T and ChF is shown in Figure 6.2, using data and simulated QCD events. The plot on the left shows the efficiency as a function of p_T , which quickly reaches a plateau at 100% around 350 GeV, as expected. The efficiency as a function of ChF is shown on the right and also shows a plateau at 100% for low ChF. The slope of the turn-on is however less steep and only reaches the plateau around 0.35, for a threshold at ChF = 0.5 at trigger level. The signal efficiency measurement was first tried by taking a photon + jet sample, as photons could also mimic neutral jets. The photon was matched to the leading jet within a ΔR cone, and the efficiency was measured at low ChF. However, as the jet is reconstructed with a large electromagnetic energy fraction (EMF) and it does not mimic the SIMP signal.

Instead, one of the neutron signal samples described in Section 4.4 was used, generated with a SIMP mass of 700 GeV. The obtained trigger efficiency as a function of p_T and ChF is shown in Figure 6.3 for HLT_DiCentralPFJet330_CFMMax0p5, comparing the data and the signal-like events. This shows that the trigger reaches a plateau at only 60% signal efficiency.

¹Due to the unexpected high rate, this trigger was disabled after some time.

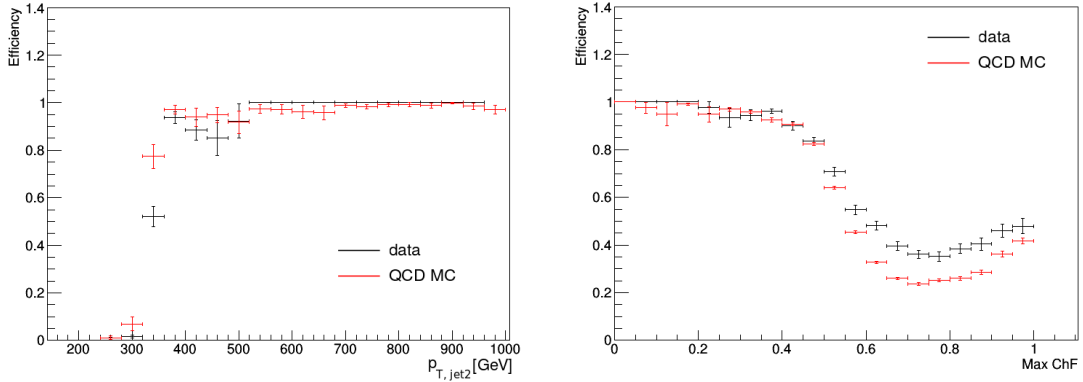


Figure 6.2: The HLT_DiCentralPFJet330_CFMMax0p5 trigger efficiency as a function of p_T (left) and ChF (right). Comparison between data (black) and QCD simulation (red).

2236 The origin of the inefficiency was found to come from a hidden requirement asking at least one
 2237 charged particle in the jets. This explains why the trigger efficiencies turn on at the expected
 2238 values when using data or simulated QCD events, where jets nearly always contain some tracks,
 2239 while it is largely inefficient in signal-like simulation which generates neutral jets.

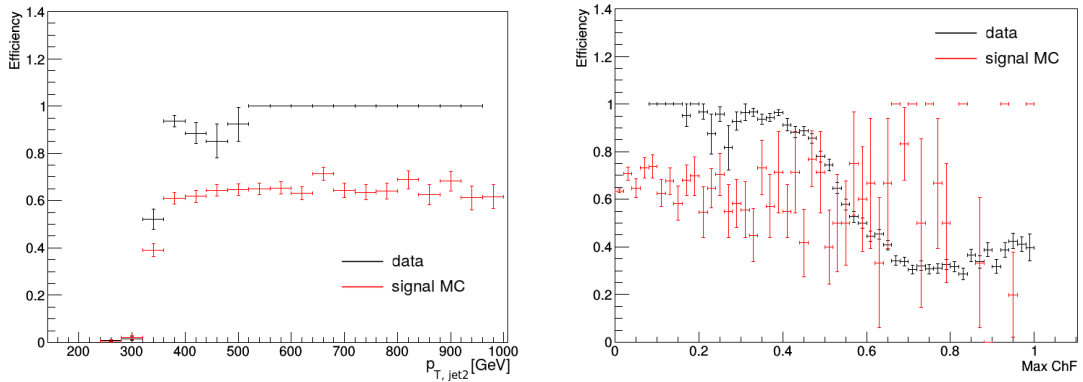


Figure 6.3: The HLT_DiCentralPFJet330_CFMMax0p5 trigger efficiency as a function of p_T (left) and ChF (right). Comparison between data (black) and signal-like MC (red).

2240 After this problem had been uncovered, the single jet trigger HLT_PFJet 450 has been
 2241 used for the analysis. It was selected because it has the lowest threshold among the unprescaled²
 2242 single jet triggers. The trigger efficiency for the data was measured using single muon events,
 2243 and is defined as

$$\epsilon = \frac{\text{Obs}(\text{HLT_PFJet 450 and HLT_IsoMu24})}{\text{Obs}(\text{HLT_IsoMu24})}, \quad (6.1)$$

2244 where Obs in this case is the p_T spectrum of the leading jet for events that fired the single muon
 2245 (and single jet) trigger. The jets are required to have a muon energy fraction smaller than 0.3 in
 2246 order to avoid jets with large difference in the online and offline p_T . This difference can arise
 2247 when the offline PF jet contains a high- p_T muon. Since the online jet is reconstructed using only
 2248 information from the calorimeters, this can significantly change the total p_T of the jet between
 2249 online and the offline PF jet. The trigger efficiency was also measured in the simulated QCD and

²Triggers with a lower p_T threshold exist, but these are prescaled. Prescaled triggers are typically not used to perform an analysis, as only a small fraction of the events that pass the trigger are kept, leading to large statistical uncertainties.

2250 neutron signal samples. In this case the denominator is the p_T spectrum of leading jet without
 2251 any trigger selection, while the numerator is the p_T spectrum of the events firing the single jet
 2252 trigger. Figure 6.4 shows the turn-on curves for data, QCD events, and the signal-like events.
 2253 The trigger efficiency was found to be 98% for jets with $p_T > 550$ GeV.

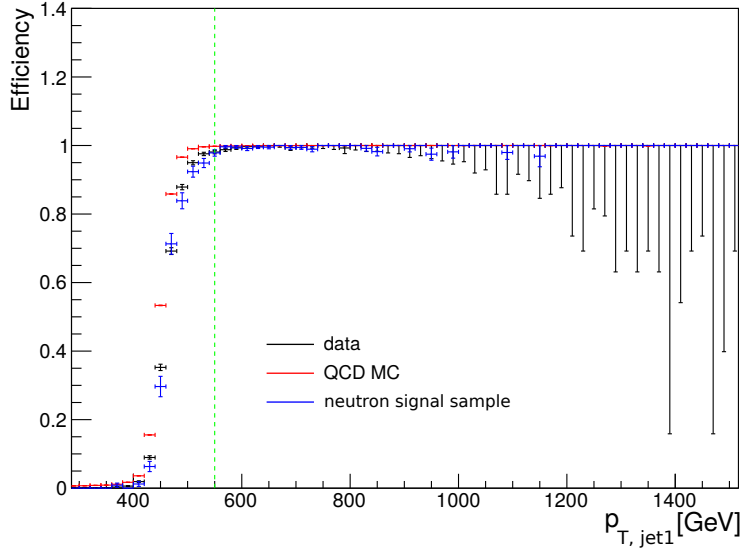


Figure 6.4: The HLT_PFJet450 trigger efficiency turn-on as a function of the offline leading jet p_T , for data, QCD events, and the signal-like events. The p_T cut used in the event selection is shown with a green dashed line.

2254 6.3 Event selection

2255 The event selection aims to select back-to-back dijet events with a low ChF. As a baseline se-
 2256 lection, the two highest- p_T jets are required to have $p_T > 550$ GeV, in order to ensure the jets
 2257 to be above the turn-on of the trigger. Furthermore, they are required to have $|\eta| < 2.0$, placing
 2258 them fully within the tracking volume, thus suppressing backgrounds from jets that have a low
 2259 ChF due to tracks falling out of tracker acceptance. As can be seen from the middle plots in
 2260 Figure 6.5, this cut has only a small impact on the signal. Since the SIMPs do not undergo
 2261 parton showering, while QCD partons undergo final state radiation, events with SIMPs have a
 2262 lower number of jets than QCD multijet events, as can be seen from the top right plot in Fig-
 2263 ure 6.6. Events containing additional jets with $p_T > 30$ GeV in the full η acceptance of the
 2264 CMS calorimeters on top of the two leading jets are therefore vetoed.

2265 A photon veto is also applied to suppress photon + jets events. This is done by rejecting
 2266 events with a photon within $\Delta R < 0.1$ of the leading or subleading jet, using the loose working
 2267 point of the cut-based photon identification to identify photons, as described in Section 4.3.3. In
 2268 some cases, however, jets have a large photon energy fraction, but the photon in the jet does not
 2269 pass the loose identification requirements, for instance when there is a photon conversion in the
 2270 tracker. In order to reject photon + jets events more efficiently, an additional cut is applied, as
 2271 described in Section 4.3.3.

2272 In order to avoid any problems related to the striking discrepancy between data and simula-
 2273 tion observed for events with only one reconstructed vertex in the top left plot of Figure 6.6, at
 2274 least two reconstructed vertices are required. Additionally, the azimuthal separation of the two
 2275 selected jets is required to be $\Delta\phi > 2$ in order to obtain back-to-back jets, which rejects the peak
 2276 visible in data at $\Delta\phi = 0$ in the bottom left plot of Figure 6.6. Finally, noise filters are applied

in order to reject beam halo or instrumental background, such as noise in the calorimeters.

Table 6.2 shows the number of events remaining in data, for simulated QCD events, and for 2 signal samples, after consecutively applying the described selection cuts. This shows that the background is already reduced by a factor 5, mainly by the cut on the number of jets, while a high efficiency is maintained for the signal. In Figure 6.5, data, QCD multijet simulation, and signal are compared after these selections, for the p_T , η and ChF of the two leading jets. Figure 6.6 shows the distribution of the number of vertices, the number of jets, $\Delta\phi(\text{jet1}, \text{jet2})$, and H_T , which is defined as the scalar sum of the transverse momenta of the two jets. In some cases, all the selection cuts except the cut on the variable being shown are applied. The bump and long tail that can be seen in the data for the $\Delta\phi(\text{jet1}, \text{jet2})$ distribution contain events coming from processes with a heavy vector boson, such as $Z + \text{jets}$ or $W + \text{jets}$, or $t\bar{t}$ events. The simulation instead shows a steeply falling spectrum since only QCD dijet events are shown. Contributions from $Z + \text{jets}$ or $W + \text{jets}$, and $t\bar{t}$ events were verified to be negligible in the signal region using simulated samples.

selection cut	yield			
	data	QCD MC	SIMP ($m_\chi = 1 \text{ GeV}$)	SIMP ($m_\chi = 1000 \text{ GeV}$)
$p_T^{j1,j2} > 550 \text{ GeV}$	2540420	3152550	604	5.6
$ \eta_{j1,j2} < 2.0$	2441240	2980320	581	5.5
# jets = 2	534053	587670	509	4.8
photon veto	531366	586674	507	4.8
# vertices ≥ 2	531244	586641	507	4.9
$\Delta\phi(j1, j2) > 2$	531207	586641	507	4.8
MET filters	528614	582184	493	4.7

Table 6.2: Number of events remaining after the listed selection cuts in data, QCD events, and 2 signal samples.

As will be detailed in Section 6.4, the background is predicted from a data control region where at least one of the leading jets has a high ChF, above 0.25. No further selection on the second reconstruction with respect to the second primary vertex is applied for the control region, since the presence of at least one jet with a large ChF avoids the problem of the wrong selection of primary vertex detailed in Section 6.1.

In the case of the signal region selection, both jets are required to have $\text{ChF} < x$, where x is the signal cut being considered. In this case, the cut is applied for both reconstructions starting from the first and second primary vertex.

6.4 Background estimation

The main background for this analysis is QCD multijets. This background is estimated from data, as the simulation does not describe the data well, especially at low ChF. The signal events can then be distinguished from this background using the jet ChF. A second background comes from photon + jets events. However, this background is efficiently removed by applying a photon veto.

6.4.1 Photon + jets

The photon + jets background was studied using a high- H_T MC sample generated at LO with MADGRAPH5_aMC@NLO, hadronized with PYTHIA 8, and simulated and reconstructed using the standard procedure described in Chapter 4. The used sample corresponds to about 27 fb^{-1} , which is larger than the data sample used for this analysis and was found to be sufficient to

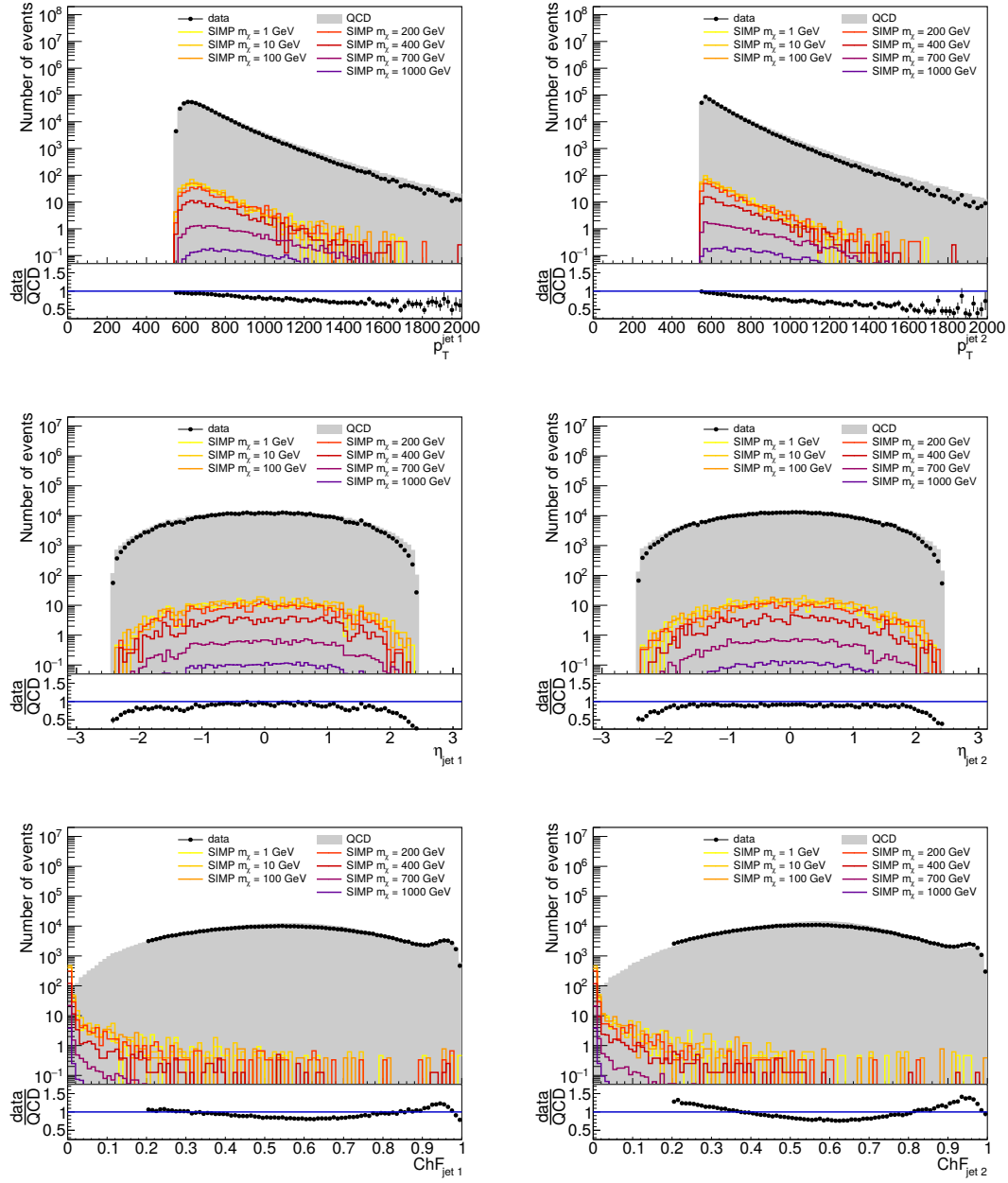


Figure 6.5: p_T , η and ChF of the leading (left) and subleading (right) jet. The selection cuts are applied, except for the cut on η in the corresponding plot.

evaluate its contribution in the signal region. This background is verified to be negligible after applying the signal region event selection, and well within any other systematic uncertainty on the background prediction. The photon veto works well, especially the cut on the jet neutral electromagnetic fraction, and no events from the used simulated photon + jets sample remain after applying a cut of $\text{ChF} < 0.1$. Additionally, in part of the events remaining just above that cut the photon is not identified because it is very close to a jet. These events are therefore already contained in the overlapping QCD multijets sample.

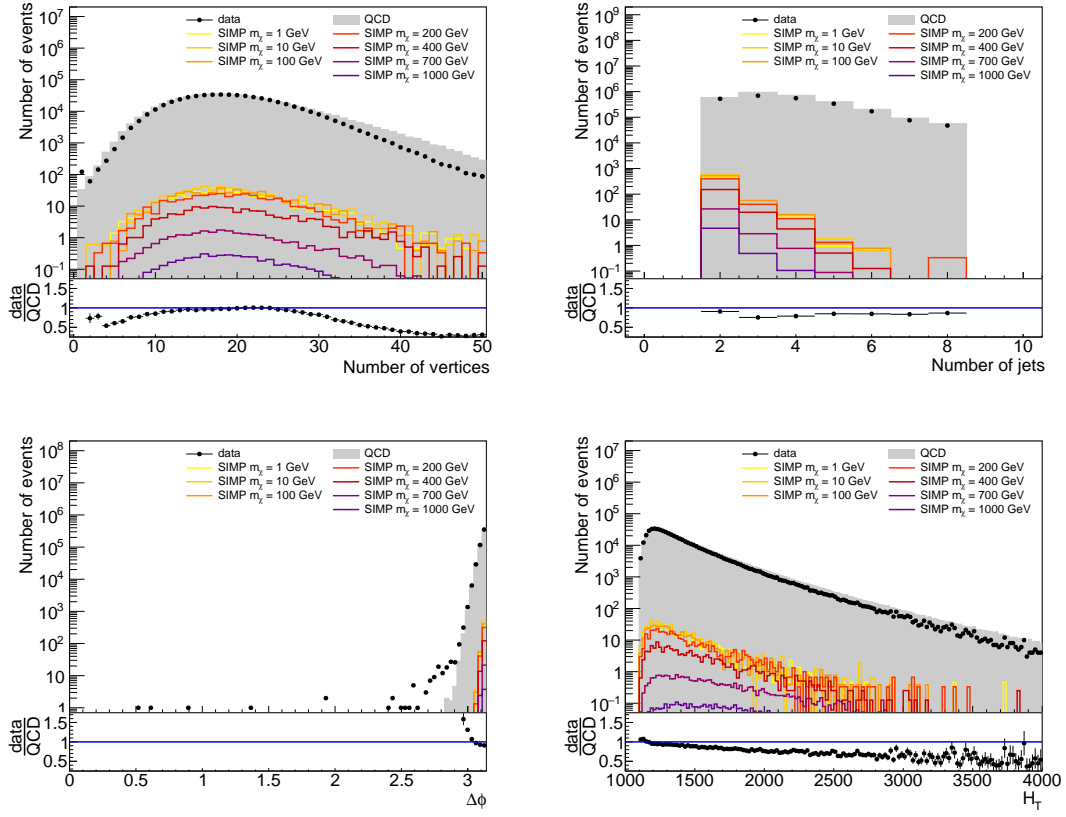


Figure 6.6: Number of vertices, number of jets in the full detector acceptance with $p_T > 30$ GeV, $\Delta\phi(\text{jet1}, \text{jet2})$, and H_T distributions, with selection cuts applied. The requirement on the number of vertices is not applied for the corresponding plot, the cut on the number of jets is not applied for the number of jets distribution, and the $\Delta\phi$ cut is similarly not applied for the corresponding distribution.

6.4.2 QCD multijets

The QCD multijet background is estimated from data, since the simulation does not describe the data well, especially at low ChF, as can be seen from Figure 6.7 which compares the ChF distribution in the control region to the QCD MC. In this plot the subleading jet is required to have a large ChF, in order to stay in the control region.

As a first step, the efficiency of the ChF cut is measured in the control region, by tagging one jet with high ChF and applying the ChF cut on the other jet. The efficiency is then given by the ratio of the number of events passing the cut divided by the total number of events selected in the control region. The measurement is performed in bins of jet p_T and η . The number of QCD events in the signal region is then predicted by using any QCD dijet event passing the selection cuts listed in Table 6.2 and applying the appropriate p_T and η dependent ChF cut efficiencies on the two leading jets. Figure 6.8 shows the measured efficiency as a function of the ChF cut for various bins in p_T^{jet} , integrating over the η_{jet} bins, and η_{jet} , integrating of the p_T^{jet} bins, as measured in the QCD MC. There is a strong dependence on the jet p_T , and a less pronounced dependence on the jet η at low ChF. The efficiencies are the highest for the $1.0 < |\eta| < 1.25$ bin, which can be attributed to this being the barrel-endcap transition region where most of the tracker material is located. As can be seen from the left plot in Figure 6.9, at generator level the ChF is independent of the jet p_T , as one would expect. However, after applying the jet reconstruction, a p_T dependence arises due to the known degradation of tracking efficiency in

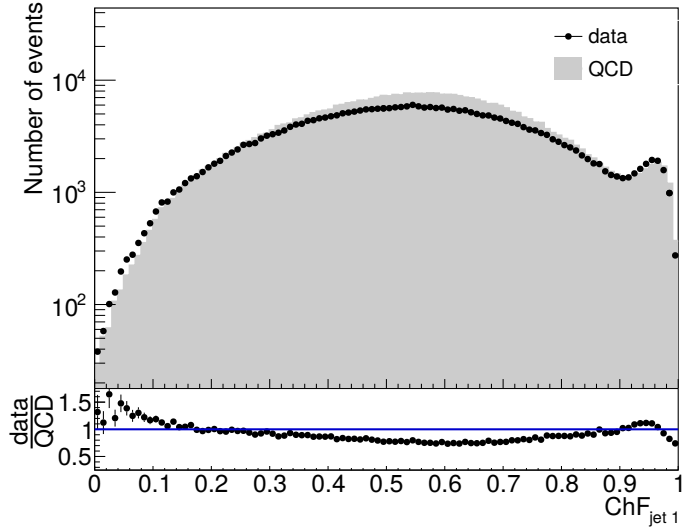


Figure 6.7: Data-MC comparison of the charged energy fraction of the leading jet, tagging events with subleading jet $\text{ChF} > 0.5$.

2336 dense jet environments, which becomes more of an issue for very high p_T and thus collimated
2337 jets, as demonstrated in the right plot of Figure 6.9.

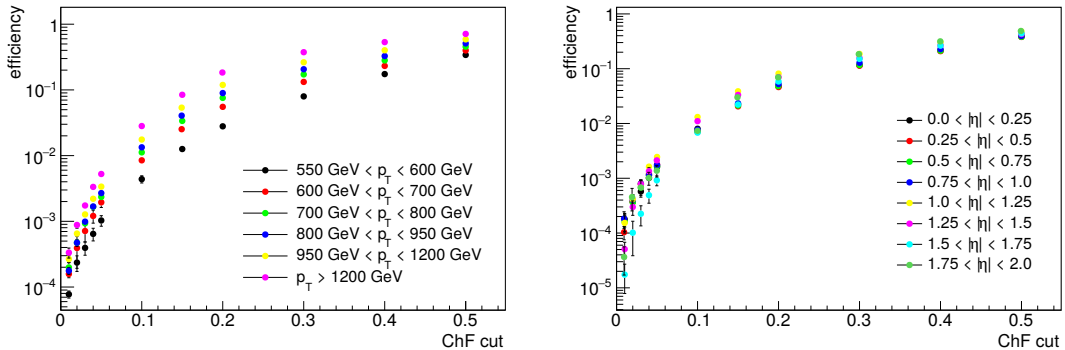


Figure 6.8: The efficiency of several ChF cuts in QCD MC, binned in p_T (left) and η (right).

2338 A test of the background prediction method is performed using simulated events in order to
2339 validate it. This is done by comparing the MC truth and the so-called 1- and 2-leg predictions.
2340 The MC truth shows the yield after applying the ChF cuts on both jets. For the 1-leg prediction
2341 the ChF cut is applied on one jet and the event is then weighted by applying the measured p_T -
2342 and η -dependent efficiency for the other jet. For the 2-leg prediction, the efficiencies are applied
2343 for both jets, and no ChF cut is applied directly.

2344 As a first check, the test was also performed at the generator level, using the GenJets, which
2345 are reconstructed from the generator level particles. This comparison is done in exclusive bins
2346 in $(\text{ChF}_{\text{jet}1}, \text{ChF}_{\text{jet}2})$, as illustrated in Figure 6.10. From Figure 6.11 one can see that there is
2347 a good agreement between MC truth, 1-, and 2-leg predictions. This shows that there are no
2348 relevant physics correlations between the 2 jets, an essential prerequisite for this background
2349 prediction to work well, and proves the p_T and η binning is adequate as well.

2350 Next, the test is performed with reconstructed jets, as shown in the left plot of Figure 6.12,
2351 using the exclusive binning. For the MC truth, the ChF cut is applied on the 2 leading jets of

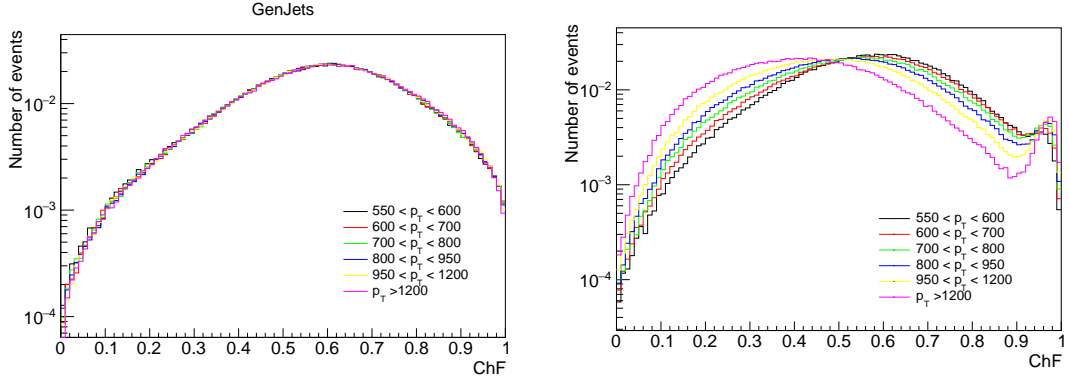


Figure 6.9: The ChF per bins of jet p_T , for generator level (left) and reconstructed (right) jets.

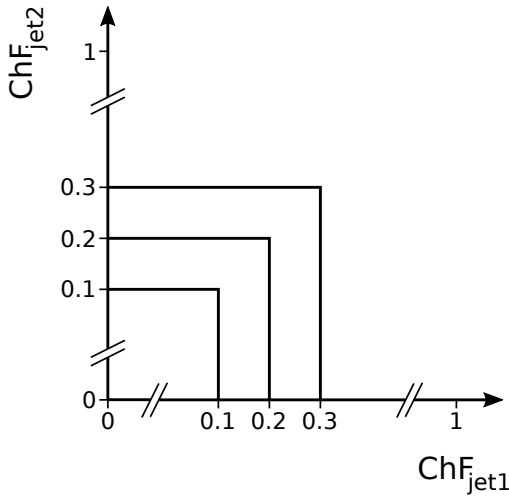


Figure 6.10: Illustration of the exclusive bins in the leading and subleading jet ChF, used for test of the background prediction method and the data vs. prediction comparisons.

the standard jet collection, as well as the 2 leading jets of the jet collection created when using the second vertex as primary vertex. This extra cut is a part of the signal region event selection described earlier, designed to remove events where the wrong primary vertex was chosen and the charged energy fraction of the jets is removed by CHS. However, there is still a small discrepancy between the MC truth and the prediction at the tightest ChF cuts. This is mainly due to a very small number of events where the wrong vertex was chosen, but where the correct one is not the second one. The level of agreement reached is however already sufficient for the considered data sample.

The test of the method is also performed in inclusive bins, as used in the signal region event selection, by applying the same cut on the ChF of both jets. This is shown in the right plot of Figure 6.12, with the applied ChF cut on the x-axis. For the MC truth, the statistical uncertainty is determined per HT-binned QCD sample, using asymmetric vertical bars with correct coverage for event counts with Poisson variates when less than 10 events remain, and the square root of the remaining number of events otherwise. In this way, the statistical uncertainty correctly reflects the contribution of HT bins with few or no events left. The total statistical uncertainty in the MC truth is then calculated by multiplying the uncertainty per HT bin by the corresponding weight for this HT bin, and adding them quadratically. The uncertainties on the 1- and 2-leg predictions are much smaller, as the statistical uncertainties from the efficiencies is negligible. The systematic uncertainty on the background prediction is then defined as the difference between the MC truth and the prediction, unless it is smaller than the statistical uncertainty on the MC

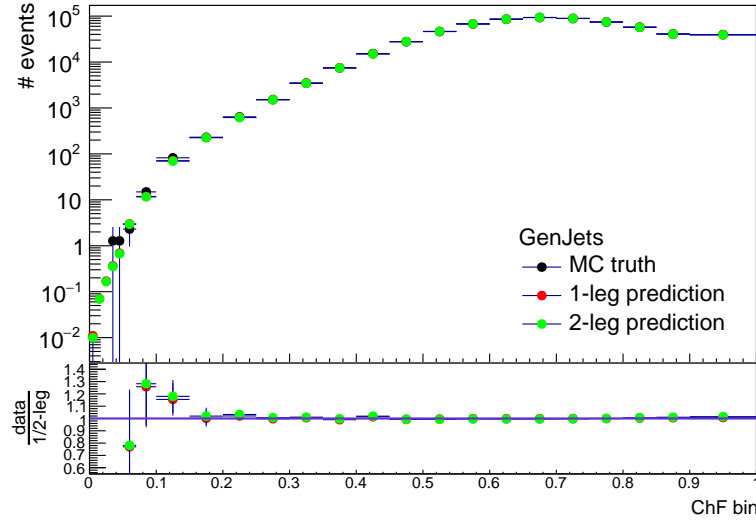


Figure 6.11: Test of the background prediction method using the GenJets in simulated events. The number of events is scaled to 16.1 fb^{-1} , corresponding to the amount of data used for this analysis.

truth. In that case, the uncertainty on the MC truth is taken as systematic uncertainty. For most ChF cut values, the statistical uncertainty dominates. As a result the background prediction is limited by the MC sample size.

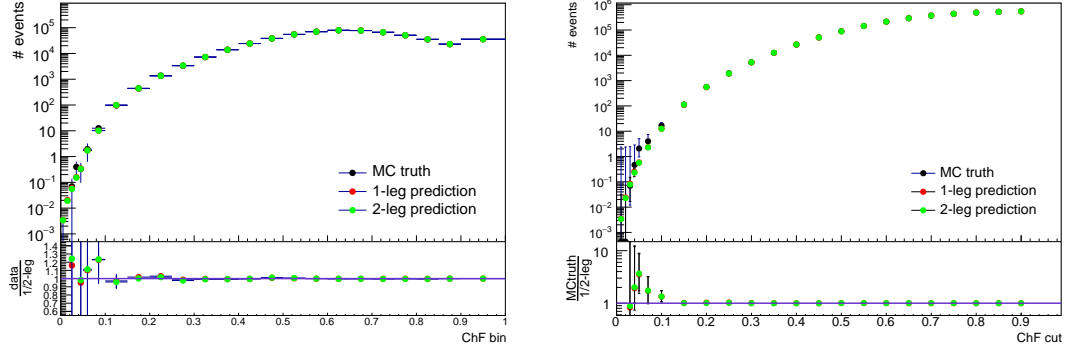


Figure 6.12: Test of the background prediction method with simulated events, using an exclusive (left) or inclusive (right) binning in ChF. The number of events is scaled to 16.1 fb^{-1} , corresponding to the amount of data used for this analysis.

The QCD background prediction in data is shown in Figure 6.13 as a function of the exclusive ChF bins, using the `HLT_PFJet450` single jet trigger. The data is blinded in the signal region below $\text{ChF} = 0.05$. A distinction is made between the run periods B to F (left) and G to H (right). There is a clear deviation below a ChF of 0.4 for run periods B to F, while the agreement is very good down to $\text{ChF} = 0.05$ for run periods G and H. The main difference between these 2 datasets is the issue with the Tracker APV pre-amplifier saturation, described in Section 3.2.6.1, which was solved from run period G onwards.

To first order, the measured ChF cut efficiencies should absorb the effects of tracking inefficiencies caused by the APV pre-amplifier saturation problem. However, this effect is also reflected in the distribution of the number of vertices. As is shown in Figure 6.14, a subtle effect causes the data and the prediction from data to disagree in the distribution of the number of ver-

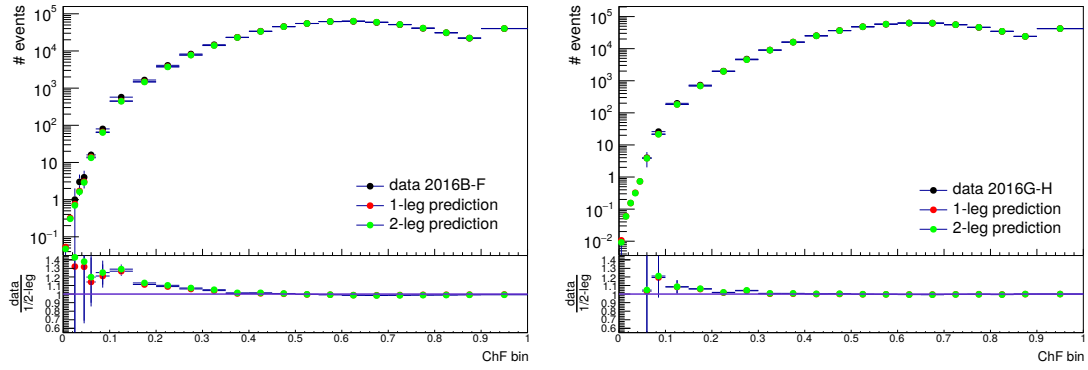


Figure 6.13: The 1- and 2-leg predictions from data, as well as the data as a function of the exclusive ChF bins, for run periods B-F (left) and G-H (right).

2386 tices for run periods B to F, while a good agreement is obtained for run periods G to H. As there
 2387 are not enough data to derive the ChF efficiencies reliably in bins of number of vertices as well
 2388 as p_T and η , a recovery of the data in this way is not possible. A reweighting was also performed,
 2389 using a fit to the ratio of data divided by the 2-leg prediction per ChF bin. Figure 6.15 shows
 2390 the data versus data prediction comparison in run period E, applying the reweighting based on
 2391 the number of vertices in the event, per ChF bin, and a clear improvement can be observed for
 2392 the 2-leg prediction. In contrast, the 1-leg prediction has not been reweighted and still shows
 2393 the original disagreement. This reweighting can however not be used in the signal region, where
 2394 very few events remain. As a result, the analysis is performed with run periods G and H only,
 2395 corresponding to an integrated luminosity of 16.1 fb^{-1} . The rejected data, from run periods B
 2396 to F, corresponds to an integrated luminosity of 17 fb^{-1} .

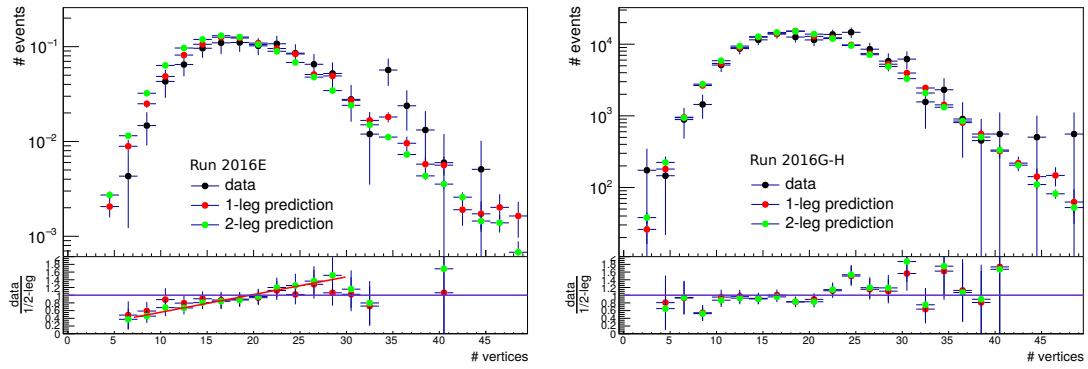


Figure 6.14: The distribution of the number of vertices for data, 1-leg, and 2-leg prediction using data from run period E (left) and run periods G-H (right).

2397 6.5 Systematic uncertainties

2398 For the signal prediction, systematic uncertainties are included for the luminosity, the jet energy
 2399 corrections, and the trigger inefficiency. The systematic uncertainty for the luminosity amounts
 2400 to 2.5% [176]. The systematic uncertainty coming from the jet energy corrections is computed
 2401 by varying the jet energy by the correction and recalculating the yield after applying the selection
 2402 cuts and the ChF cut. Depending on the SIMP mass and the ChF cut, this uncertainty varies
 2403 between 0.4% and 3.9%. A systematic uncertainty is also included to take into account the

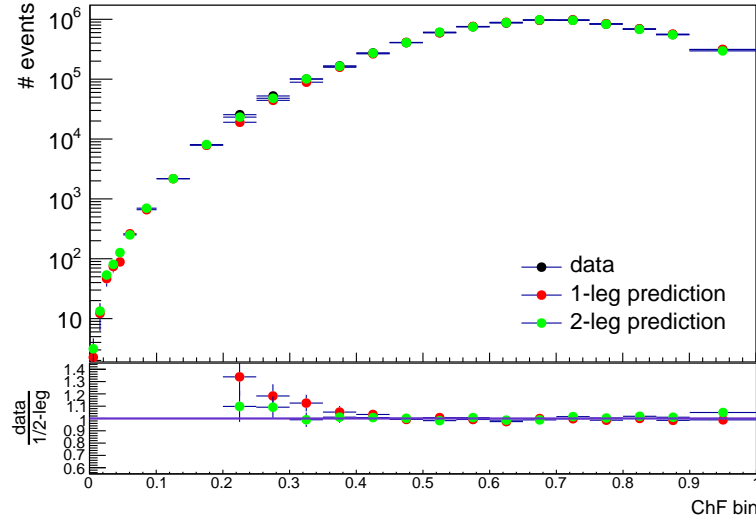


Figure 6.15: The 1- and 2-leg predictions from data, as well as the data (above ChF = 0.2) as a function of the exclusive ChF bins for run period E, reweighting the 2-leg prediction to data based on the number of vertices in the event, per ChF bin.

trigger inefficiency at 550 GeV due to the turn-on. This is done by taking 100% of the maximal inefficiency as the uncertainty, which gives a 2% systematic uncertainty for the signal. This does not take into account the fact that the turn-on was determined for one jet only and the inefficiency is strongly reduced when two jets with a similar p_T are present in the event. However, some signal events have one of the two jets with EMF = 0. In this case the jet which does not contain electromagnetic energy would not fire the single jet trigger, which requires the jet to have EMF > 0, and these events become single jet events from the trigger point of view. The 2% uncertainty is therefore conservative as it represents the worst case scenario. The photon and conversion veto was found to be 100% efficient on the signal, and as a result this systematic uncertainty is negligible. The effect of pileup was considered to be negligible as well, as the distribution of the number of vertices is very similar for the data and SIMP samples. As an example the data is compared to the SIMP sample with $m_\chi = 1000$ GeV in Figure 6.16, which shows that there is a good agreement in the bulk of the distribution with some deviations for a few events with a high number of primary vertices only.

As mentioned in Section 6.4, the main systematic uncertainty on the background prediction is obtained from the closure test in MC, by taking the difference between the MC truth and the prediction, unless it is smaller than the statistical uncertainty on the MC truth, in which case the uncertainty on the MC truth is taken as systematic uncertainty. This uncertainty varies between 4% and 3400%, depending on the ChF cut. As for the signal, the trigger inefficiency due to the turn-on at 550 GeV is also taken into account, yielding an additional 2% systematic uncertainty also for the background.

6.6 Results

Table 6.3 shows the number of predicted and observed events, per considered ChF cut. The prediction is done using the 1-leg data prediction, as this provides slightly smaller uncertainties, as every event can be used twice by applying the ChF first on one jet and then on the other. The statistical uncertainty, as well as the systematic uncertainty from the closure test described in Section 6.5, are given.

A cut of ChF < 0.05 is chosen as the final signal region selection, to reject most of the

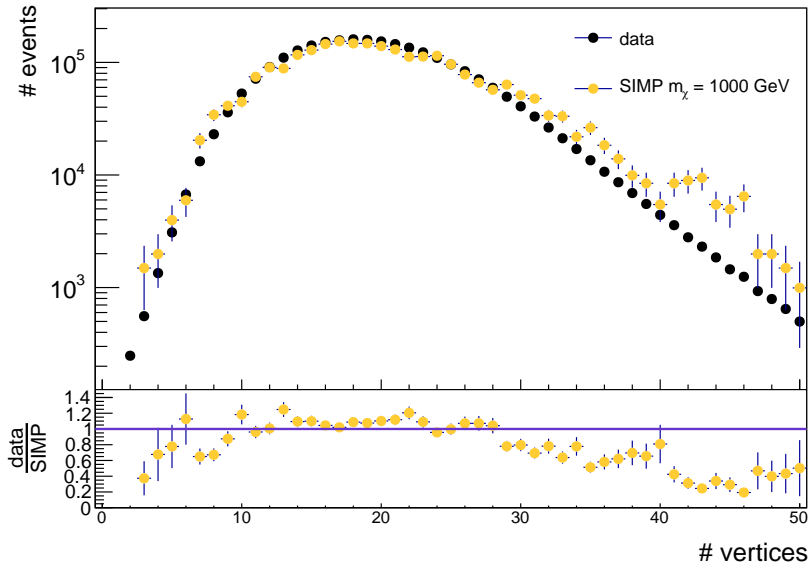


Figure 6.16: The distribution of the number of vertices in data compared to the SIMP signal with $m_\chi = 1000$ GeV.

2432 QCD background. The background is then reduced to the level of about one event, and a large
 2433 uncertainty does not have big consequences. Moreover, the uncertainty from the closure test
 2434 is reduced when taking into account the smaller statistical uncertainty on the number of back-
 2435 ground events during the limit calculation. In addition, the expected sensitivity does not improve
 2436 significantly at tighter ChF cuts, and the closure tests becomes statistically limited. The domi-
 nating uncertainty then comes from the closure test, and amounts to 250% in this case.

ChF cut	data prediction	QCD MC prediction	observed	SIMP signal [m_χ]	
				1 GeV	1000 GeV
0.2	902 ± 5 (stat.) ± 38 (syst.)	546.5 ± 0.6	969	456	4.4
0.15	210 ± 2 (stat.) ± 18 (syst.)	111.1 ± 0.4	229	442	4.3
0.1	26.9 ± 0.3 (stat.) ± 8.9 (syst.)	12.6 ± 0.2	30	426	4.2
0.07	5.1 ± 0.1 (stat.) ± 4.4 (syst.)	2.3 ± 0.2	4	408	4.0
0.05	1.28 ± 0.03 (stat.) ± 3.24 (syst.)	0.6 ± 0.1	0	395	3.9
0.04	0.55 ± 0.02 (stat.) ± 2.81 (syst.)	0.24 ± 0.09	0	387	3.8
0.03	0.22 ± 0.01 (stat.) ± 7.68 (syst.)	0.08 ± 0.07	0	377	3.7

Table 6.3: Number of predicted (using the 1-leg prediction from data) and observed events for several inclusive cuts on the ChF of both jets. The expected number of signal events is also given for the $m_\chi = 1$ GeV and $m_\chi = 1000$ GeV scenarios.

2437 Model-independent limits are derived for a $\text{ChF} < 0.05$ cut, using the CL_S criterion [155,
 2438 156] with the LHC style test statistic [162] and using the full set of pseudo-experiments, as
 2439 described in Section 5.8. This was done using the RooStat-based Combine tool, taking into
 2440 account the systematic uncertainties detailed in Section 6.5, as well as the statistical uncertainties
 2441 on signal and background predictions, and modelling them as nuisance parameters. All included
 2442 systematic uncertainties are profiled with a lognormal prior, except for the uncertainty coming
 2443 from the closure test, which is profiled with a gamma function since it arises from the limited
 2444 number of remaining events. The resulting expected fiducial cross section is $\sigma_{\text{fid}}^{95\%} = \sigma \times A \times \epsilon =$
 2445 0.17 fb . With zero observed events, the observed model-independent lower limit is found to be

$$\sigma_{\text{fid,obs}}^{95\%} = 0.18 \text{ fb.}$$

6.7 SIMP model interpretation

Limits are also derived on the production cross section for the SIMP simplified model, using the same method as described for the model-independent limits. The expected limits on the production cross section are shown for SIMP masses between 1 GeV and 1 TeV in Figure 6.17, using a cut of $\text{ChF} < 0.05$. In this case, the search is sensitive to all the generated SIMP mass points, up to 1 TeV.

Figure 6.18 shows the expected and observed limits when including the observation of zero events in the signal region. The expected and observed limits, and the theoretical cross section are given with respect to the generator level cuts applied in the signal sample generation, $p_T^\chi > 200 \text{ GeV}$ and $|\eta_\chi| < 2.5$. The shown theoretical cross section is also given per SIMP mass point in Table 4.1. In summary, no significant excess above the expected background is observed, and the considered SIMP simplified model is ruled out for SIMP masses up to 1000 GeV.

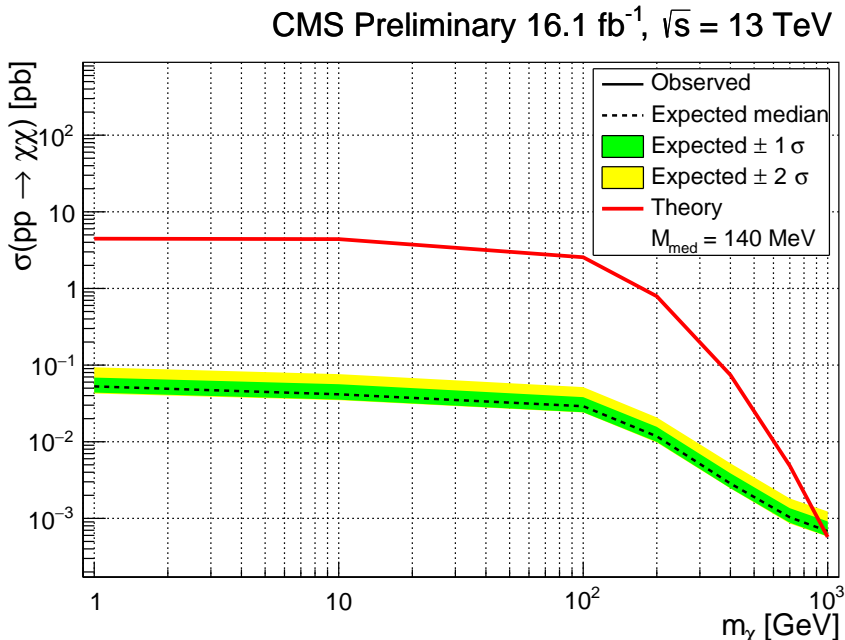


Figure 6.17: The expected limits on the production cross section, obtained without looking in the signal region, for SIMP masses between 1 and 1000 GeV, with 1σ and 2σ bands is shown, as well as the theoretical prediction (red), with respect to the generator level cuts ($p_T^\chi > 200 \text{ GeV}$ and $|\eta_\chi| < 2.5$).

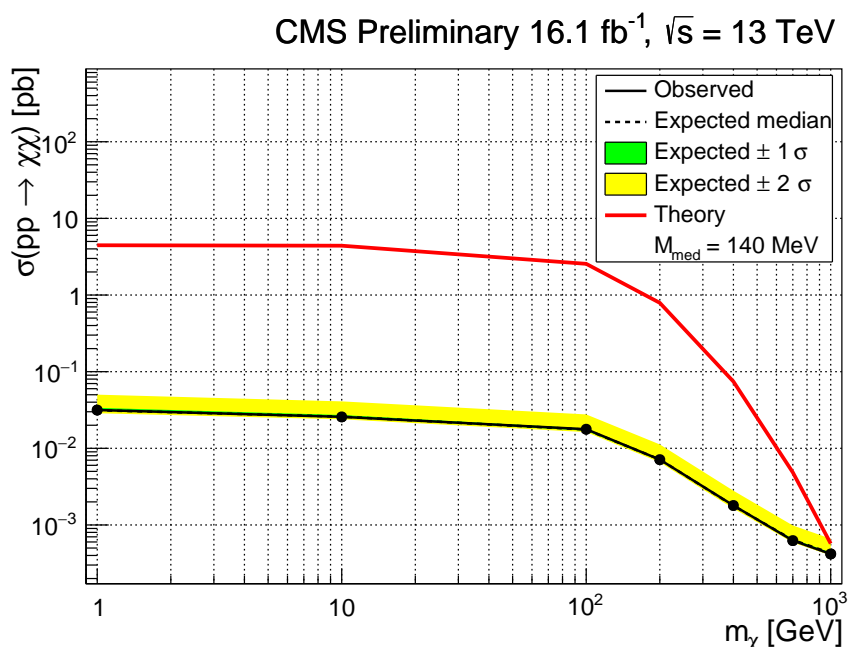


Figure 6.18: The expected and observed limits on the production cross section for SIMP masses between 1 and 1000 GeV, with 1σ and 2σ bands is shown, as well as the theoretical prediction (red), with respect to the generator level cuts ($p_T^\chi > 200$ GeV and $|\eta_\chi| < 2.5$).

7

2460

2461

Conclusions & Outlook

2462 *This is the way the world ends*
2463 *Not with a bang but a whimper.*

2464

– T.S. Eliot, *The Hollow Men*

2465 One of the remaining unsolved mysteries in the universe is the presumed existence of dark
2466 matter. Various astrophysical observations indicate the presence of an unknown type of matter
2467 next to the known visible matter. As it does not interact electromagnetically, only very little is
2468 known about this new type of matter, and many theories exist to explain its nature and origin.
2469 These theories can be tested through a variety of techniques and experiments. Depending on
2470 the exact nature of the dark matter particles, they could also be produced at colliders in high-
2471 energy collisions between Standard Model particles. Currently, the largest particle accelerator
2472 in the world is the LHC at CERN, which provides proton-proton collisions with a record centre-
2473 of-mass energy of 13 TeV at a very high rate. In this thesis, two complementary searches for
2474 dark matter have been performed with data collected by the CMS detector located at one of the
2475 interaction points of this collider.

2476 For both analyses, simplified model interpretations were considered. While dark matter
2477 does not interact electromagnetically, in these models it is assumed to interact with the ordinary
2478 matter through a new force. In the first analysis, the dark matter candidates are expected to
2479 interact very weakly with Standard Model particles and leave the detector undetected. They can
2480 however be detected when they recoil against another object in the event. In this case, the studied
2481 signature is one or more jets together with missing transverse energy. This search was already
2482 performed during Run 1, and has now been improved for Run 2. One of the main developments
2483 was the refinement of the prediction of events with a Z boson decaying to two neutrinos in
2484 association with one or more jets, which led to an improved sensitivity. While the first iteration
2485 of this analysis with Run 2 data sets less stringent limits on the scenario with a vector mediator
2486 compared to the Run 1 analysis, the new results including the discussed improvements and using
2487 data corresponding to 12.9 fb^{-1} set stronger limits up to mediator masses of 1.95 TeV. Similar
2488 results are obtained for an axial-vector mediator. Scalar and pseudoscalar mediator masses are
2489 excluded up to 100 GeV and 430 GeV, respectively.

2490 In the second analysis, a different simplified model is considered, where the dark matter
2491 particles are assumed to interact strongly with Standard Model particles, through a new, light
2492 mediator. The produced pair of stable, neutral dark matter candidates will then give a signature
2493 consisting of a pair of trackless jets. First, a feasibility study for this model and corresponding
2494 signature was performed and published. For this study, the analysis strategy was developed,

and the achievable sensitivity was investigated. This model had never been tested at colliders before, and as the feasibility study showed promising results, this signature was now studied for the first time at CMS in this analysis, using a type of jets that is typically rejected by the jet identification criteria. While this search is very sensitive to new physics and the expected background was very efficiently reduced, some complications emerged as well. As an example, care was taken to account for the possibility of a wrongly chosen primary vertex, as this problem in the reconstruction can mimic signal-like events. A different issue was related to data taking and originated from the tracker APV pre-amplifier saturation problem, which occurred during the first half of the 2016 data taking period at CMS. Due to the nature of this issue, the data affected by this problem were rejected for the analysis, and data corresponding to a total of 16.1 fb^{-1} were used. Moreover, the photon veto, which is crucial to reject background events coming from the production of a photon and a jet, was extended to take into account photon conversions as well. The outcome of this analysis yielded no observation of new physics, and all the considered dark matter masses, from 1 GeV up to 1 TeV, were excluded. Additionally, model-independent limits were derived as well, excluding production cross sections down to 0.18 fb .

Both results can be translated into limits on the dark matter-nucleon interaction cross section, in order to compare the results with other experiments. Depending on the dark matter mass, the monojet analysis can exclude cross sections between approximately 10^{-6} fb and 0.1 pb , for the scalar or vector mediator case. The limit on the high interaction cross sections arises at small mediator masses, where the used simplified model may be too simple since hadron resonances can change the picture. This region could consequently be further explored as a next step. In comparison, the trackless jets analysis excludes interaction cross sections of about $1 - 10 \text{ mb}$, thus complementing the monojet results at higher cross sections. Additionally, recent results which recast measurements from a low-threshold surface experiment looking for dark matter also exclude SIMPs up to a SIMP-nucleon interaction cross section of approximately 1 mb at SIMP masses above 100 MeV [177].

In the future, the monojet analysis will be able to cover a larger part of phase space, going to higher mediator and dark matter masses, which translates in improvements at small interaction cross sections. Projections can for example be made for the expected sensitivity at the high luminosity LHC, which is expected to deliver 3000 fb^{-1} of integrated luminosity at a centre-of-mass energy of 14 TeV. The expected reach is shown in Figure 7.1 for an axial-vector and pseudoscalar mediator. The nominal scenario assumes that the level of control of the E_T^{miss} distribution will remain the same as in the current analysis. Two more scenarios are shown, where the systematic uncertainties are reduced by a factor 2 and 4.

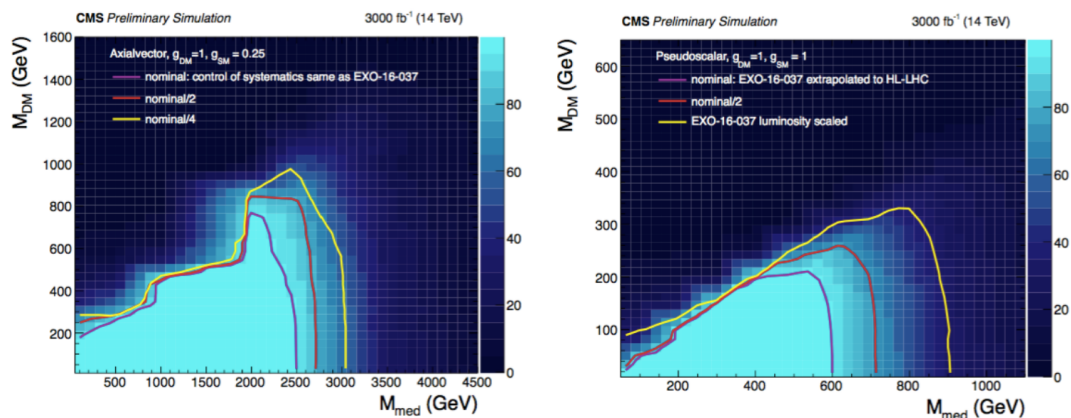


Figure 7.1: Prediction of the sensitivity of the monojet analysis in the $m_{\text{med}} - m_{\text{DM}}$ plane at the high luminosity LHC, using 3000 fb^{-1} of integrated luminosity, for an axial-vector mediator (left) and a pseudoscalar mediator (right). Figures taken from [178].

2530 For the pseudoscalar mediator, the systematic uncertainties are dominated by the uncertainty
2531 on lepton identification and isolation efficiencies used in the selection of events in the control
2532 regions at low missing transverse momentum. At high missing transverse momentum on the
2533 other hand, the systematic uncertainties are dominated by the statistical uncertainty. For the
2534 nominal scenario shown in the right plot of Figure 7.1, the systematic uncertainties are scaled by
2535 the luminosity at high E_T^{miss} and scaled according to the predictions for the uncertainty on the
2536 lepton identification and isolation efficiencies at low E_T^{miss} . Additionally, a scenario is shown
2537 where the systematic uncertainties are reduced by a factor 2, as well as a scenario where the
2538 systematic uncertainties are scaled by the luminosity over the full E_T^{miss} range.

2539 The obtained estimations show that mediator masses up to at least 2.5 TeV and 600 GeV
2540 could be excluded in the axial-vector and pseudoscalar case, respectively. This corresponds to
2541 an increase in range of about 30%.

2542 In the case of the trackless jets search, the entire considered dark matter mass range is al-
2543 ready excluded by the described results. As the interaction cross section in the model is restricted
2544 a narrow range in order to have a trackless jets signature, it was possible to exclude this model
2545 instead of excluding it up to some cross section only. In a next step, the mass range could be
2546 extended, or the search could be broadened by allowing more extra jets, or including missing
2547 transverse energy in the signature. Alternative signatures can also be obtained by assuming a dif-
2548 ferent interaction cross section, such as emerging jets or a cluster of tracks in the muon systems.
2549 Aside from SIMPs, Hidden Valley models can also give rise to this kind of signature [179]. In
2550 these models, the interaction with the hidden sector can for example happen through rare Higgs
2551 boson decays. Additionally, trackless jets could also be produced by dark photons [180]. This
2552 model is now being studied as well, and the analysis can benefit from this first trackless jets anal-
2553 ysis, among other things concerning the issue of the tracker APV pre-amplifier saturation. In the
2554 considered scenario, the neutral dark photon is produced in association with an ordinary photon.
2555 The resulting signature is then composed of a photon and a trackless jet with energy deposits in
2556 the ECAL or HCAL, or missing transverse energy, depending on the interaction strength.

References

- [1] K. G. Begeman, A. H. Broeils, and R. H. Sanders, “Extended rotation curves of spiral galaxies: Dark haloes and modified dynamics,” *Mon. Not. Roy. Astron. Soc.*, vol. 249, p. 523, 1991.
- [2] V. Belokurov, N. W. Evans, P. C. Hewett, A. Moiseev, R. G. McMahon, S. F. Sanchez, and L. J. King, “Two New Large Separation Gravitational Lenses from SDSS,” *Mon. Not. Roy. Astron. Soc.*, vol. 392, p. 104, 2009.
- [3] G. F. Smoot *et al.*, “Structure in the COBE differential microwave radiometer first year maps,” *Astrophys. J.*, vol. 396, pp. L1–L5, 1992.
- [4] E. Komatsu *et al.*, “Seven-Year Wilkinson Microwave Anisotropy Probe (WMAP) Observations: Cosmological Interpretation,” *Astrophys. J. Suppl.*, vol. 192, p. 18, 2011.
- [5] P. A. R. Ade *et al.*, “Planck 2013 results. XVI. Cosmological parameters,” *Astron. Astrophys.*, vol. 571, p. A16, 2014.
- [6] N. Daci, I. De Bruyn, S. Lowette, M. H. G. Tytgat, and B. Zaldivar, “Simplified SIMPs and the LHC,” *JHEP*, vol. 11, p. 108, 2015.
- [7] M. E. Peskin and D. V. Schroeder, *An introduction to quantum field theory; 1995 ed.* Boulder, CO: Westview, 1995. [Online]. Available: <https://cds.cern.ch/record/257493>
- [8] Y. Nagashima, *Beyond the standard model of elementary particle physics.* Weinheim, Germany: Wiley-VCH Verlag, 2014. [Online]. Available: <http://www-spires.fnal.gov/spires/find/books/www?cl=QC793.2.N34::2014>
- [9] G. Aad *et al.*, “Observation of a new particle in the search for the Standard Model Higgs boson with the ATLAS detector at the LHC,” *Phys. Lett.*, vol. B716, pp. 1–29, 2012.
- [10] S. Chatrchyan *et al.*, “Observation of a new boson at a mass of 125 GeV with the CMS experiment at the LHC,” *Phys. Lett.*, vol. B716, pp. 30–61, 2012.
- [11] S. L. Glashow, “The renormalizability of vector meson interactions,” *Nucl. Phys.*, vol. 10, pp. 107–117, 1959.
- [12] S. Weinberg, “A Model of Leptons,” *Phys. Rev. Lett.*, vol. 19, pp. 1264–1266, 1967.
- [13] A. Salam and J. C. Ward, “Weak and electromagnetic interactions,” *Nuovo Cim.*, vol. 11, pp. 568–577, 1959.
- [14] F. Englert and R. Brout, “Broken Symmetry and the Mass of Gauge Vector Mesons,” *Phys. Rev. Lett.*, vol. 13, pp. 321–323, 1964.
- [15] P. W. Higgs, “Broken Symmetries and the Masses of Gauge Bosons,” *Phys. Rev. Lett.*, vol. 13, pp. 508–509, 1964.
- [16] G. S. Guralnik, C. R. Hagen, and T. W. B. Kibble, “Global Conservation Laws and Massless Particles,” *Phys. Rev. Lett.*, vol. 13, pp. 585–587, 1964.

- 2592 [17] D. J. Gross and F. Wilczek, “Ultraviolet Behavior of Nonabelian Gauge Theories,” *Phys.*
2593 *Rev. Lett.*, vol. 30, pp. 1343–1346, 1973.
- 2594 [18] H. D. Politzer, “Reliable Perturbative Results for Strong Interactions?” *Phys. Rev. Lett.*,
2595 vol. 30, pp. 1346–1349, 1973.
- 2596 [19] <http://www.quantumdiaries.org/2014/03/14/the-standard-model-a-beautiful-but-flawed-theory>.
- 2597 [20] Q. R. Ahmad *et al.*, “Direct evidence for neutrino flavor transformation from neutral
2598 current interactions in the Sudbury Neutrino Observatory,” *Phys. Rev. Lett.*, vol. 89, p.
2599 011301, 2002.
- 2600 [21] Y. Fukuda *et al.*, “Evidence for oscillation of atmospheric neutrinos,” *Phys. Rev. Lett.*,
2601 vol. 81, pp. 1562–1567, 1998.
- 2602 [22] G. Bertone, D. Hooper, and J. Silk, “Particle dark matter: Evidence, candidates and con-
2603 straints,” *Phys. Rept.*, vol. 405, pp. 279–390, 2005.
- 2604 [23] F. Zwicky, “Die Rotverschiebung von extragalaktischen Nebeln,” *Helv. Phys. Acta*, vol. 6,
2605 pp. 110–127, 1933, [Gen. Rel. Grav.41,207(2009)].
- 2606 [24] P. Salucci and A. Borriello, “The intriguing distribution of dark matter in galaxies,” *Lect.*
2607 *Notes Phys.*, vol. 616, pp. 66–77, 2003.
- 2608 [25] A. A. Penzias and R. W. Wilson, “A Measurement of excess antenna temperature at 4080-
2609 Mc/s,” *Astrophys. J.*, vol. 142, pp. 419–421, 1965.
- 2610 [26] <https://briankoberlein.com/2015/06/15/science-in-the-raw>.
- 2611 [27] P. A. R. Ade *et al.*, “Planck 2013 results. I. Overview of products and scientific results,”
2612 *Astron. Astrophys.*, vol. 571, p. A1, 2014.
- 2613 [28] M. Azzaro, F. Prada, and C. M. Gutierrez, “Motion properties of satellites around external
2614 spiral galaxies,” *ASP Conf. Ser.*, vol. 327, p. 268, 2004.
- 2615 [29] M. Mateo, “Dwarf galaxies of the Local Group,” *Ann. Rev. Astron. Astrophys.*, vol. 36,
2616 pp. 435–506, 1998.
- 2617 [30] J. N. Bahcall, C. Flynn, and A. Gould, “Local dark matter from a carefully selected sam-
2618 ple,” *Astrophys. J.*, vol. 389, pp. 234–250, 1992.
- 2619 [31] M. Milgrom, “A Modification of the Newtonian dynamics as a possible alternative to the
2620 hidden mass hypothesis,” *Astrophys. J.*, vol. 270, pp. 365–370, 1983.
- 2621 [32] M. Milgrom, “A Modification of the Newtonian dynamics: Implications for galaxies,”
2622 *Astrophys. J.*, vol. 270, pp. 371–383, 1983.
- 2623 [33] M. Milgrom, “A modification of the Newtonian dynamics: implications for galaxy sys-
2624 tems,” *Astrophys. J.*, vol. 270, pp. 384–389, 1983.
- 2625 [34] J. D. Bekenstein, “Relativistic gravitation theory for the MOND paradigm,” *Phys. Rev.*,
2626 vol. D70, p. 083509, 2004, [Erratum: *Phys. Rev.D71,069901(2005)*].
- 2627 [35] E. P. Verlinde, “Emergent Gravity and the Dark Universe,” *SciPost Phys.*, vol. 2, no. 3, p.
2628 016, 2017.
- 2629 [36] L. Bergström, “Nonbaryonic dark matter: Observational evidence and detection meth-
2630 ods,” *Rept. Prog. Phys.*, vol. 63, p. 793, 2000.

- 2631 [37] V. M. Lobashev, “The search for the neutrino mass by direct method in the tritium beta-
2632 decay and perspectives of study it in the project KATRIN,” *Nucl. Phys.*, vol. A719, pp.
2633 153–160, 2003.
- 2634 [38] V. N. Aseev *et al.*, “An upper limit on electron antineutrino mass from Troitsk experi-
2635 ment,” *Phys. Rev.*, vol. D84, p. 112003, 2011.
- 2636 [39] C. Kraus *et al.*, “Final results from phase II of the Mainz neutrino mass search in tritium
2637 beta decay,” *Eur. Phys. J.*, vol. C40, pp. 447–468, 2005.
- 2638 [40] M. C. Gonzalez-Garcia and Y. Nir, “Neutrino masses and mixing: Evidence and implica-
2639 tions,” *Rev. Mod. Phys.*, vol. 75, pp. 345–402, 2003.
- 2640 [41] S. Dodelson and L. M. Widrow, “Sterile-neutrinos as dark matter,” *Phys. Rev. Lett.*,
2641 vol. 72, pp. 17–20, 1994.
- 2642 [42] N. Yoshida, A. Sokasian, L. Hernquist, and V. Springel, “Early structure formation and
2643 reionization in a warm dark matter cosmology,” *Astrophys. J.*, vol. 591, pp. L1–L4, 2003.
- 2644 [43] L. J. Rosenberg and K. A. van Bibber, “Searches for invisible axions,” *Phys. Rept.*, vol.
2645 325, pp. 1–39, 2000.
- 2646 [44] A. A. Klypin, A. V. Kravtsov, O. Valenzuela, and F. Prada, “Where are the missing Galac-
2647 tic satellites?” *Astrophys. J.*, vol. 522, pp. 82–92, 1999.
- 2648 [45] B. Moore, S. Ghigna, F. Governato, G. Lake, T. R. Quinn, J. Stadel, and P. Tozzi, “Dark
2649 matter substructure within galactic halos,” *Astrophys. J.*, vol. 524, pp. L19–L22, 1999.
- 2650 [46] L. Hui, J. P. Ostriker, S. Tremaine, and E. Witten, “Ultralight scalars as cosmological dark
2651 matter,” *Phys. Rev.*, vol. D95, no. 4, p. 043541, 2017.
- 2652 [47] S. Hawking, “Gravitationally collapsed objects of very low mass,” *Mon. Not. Roy. Astron.
2653 Soc.*, vol. 152, p. 75, 1971.
- 2654 [48] B. P. Abbott *et al.*, “Observation of Gravitational Waves from a Binary Black Hole
2655 Merger,” *Phys. Rev. Lett.*, vol. 116, no. 6, p. 061102, 2016.
- 2656 [49] M. Sasaki, T. Suyama, T. Tanaka, and S. Yokoyama, “Primordial Black Hole Scenario for
2657 the Gravitational-Wave Event GW150914,” *Phys. Rev. Lett.*, vol. 117, no. 6, p. 061101,
2658 2016.
- 2659 [50] S. Clesse and J. Garcia-Bellido, “The clustering of massive Primordial Black Holes as
2660 Dark Matter: measuring their mass distribution with Advanced LIGO,” *Phys. Dark Univ.*,
2661 vol. 15, pp. 142–147, 2017.
- 2662 [51] S. Bird, I. Cholis, J. B. Munoz, Y. Ali-Haïmoud, M. Kamionkowski, E. D. Kovetz, A. Rac-
2663 canelli, and A. G. Riess, “Did LIGO detect dark matter?” *Phys. Rev. Lett.*, vol. 116, no. 20,
2664 p. 201301, 2016.
- 2665 [52] D. Hooper, “Particle Dark Matter,” in *Proceedings of Theoretical Advanced Study
2666 Institute in Elementary Particle Physics on The dawn of the LHC era (TASI
2667 2008): Boulder, USA, June 2-27, 2008*, 2010, pp. 709–764. [Online]. Available:
2668 http://lss.fnal.gov/cgi-bin/find_paper.pl?conf-09-025
- 2669 [53] K. Kainulainen and K. A. Olive, “Astrophysical and cosmological constraints on neutrino
2670 masses,” *Springer Tracts Mod. Phys.*, vol. 190, pp. 53–74, 2003.
- 2671 [54] N. Arkani-Hamed, S. Dimopoulos, and G. R. Dvali, “The Hierarchy problem and new
2672 dimensions at a millimeter,” *Phys. Lett.*, vol. B429, pp. 263–272, 1998.

- 2673 [55] L. Randall and R. Sundrum, “A Large mass hierarchy from a small extra dimension,”
2674 *Phys. Rev. Lett.*, vol. 83, pp. 3370–3373, 1999.
- 2675 [56] E. W. Kolb, D. J. H. Chung, and A. Riotto, “WIMPzillas!” in *Trends in*
2676 *theoretical physics II. Proceedings, 2nd La Plata Meeting, Buenos Aires, Argentina,*
2677 *November 29-December 4, 1998*, 1998, pp. 91–105, [,91(1998)]. [Online]. Available:
2678 http://lss.fnal.gov/cgi-bin/find_paper.pl?conf=98-325
- 2679 [57] D. N. Spergel and P. J. Steinhardt, “Observational evidence for selfinteracting cold dark
2680 matter,” *Phys. Rev. Lett.*, vol. 84, pp. 3760–3763, 2000.
- 2681 [58] A. De Rujula, S. L. Glashow, and U. Sarid, “CHARGED DARK MATTER,” *Nucl. Phys.*,
2682 vol. B333, pp. 173–194, 1990.
- 2683 [59] A. Kusenko and M. E. Shaposhnikov, “Supersymmetric Q balls as dark matter,” *Phys.*
2684 *Lett.*, vol. B418, pp. 46–54, 1998.
- 2685 [60] J. R. Ellis, “Particle candidates for dark matter,” *Phys. Scripta*, vol. T85, pp. 221–230,
2686 2000.
- 2687 [61] L. Bergstrom, “Dark Matter Candidates,” *New J. Phys.*, vol. 11, p. 105006, 2009.
- 2688 [62] R. Bernabei *et al.*, “Final model independent result of DAMA/LIBRA-phase1,” *Eur. Phys.*
2689 *J.*, vol. C73, p. 2648, 2013.
- 2690 [63] R. Agnese *et al.*, “Search for Low-Mass Weakly Interacting Massive Particles with Su-
2691 perCDMS,” *Phys. Rev. Lett.*, vol. 112, no. 24, p. 241302, 2014.
- 2692 [64] E. Armengaud *et al.*, “Constraints on low-mass WIMPs from the EDELWEISS-III dark
2693 matter search,” *JCAP*, vol. 1605, no. 05, p. 019, 2016.
- 2694 [65] G. Angloher *et al.*, “Results on low mass WIMPs using an upgraded CRESST-II detector,”
2695 *Eur. Phys. J.*, vol. C74, no. 12, p. 3184, 2014.
- 2696 [66] E. Aprile *et al.*, “XENON100 Dark Matter Results from a Combination of 477 Live
2697 Days,” *Phys. Rev.*, vol. D94, no. 12, p. 122001, 2016.
- 2698 [67] D. S. Akerib *et al.*, “Results from a search for dark matter in the complete LUX exposure,”
2699 *Phys. Rev. Lett.*, vol. 118, no. 2, p. 021303, 2017.
- 2700 [68] C. Amole *et al.*, “Dark Matter Search Results from the PICO-60 C₃F₈ Bubble Chamber,”
2701 *Phys. Rev. Lett.*, vol. 118, no. 25, p. 251301, 2017.
- 2702 [69] C. Fu *et al.*, “Spin-Dependent Weakly-Interacting-Massive-ParticleNucleon Cross Sec-
2703 tion Limits from First Data of PandaX-II Experiment,” *Phys. Rev. Lett.*, vol. 118, no. 7, p.
2704 071301, 2017.
- 2705 [70] T. Marrodn Undagoitia and L. Rauch, “Dark matter direct-detection experiments,” *J.*
2706 *Phys.*, vol. G43, no. 1, p. 013001, 2016.
- 2707 [71] W. B. Atwood *et al.*, “The Large Area Telescope on the Fermi Gamma-ray Space Tele-
2708 scope Mission,” *Astrophys. J.*, vol. 697, pp. 1071–1102, 2009.
- 2709 [72] F. Aharonian *et al.*, “Observations of the Crab Nebula with H.E.S.S.,” *Astron. Astrophys.*,
2710 vol. 457, pp. 899–915, 2006.
- 2711 [73] J. Aleksic *et al.*, “Performance of the MAGIC stereo system obtained with Crab Nebula
2712 data,” *Astropart. Phys.*, vol. 35, pp. 435–448, 2012.

- 2713 [74] J. Holder *et al.*, “Status of the VERITAS Observatory,” *AIP Conf. Proc.*, vol. 1085, pp.
2714 657–660, 2009.
- 2715 [75] M. Ageron *et al.*, “ANTARES: the first undersea neutrino telescope,” *Nucl. Instrum.*
2716 *Meth.*, vol. A656, pp. 11–38, 2011.
- 2717 [76] A. Achterberg *et al.*, “First Year Performance of The IceCube Neutrino Telescope,” *Ast-*
2718 *ropart. Phys.*, vol. 26, pp. 155–173, 2006.
- 2719 [77] A. Kounine, “The Alpha Magnetic Spectrometer on the International Space Station,” *Int.*
2720 *J. Mod. Phys.*, vol. E21, no. 08, p. 1230005, 2012.
- 2721 [78] P. Picozza *et al.*, “PAMELA: A Payload for Antimatter Matter Exploration and Light-
2722 nuclei Astrophysics,” *Astropart. Phys.*, vol. 27, pp. 296–315, 2007.
- 2723 [79] A. M. Sirunyan *et al.*, “Search for dark matter produced with an energetic jet or a hadron-
2724 ically decaying W or Z boson at $\sqrt{s} = 13$ TeV,” *JHEP*, vol. 07, p. 014, 2017.
- 2725 [80] M. Aaboud *et al.*, “Search for dark matter produced in association with a hadronically
2726 decaying vector boson in pp collisions at $\sqrt{s} = 13$ TeV with the ATLAS detector,” *Phys.*
2727 *Lett.*, vol. B763, pp. 251–268, 2016.
- 2728 [81] F. Kahlhoefer, “Review of LHC Dark Matter Searches,” *Int. J. Mod. Phys.*, vol. A32,
2729 no. 13, p. 1730006, 2017.
- 2730 [82] O. Buchmueller, C. Doglioni, and L. T. Wang, “Search for dark matter at colliders,” *Nature*
2731 *Phys.*, vol. 13, no. 3, pp. 217–223, 2017.
- 2732 [83] ATLAS collaboration, “Search for long-lived, massive particles in events with displaced
2733 vertices and missing transverse momentum in 13 TeV pp collisions with the ATLAS de-
2734 tector,” 2017.
- 2735 [84] ATLAS collaboration, “Search for long-lived charginos based on a disappearing-track
2736 signature in pp collisions at $\sqrt{s} = 13$ TeV with the ATLAS detector,” 2017.
- 2737 [85] ATLAS collaboration, “Search for Higgs boson decays to Beyond-the-Standard-Model
2738 light bosons in four-lepton events with the ATLAS detector at $\sqrt{s} = 13$ TeV,” 2017.
- 2739 [86] A. M. Sirunyan *et al.*, “Search for new physics with dijet angular distributions in proton-
2740 proton collisions at $\sqrt{s} = 13$ TeV,” *JHEP*, vol. 07, p. 013, 2017.
- 2741 [87] A. M. Sirunyan *et al.*, “Search for dijet resonances in protonproton collisions at $\sqrt{s} =$
2742 13 TeV and constraints on dark matter and other models,” *Phys. Lett.*, vol. B769, pp.
2743 520–542, 2017, [Erratum: *Phys. Lett.*B772,882(2017)].
- 2744 [88] M. Aaboud *et al.*, “Search for new phenomena in dijet events using 37 fb^{-1} of pp collision
2745 data collected at $\sqrt{s} = 13$ TeV with the ATLAS detector,” *Phys. Rev.*, vol. D96, p. 052004,
2746 2017.
- 2747 [89] Y. Bai and A. Rajaraman, “Dark Matter Jets at the LHC,” 2011.
- 2748 [90] CMS Collaboration, “Search for heavy stable charged particles with 12.9 fb^{-1} of 2016
2749 data,” 2016.
- 2750 [91] M. Aaboud *et al.*, “Search for metastable heavy charged particles with large ionization
2751 energy loss in pp collisions at $\sqrt{s} = 13$ TeV using the ATLAS experiment,” *Phys. Rev.*,
2752 vol. D93, no. 11, p. 112015, 2016.
- 2753 [92] <http://cms-results.web.cern.ch/cms-results/public-results/publications/EXO/index.html>.

- 2754 [93] G. Busoni, A. De Simone, E. Morgante, and A. Riotto, “On the Validity of the Effective
2755 Field Theory for Dark Matter Searches at the LHC,” *Phys. Lett.*, vol. B728, pp. 412–421,
2756 2014.
- 2757 [94] G. Busoni, A. De Simone, J. Gramling, E. Morgante, and A. Riotto, “On the Validity
2758 of the Effective Field Theory for Dark Matter Searches at the LHC, Part II: Complete
2759 Analysis for the s -channel,” *JCAP*, vol. 1406, p. 060, 2014.
- 2760 [95] G. Busoni, A. De Simone, T. Jacques, E. Morgante, and A. Riotto, “On the Validity of
2761 the Effective Field Theory for Dark Matter Searches at the LHC Part III: Analysis for the
2762 t -channel,” *JCAP*, vol. 1409, p. 022, 2014.
- 2763 [96] D. Abercrombie *et al.*, “Dark Matter Benchmark Models for Early LHC Run-2 Searches:
2764 Report of the ATLAS/CMS Dark Matter Forum,” 2015.
- 2765 [97] G. Busoni *et al.*, “Recommendations on presenting LHC searches for missing transverse
2766 energy signals using simplified s -channel models of dark matter,” 2016.
- 2767 [98] J. S. Bullock, “Notes on the Missing Satellites Problem,” 2010.
- 2768 [99] M. Boylan-Kolchin, J. S. Bullock, and M. Kaplinghat, “Too big to fail? The puzzling
2769 darkness of massive Milky Way subhaloes,” *Mon. Not. Roy. Astron. Soc.*, vol. 415, p.
2770 L40, 2011.
- 2771 [100] D. H. Weinberg, J. S. Bullock, F. Governato, R. Kuzio de Naray, and A. H. G. Peter,
2772 “Cold dark matter: controversies on small scales,” *Proc. Nat. Acad. Sci.*, vol. 112, pp.
2773 12 249–12 255, 2014, [Proc. Nat. Acad. Sci.112,2249(2015)].
- 2774 [101] B. Famaey and S. McGaugh, “Challenges for Lambda-CDM and MOND,” *J. Phys. Conf.
2775 Ser.*, vol. 437, p. 012001, 2013.
- 2776 [102] J. F. Donoghue, E. Golowich, and B. R. Holstein, “Dynamics of the standard model,”
2777 *Camb. Monogr. Part. Phys. Nucl. Phys. Cosmol.*, vol. 2, pp. 1–540, 1992, [Camb. Monogr.
2778 Part. Phys. Nucl. Phys. Cosmol.35(2014)].
- 2779 [103] C. Downum, T. Barnes, J. R. Stone, and E. S. Swanson, “Nucleon-meson coupling
2780 constants and form-factors in the quark model,” *Phys. Lett.*, vol. B638, pp. 455–460, 2006.
- 2781 [104] S. W. Randall, M. Markevitch, D. Clowe, A. H. Gonzalez, and M. Bradac, “Constraints
2782 on the Self-Interaction Cross-Section of Dark Matter from Numerical Simulations of the
2783 Merging Galaxy Cluster 1E 0657-56,” *Astrophys. J.*, vol. 679, pp. 1173–1180, 2008.
- 2784 [105] J. L. Feng, “Dark Matter Candidates from Particle Physics and Methods of Detection,”
2785 *Ann. Rev. Astron. Astrophys.*, vol. 48, pp. 495–545, 2010.
- 2786 [106] G. D. Mack, J. F. Beacom, and G. Bertone, “Towards Closing the Window on Strongly
2787 Interacting Dark Matter: Far-Reaching Constraints from Earth’s Heat Flow,” *Phys. Rev.*,
2788 vol. D76, p. 043523, 2007.
- 2789 [107] J. Rich, R. Rocchia, and M. Spiro, “A Search for Strongly Interacting Dark Matter,” *Phys.
2790 Lett.*, vol. B194, p. 173, 1987, [,221(1987)].
- 2791 [108] A. L. Erickcek, P. J. Steinhardt, D. McCammon, and P. C. McGuire, “Constraints on
2792 the Interactions between Dark Matter and Baryons from the X-ray Quantum Calorimetry
2793 Experiment,” *Phys. Rev.*, vol. D76, p. 042007, 2007.
- 2794 [109] G. D. Mack and A. Manohar, “Closing the window on high-mass strongly interacting dark
2795 matter,” *J. Phys.*, vol. G40, p. 115202, 2013.

- 2796 [110] R. H. Cyburt, B. D. Fields, V. Pavlidou, and B. D. Wandelt, “Constraining strong baryon
2797 dark matter interactions with primordial nucleosynthesis and cosmic rays,” *Phys. Rev.*,
2798 vol. D65, p. 123503, 2002.
- 2799 [111] X.-l. Chen, S. Hannestad, and R. J. Scherrer, “Cosmic microwave background and large
2800 scale structure limits on the interaction between dark matter and baryons,” *Phys. Rev.*, vol.
2801 D65, p. 123515, 2002.
- 2802 [112] C. Dvorkin, K. Blum, and M. Kamionkowski, “Constraining Dark Matter-Baryon Scat-
2803 tering with Linear Cosmology,” *Phys. Rev.*, vol. D89, no. 2, p. 023519, 2014.
- 2804 [113] H. R. Gustafson, C. A. Ayre, L. W. Jones, M. J. Longo, and P. V. Ramana Murthy, “Search
2805 for New Massive Long-lived Neutral Particles,” *Phys. Rev. Lett.*, vol. 37, p. 474, 1976.
- 2806 [114] K. A. Olive *et al.*, “Review of Particle Physics,” *Chin. Phys.*, vol. C38, p. 090001, 2014.
- 2807 [115] E. A. Mobs, “The CERN accelerator complex. Complexe des accrateurs du CERN,” Oct
2808 2016, general Photo. [Online]. Available: <http://cds.cern.ch/record/2225847>
- 2809 [116] S. Chatrchyan *et al.*, “The CMS Experiment at the CERN LHC,” *JINST*, vol. 3, p. S08004,
2810 2008.
- 2811 [117] D. A. Matzner Dominguez, D. Abbaneo, K. Arndt, N. Bacchetta, A. Ball, E. Bartz,
2812 W. Bertl, G. M. Bilei, G. Bolla, H. W. K. Cheung *et al.*, “CMS Technical Design Re-
2813 port for the Pixel Detector Upgrade,” 2012.
- 2814 [118] G. L. Bayatian *et al.*, “CMS Physics,” 2006.
- 2815 [119] S. Chatrchyan *et al.*, “Energy Calibration and Resolution of the CMS Electromag-
2816 netic Calorimeter in pp Collisions at $\sqrt{s} = 7$ TeV,” *JINST*, vol. 8, p. P09009, 2013,
2817 [JINST8,9009(2013)].
- 2818 [120] G. Abbiendi, “The CMS muon system in Run2: preparation, status and first results,” *PoS*,
2819 vol. EPS-HEP2015, p. 237, 2015.
- 2820 [121] A. Tapper and D. Acosta, “CMS Technical Design Report for the Level-1 Trigger Up-
2821 grade,” 2013.
- 2822 [122] J.-M. O. Andre *et al.*, “Performance of the CMS Event Builder,” no. CMS-CR-2017-034,
2823 Feb 2017. [Online]. Available: <http://cds.cern.ch/record/2252634>
- 2824 [123] <https://twiki.cern.ch/twiki/bin/view/CMSPublic/DataQuality>.
- 2825 [124] <https://twiki.cern.ch/twiki/bin/view/CMSPublic/ActiveChannelsSummary>.
- 2826 [125] E. Butz, private communication. Shown at 127th LHCC Open Session,
2827 https://indico.cern.ch/event/563488/contributions/2277293/attachments/1340356/2018262/CMS_LHCC_2016_09_21.pdf.
- 2829 [126] S. Höche, “Introduction to parton-shower event generators,” in *Proceedings, Theoretical
2830 Advanced Study Institute in Elementary Particle Physics: Journeys Through the Precision
2831 Frontier: Amplitudes for Colliders (TASI 2014): Boulder, Colorado, June 2-27, 2014,*
2832 2015, pp. 235–295. [Online]. Available: <http://inspirehep.net/record/1328513/files/arXiv:1411.4085.pdf>
- 2834 [127] J. Pumplin, D. R. Stump, J. Huston, H. L. Lai, P. M. Nadolsky, and W. K. Tung, “New
2835 generation of parton distributions with uncertainties from global QCD analysis,” *JHEP*,
2836 vol. 07, p. 012, 2002.

- 2837 [128] A. D. Martin, W. J. Stirling, R. S. Thorne, and G. Watt, “Parton distributions for the
2838 LHC,” *Eur. Phys. J.*, vol. C63, pp. 189–285, 2009.
- 2839 [129] R. D. Ball *et al.*, “Parton distributions for the LHC Run II,” *JHEP*, vol. 04, p. 040, 2015.
- 2840 [130] J. Alwall, R. Frederix, S. Frixione, V. Hirschi, F. Maltoni, O. Mattelaer, H. S. Shao,
2841 T. Stelzer, P. Torrielli, and M. Zaro, “The automated computation of tree-level and next-
2842 to-leading order differential cross sections, and their matching to parton shower simula-
2843 tions,” *JHEP*, vol. 07, p. 079, 2014.
- 2844 [131] S. Frixione, P. Nason, and C. Oleari, “Matching NLO QCD computations with Parton
2845 Shower simulations: the POWHEG method,” *JHEP*, vol. 11, p. 070, 2007.
- 2846 [132] V. N. Gribov and L. N. Lipatov, “Deep inelastic e p scattering in perturbation theory,”
2847 *Sov. J. Nucl. Phys.*, vol. 15, pp. 438–450, 1972, [Yad. Fiz.15,781(1972)].
- 2848 [133] Y. L. Dokshitzer, “Calculation of the Structure Functions for Deep Inelastic Scattering
2849 and e+ e- Annihilation by Perturbation Theory in Quantum Chromodynamics.” *Sov. Phys.
2850 JETP*, vol. 46, pp. 641–653, 1977, [Zh. Eksp. Teor. Fiz.73,1216(1977)].
- 2851 [134] G. Altarelli and G. Parisi, “Asymptotic Freedom in Parton Language,” *Nucl. Phys.*, vol.
2852 B126, pp. 298–318, 1977.
- 2853 [135] T. Sjöstrand, S. Mrenna, and P. Skands, “PYTHIA 6.4 physics and manual,” *JHEP*,
2854 vol. 05, p. 026, 2006.
- 2855 [136] B. Andersson, G. Gustafson, G. Ingelman, and T. Sjostrand, “Parton Fragmentation and
2856 String Dynamics,” *Phys. Rept.*, vol. 97, pp. 31–145, 1983.
- 2857 [137] J. M. Campbell and R. K. Ellis, “MCFM for the Tevatron and the LHC,” *Nucl. Phys. Proc.
2858 Suppl.*, vol. 205-206, pp. 10–15, 2010.
- 2859 [138] A. Alloul, N. D. Christensen, C. Degrande, C. Duhr, and B. Fuks, “FeynRules 2.0 - A
2860 complete toolbox for tree-level phenomenology,” *Comput.Phys.Commun.*, vol. 185, pp.
2861 2250–2300, 2014.
- 2862 [139] J. Allison *et al.*, “Geant4 developments and applications,” *IEEE Trans. Nucl. Sci.*, vol. 53,
2863 p. 270, 2006.
- 2864 [140] S. Chatrchyan *et al.*, “Description and performance of track and primary-vertex recon-
2865 struction with the CMS tracker,” *JINST*, vol. 9, no. 10, p. P10009, 2014.
- 2866 [141] D. Contardo, M. Klute, J. Mans, L. Silvestris, and J. Butler, “Technical Proposal for the
2867 Phase-II Upgrade of the CMS Detector,” 2015.
- 2868 [142] R. Frühwirth, W. Waltenberger, and P. Vanlaer, “Adaptive vertex fitting,” *J. Phys.*, vol.
2869 G34, p. N343, 2007.
- 2870 [143] A. Strandlie and R. Frühwirth, “Discrimination between different types of material in
2871 track reconstruction with a Gaussian-sum filter,” *IEEE Trans. Nucl. Sci.*, vol. 53, pp.
2872 3842–3849, 2006.
- 2873 [144] A. M. Sirunyan *et al.*, “Particle-flow reconstruction and global event description with the
2874 cms detector,” *JINST*, vol. 12, p. P10003, 2017.
- 2875 [145] M. Cacciari, G. P. Salam, and G. Soyez, “The anti- k t jet clustering algorithm,”
2876 *Journal of High Energy Physics*, vol. 2008, no. 04, p. 063, 2008. [Online]. Available:
2877 <http://stacks.iop.org/1126-6708/2008/i=04/a=063>

- 2878 [146] S. Chatrchyan *et al.*, “Identification of b-quark jets with the CMS experiment,” *JINST*,
2879 vol. 8, p. P04013, 2013.
- 2880 [147] V. Khachatryan *et al.*, “Reconstruction and identification of lepton decays to hadrons and
2881 at CMS,” *JINST*, vol. 11, no. 01, p. P01019, 2016.
- 2882 [148] B. Zaldivar, private communication.
- 2883 [149] V. Khachatryan *et al.*, “Search for dark matter, extra dimensions, and unparticles in mono-
2884 jet events in protonproton collisions at $\sqrt{s} = 8$ TeV,” *Eur. Phys. J.*, vol. C75, no. 5, p.
2885 235, 2015.
- 2886 [150] J. H. Kuhn, A. Kulesza, S. Pozzorini, and M. Schulze, “Electroweak corrections to
2887 hadronic photon production at large transverse momenta,” *JHEP*, vol. 03, p. 059, 2006.
- 2888 [151] S. Kallweit, J. M. Lindert, S. Pozzorini, M. Schönherr, and P. Maierhöfer,
2889 “NLO QCD+EW automation and precise predictions for V+multijet production,”
2890 in *Proceedings, 50th Rencontres de Moriond, QCD and high energy interactions: La Thuile, Italy, March 21-28, 2015*, 2015, pp. 121–124. [Online]. Available:
2891 <https://inspirehep.net/record/1372103/files/arXiv:1505.05704.pdf>
- 2892 [152] S. Kallweit, J. M. Lindert, P. Maierhöfer, S. Pozzorini, and M. Schönherr, “NLO elec-
2893 troweak automation and precise predictions for W+multijet production at the LHC,”
2894 *JHEP*, vol. 04, p. 012, 2015.
- 2895 [153] S. Kallweit, J. M. Lindert, P. Maierhofer, S. Pozzorini, and M. Schönherr, “NLO
2896 QCD+EW predictions for V + jets including off-shell vector-boson decays and multijet
2897 merging,” *JHEP*, vol. 04, p. 021, 2016.
- 2898 [154] CMS Collaboration, “CMS Luminosity Measurement for the 2015 Data Taking Period,”
2899 2016.
- 2900 [155] A. L. Read, “Presentation of search results: the cls technique,” *J. Phys.*, vol. G28, p. 2693,
2901 2002.
- 2902 [156] T. Junk, “Confidence level computation for combining searches with small statistics,”
2903 *Nucl. Instrum. Meth.*, vol. A434, p. 435, 1999.
- 2904 [157] L. Moneta, K. Belasco, K. S. Cranmer, S. Kreiss, A. Lazzaro, D. Piparo, G. Schott,
2905 W. Verkerke, and M. Wolf, “The RooStats Project,” *PoS*, vol. ACAT2010, p. 057, 2010.
- 2906 [158] Higgs working group, “Documentation of the roostats-based statistics
2907 tools for the higgs pag,” [https://twiki.cern.ch/twiki/bin/viewauth/CMS/
2908 SWGuideHiggsAnalysisCombinedLimit](https://twiki.cern.ch/twiki/bin/viewauth/CMS/SWGuideHiggsAnalysisCombinedLimit).
- 2909 [159] CMS Collaboration, “Search for dark matter with jets and missing transverse energy at
2910 13 TeV,” 2015.
- 2911 [160] CMS Collaboration, “Search for dark matter production in association with jets, or
2912 hadronically decaying W or Z boson at $\sqrt{s} = 13$ TeV,” 2016.
- 2913 [161] G. Cowan, K. Cranmer, E. Gross, and O. Vitells, “Asymptotic formulae for likelihood-
2914 based tests of new physics,” *Eur. Phys. J.*, vol. C71, p. 1554, 2011, [Erratum: *Eur. Phys.
2915 J.*C73,2501(2013)].
- 2916 [162] ATLAS, CMS, LHC Higgs Combination Group Collaborations, “Procedure for the LHC
2917 Higgs boson search combination in summer 2011,” 2011.
- 2918

- 2919 [163] O. Buchmueller, M. J. Dolan, S. A. Malik, and C. McCabe, “Characterising dark matter
2920 searches at colliders and direct detection experiments: Vector mediators,” *JHEP*, vol. 01,
2921 p. 037, 2015.
- 2922 [164] A. Kurylov and M. Kamionkowski, “Generalized analysis of weakly interacting massive
2923 particle searches,” *Phys. Rev.*, vol. D69, p. 063503, 2004.
- 2924 [165] J. Hisano, K. Ishiwata, and N. Nagata, “Gluon contribution to the dark matter direct
2925 detection,” *Phys. Rev.*, vol. D82, p. 115007, 2010.
- 2926 [166] R. Agnese *et al.*, “New Results from the Search for Low-Mass Weakly Interacting Mas-
2927 sive Particles with the CDMS Low Ionization Threshold Experiment,” *Phys. Rev. Lett.*,
2928 vol. 116, no. 7, p. 071301, 2016.
- 2929 [167] D. S. Akerib *et al.*, “Improved Limits on Scattering of Weakly Interacting Massive Par-
2930 ticles from Reanalysis of 2013 LUX Data,” *Phys. Rev. Lett.*, vol. 116, no. 16, p. 161301,
2931 2016.
- 2932 [168] G. Angloher *et al.*, “Results on light dark matter particles with a low-threshold CRESST-
2933 II detector,” *Eur. Phys. J.*, vol. C76, no. 1, p. 25, 2016.
- 2934 [169] A. Tan *et al.*, “Dark Matter Results from First 98.7 Days of Data from the PandaX-II
2935 Experiment,” *Phys. Rev. Lett.*, vol. 117, no. 12, p. 121303, 2016.
- 2936 [170] C. Amole *et al.*, “Improved dark matter search results from PICO-2L Run 2,” *Phys. Rev.*,
2937 vol. D93, no. 6, p. 061101, 2016.
- 2938 [171] C. Amole *et al.*, “Dark matter search results from the PICO-60 CF₃I bubble chamber,”
2939 *Phys. Rev.*, vol. D93, no. 5, p. 052014, 2016.
- 2940 [172] M. G. Aartsen *et al.*, “Improved limits on dark matter annihilation in the Sun with the 79-
2941 string IceCube detector and implications for supersymmetry,” *JCAP*, vol. 1604, no. 04, p.
2942 022, 2016.
- 2943 [173] K. Choi *et al.*, “Search for neutrinos from annihilation of captured low-mass dark matter
2944 particles in the Sun by Super-Kamiokande,” *Phys. Rev. Lett.*, vol. 114, no. 14, p. 141301,
2945 2015.
- 2946 [174] M. Ackermann *et al.*, “Constraining Dark Matter Models from a Combined Analysis of
2947 Milky Way Satellites with the Fermi Large Area Telescope,” *Phys. Rev. Lett.*, vol. 107, p.
2948 241302, 2011.
- 2949 [175] A. A. Abdo *et al.*, “Observations of Milky Way Dwarf Spheroidal galaxies with the Fermi-
2950 LAT detector and constraints on Dark Matter models,” *Astrophys. J.*, vol. 712, pp. 147–
2951 158, 2010.
- 2952 [176] A. Kornmayer, “The CMS Pixel Luminosity Telescope,” no. CMS-CR-2015-121, Jun
2953 2015. [Online]. Available: <https://cds.cern.ch/record/2039978>
- 2954 [177] J. H. Davis, “Probing sub-GeV mass SIMP dark matter with a low-threshold surface
2955 experiment,” 2017.
- 2956 [178] “Updates on Projections of Physics Reach with the Upgraded CMS Detector for High
2957 Luminosity LHC,” Oct 2016. [Online]. Available: <http://cds.cern.ch/record/2221747>
- 2958 [179] M. J. Strassler and K. M. Zurek, “Echoes of a hidden valley at hadron colliders,” *Phys.*
2959 *Lett.*, vol. B651, pp. 374–379, 2007.
- 2960 [180] E. Izaguirre and I. Yavin, “New window to millicharged particles at the LHC,” *Phys. Rev.*,
2961 vol. D92, no. 3, p. 035014, 2015.

List of Acronyms

2963

A

2964 ALICE
2966 ATLAS

A Large Ion Collider Experiment
A Toroidal LHC ApparatuS

2967

B

2969 BU

Builder Unit

2970

C

2972 CERN
2973 CHS
2974 CMB
2975 CMS
2976 CSC

European Organization for Nuclear Research
charged hadron subtraction
Cosmic Microwave Background
Compact Muon Solenoid
Cathode Strip Chamber

2977

D

2979 DAQ
2980 DQM
2981 DT

data acquisition
Data Quality Monitoring
Drift Tube

2982

E

2984 ECAL

electromagnetic calorimeter

2985

F

2987 FED
2988 FSR
2989 FU

Front End Driver
final state radiation
Filter Unit

2990

G

2992 GSF

Gaussian-sum filter

2993

H

2995 HCAL
2996 HLT
2997 HSCP

hadronic calorimeter
High-Level Trigger
heavy stable charged particle

2998

I

3000 IP

interaction point

3001 ISR

initial state radiation

3002

J

3004 JER

jet energy resolution

3005

L

3007 L1

Level-1

3008 LEIR

Low Energy Ion Ring

3009 LEP

Large Electron Positron

3010 LHC

Large Hadron Collider

3011 LHCb

LHC Beauty

3012 LO

leading order

3013

N

3015 NLO

next-to-leading order

3016

P

3018 PDF

parton distribution function

3019 PF

particle flow

3020 PS

Proton Synchrotron

3021 PSB

Proton Synchrotron Booster

3022

Q

3024 QCD

Quantum Chromodynamics

3025

R

3027 RF

radio-frequency

3028 ROC

read-out chip

3029 RPC

Resistive Plate Chamber

3030 RU

Readout Unit

3031

S

3033 SIDM

self-interacting dark matter

3034 SIMP

strongly interacting massive particle

3035 SPS

Super Proton Synchrotron

3036 SUSY

supersymmetry

3037

T

3039 TEC

Tracker EndCaps

3040	TIB	Tracker Inner Barrel
3041	TID	Tracker Inner Disks
3042	TOB	Tracker Outer Barrel
3043		
3044	W	
3045	WIMP	weakly interacting massive particle

3046